

Characterizing and modelling the perpendicular to the grain mode-I fracture process of (tropical) hardwood

Rolf Rademaker



CHARACTERIZING AND MODELLING THE MODE-I FRACTURE PROCESS OF (TROPICAL) HARDWOOD

MASTER THESIS

A thesis report submitted for partial fulfillment of the requirements for the degree of

Master of Science in Civil Engineering

by

ROLF RADEMAKER

Thesis committee:

Dr. ir. G.J.P. Ravenshorst (<i>chair</i>)	Engineering Structures, Biobased Structures and Materials
Prof. dr. ir. J.W.G. van de Kuilen	Engineering Structures, Biobased Structures and Materials
Dr. R. Esposito	Applied Mechanics, Structural Mechanics
Dr. Y. Mosleh	Engineering Structures, Biobased Structures and Materials
Dr. M. Mirra	Engineering Structures, Biobased Structures and Materials

Faculty of Civil Engineering and Geosciences
Delft University of Technology

December 2022



PREFACE

This report presents the results of a study on the characterization and modelling of the mode-I fracture process of (tropical) hardwood. This thesis is the finalizing part in my master study Civil Engineering, with a specialisation in Structural Mechanics, at the Delft University of Technology.

"Offset your carbon footprint by donating..." is an option you recently have when buying a plane ticket or a new sweater. Why is there no option for offsetting the carbon footprint when living in a new building made of concrete and steel? Fortunately there is a transition going on in the construction industry from building with conventional highly polluting building materials to building with more sustainable materials, such as wood. But this transition is moving so slow to meet the climate goals we want to achieve. My goal with this thesis and the coming years as an engineer is to contribute to this transition and to reach for a construction industry which is built around timber. This is the bigger picture, but with this research I hope to have reduced the knowledge gap on building with timber ever so slightly.

Reaching the goals of this research is of course impossible without the help of the people who know more about the material than I do. Therefore I would sincerely like to thank the bio-based section and the major part of my thesis committee: Geert Ravenshorst, Michele Mirra, Jan-Willem van de Kuilen and Yasmine Mosleh. Coming from a master track focused mainly on theoretics, your knowledge and input on the material itself was very helpful in understanding the behaviour we have seen during testing. Furthermore, I would like to thank Rita Esposito for her contribution in the computational mechanics parts of the thesis. I would also like to thank Drs. Wolfgang F. Gard for his insights and assistance during the study of the microscopic structure of wood. A final special appreciation to Giorgos Stamoulis and Ruben Kunz for their guidance in preparation and execution of the experiments.

After reading this thesis I hope to have expanded your knowledge and interest in the material wood and why we should not only appreciate the material for its aesthetics but also for its structural capabilities.

Rolf Rademaker
29 November 2022, Rotterdam

SUMMARY

The demand to build with wood and other bio-based materials has increased rapidly the last decade, due to the ambition to build more with sustainable building materials. One of the major challenges in building with wood, is to account for the lower strength and stiffness perpendicular to the grain. Wood is an anisotropic material, meaning the material has different properties in different directions. Loading in the perpendicular to the grain direction is sometimes unavoidable and fracture often occurs in a brittle manner. Unfortunately, our understanding and knowledge of the perpendicular to the grain fracture is limited. This is especially the case for hardwoods, for which the material properties and the parameters important for the fracture process are often unknown.

The goal of this thesis is to reduce this knowledge gap on the material properties and the relevant parameters in mode-I (pure tension) fracture process of (tropical) hardwood. The knowledge gained in this research provides the answer to the main research question of this thesis:

Which parameters should be considered when describing the constitutive model of a (tropical) hardwood in mode-I tension?

This research question is answered by conducting a single-end notched three-point bending test on four different wood species: spruce (softwood), oak, bilinga and azobé. In addition to the bending test, a numerical and analytical analysis is performed to describe the constitutive law of these wood species and evaluate which parameters are important. For the azobé wood specie additional testing is done with varying growth ring orientation and size of the specimen. The experimental approach is split in two analysis, a qualitative and a quantitative analysis. In the qualitative analysis the fracture process is investigated based on visual observations and features of the general mechanical behaviour. This includes a study on the anatomical features (for example: the composition of ray cells and vessels), the fracture surface, the load-displacement curve and the stress distribution throughout the beam. In the quantitative study the fracture process is described by numerical values. Wood is often seen as a quasi-brittle material, meaning a softening regime provides stiffness when the tensile strength has been reached. For a quasi-brittle material, the constitutive law is described by four main parameters: the modulus of elasticity (MoE) E_{90} and the tensile strength perpendicular to the grain $f_{t,90}$, the mode-I fracture energy $G_{f,I}$ and the shape of the tension softening curve. In the quantitative study the fracture process is described by these four material properties.

The single-end notch three-point bending (SEN-TPB) test demonstrated a strong influence of the orientation of the growth rings on the perpendicular to the grain fracture process of azobé. The value for the peak load and post-peak behaviour change significantly depending on the orientation in which the sample is placed. Furthermore, visual observations and results from a profilometer revealed that there is an inconsistency in the roughness of the cracked surface area between the different series. From the microscopic analysis is concluded that this inconsistency in general mechanical behaviour and the roughness of the cracked surface area is linked to the composition of ray and parenchyma cells. Moreover, the direction of the ray and parenchyma cells with respect to the fracture plane is different depending on the orientation of the sample. When the ray cells are orientated perpendicular to the crack plane, a higher strength is obtained. The thin-walled parenchyma cells significantly reduce the post-elastic stiffness if these cells are orientated perpendicular to the crack plane. The influence of the composition and orientation of both cells is reflected in the numerical value for the modulus of elasticity, the tensile strength and the fracture energy.

In the numerical model cracking is modelled with discrete interface elements. In the material model the resistance to cracking is described by two main parameters: the fracture energy and the shape of the tension softening curve. Calibration of the numerical model showed that wood fracture can accurately be modelled with a bi-linear tension softening curve for the series which showed a more gradual development of the crack. On the opposite, the series which show a more brittle and unstable fracture process are modelled with a linear tension softening curve. Furthermore, an adjusted value for the fracture energy which takes into account the surface area of the fracture plane. The calibration is based on a comparison with the load-displacement curve and the crack tip opening displacement (CTOD) curve from the experiment. The influence of the growth ring orientation is taken into account in the material model in the input value for the fracture energy.

In addition to a numerical model, an analytical model is presented based on linear-elastic beam theory and the energy balance of the system. For a notched specimen the exact location of the neutral axis is difficult to define. Based on the horizontal strain distribution obtained in the experiments and the stress distribution in the numerical model, an estimation can be given on the location of the neutral axis and the stress distribution around the notch. With the location of the neutral axis and linear-elastic beam theory, the load-displacement curve can be computed. The critical cracking load of the system is computed with the change in the potential energy of the system and the found values for the fracture energy. Both the estimated critical cracking load and load-displacement curve from the analytical model provided accurate results with the experiments and the numerical model.

To conclude, this research showed that the composition of the cells in a wood specie and the orientation in which the growth rings are placed significantly influence the mode-I fracture process of a hardwood. This influence is reflected in the modulus of elasticity, the tensile strength, the fracture energy and the shape of the tension softening curve perpendicular to the grain. The results of this research provide new insight into the fracture modelling of hardwood. Both in numerical modelling and design considerations the variation in the material properties because of the orientation of the growth rings, should not be neglected.

NOMENCLATURE

$\bar{\sigma}$	Linear-elastic stress tensor (N/mm ²)
$\bar{\varepsilon}$	Linear-elastic strain tensor (-)
\bar{D}	Linear-elastic stiffness tensor (N/mm ²)
$\Delta\delta_k$	Integration step size vertical displacement (mm)
γ	Geometric parameter in the analytical model (mm)
κ	Damage threshold parameter (-)
μ	Poisson's ratio (-)
Π	Total energy (Nmm)
ρ	Density (kg/m ³)
$\tilde{\varepsilon}$	Equivalent strain (-)
ε	Strain (-)
a	Parameter defining the dimensions of the tested specimen (mm)
a_0	Initial notch length (mm)
A_c	Cracked surface area (mm ²)
a_c	Crack length (mm)
A_{approx}	Two-dimensional approximated cracked surface area (mm ²)
A_{real}	Real cracked surface area (mm ²)
B	Brittleness number (-)
b	Beam width (mm)
d_i	Damage variable in the continuum damage mechanics model (-)
E_L	Modulus of elasticity in the longitudinal direction (N/mm ²)

E_R	Modulus of elasticity in the radial direction (N/mm ²)
E_T	Modulus of elasticity in the tangential direction (N/mm ²)
E_{90}	Modulus of elasticity perpendicular to the grain (N/mm ²)
F_c	Critical external load (N)
$f_{c,90}$	Compression strength perpendicular to the grain (N/mm ²)
$f_{t,90}$	Tensile strength perpendicular to the grain (N/mm ²)
G	Energy release rate (N/mm)
g_f	Mesh-independent value for the fracture energy (N/mm)
$G_{f,90}$	Fracture energy perpendicular to the grain (N/mm)
$G_{f,\mu}$	Fracture energy associated with micro-cracking (N/mm)
$G_{f,b}$	Fracture energy associated with fiber-bridging (N/mm)
$G_{f,I}$	Mode-I fracture energy (N/mm)
$G_{f,I}^{\text{num}}$	Adjusted value for the mode-I fracture energy (N/mm)
h	Beam height (mm)
K	Stress intensity factor (MPa m ^{1/2})
k_h	Depth factor (-)
l	Beam span (mm)
l_{ch}	Characteristic length (mm)
u	Vertical displacement (mm)
U_c	Energy associated with crack propagation (Nmm)
u_f	Vertical displacement upon failure (mm)
U_p	Potential energy (Nmm)
U_s	Strain energy (Nmm)
w	Crack opening displacement (mm)
w_0	Crack opening displacement at the onset of tension softening (mm)
w_c	Critical crack opening displacement (mm)
W_{ext}	Work applied by the external load (Nmm)

CONTENTS

Preface	I
Summary	II
Nomenclature	IV
1 Introduction	1
1.1 Background	1
1.2 Problem statement and scientific relevance	2
1.3 Scope	3
1.4 Research questions	4
1.5 Research approach	6
1.5.1 Qualitative analysis	7
1.5.2 Quantitative analysis	7
1.5.3 Numerical model calibration	7
1.5.4 Theoretical approach	8
1.6 Thesis outline	8
2 Literature study	10
2.1 Material wood	10
2.1.1 Anatomy	10
2.1.2 Wood characteristics	13
2.1.3 Constitutive model	19
2.2 Fracture mechanics	22
2.2.1 Linear elastic fracture mechanics	23
2.2.2 Non-linear fracture mechanics	23
2.3 Numerical models	27
3 Materials and methodology	30
3.1 Introduction	30
3.2 Scope and limitations of the experiments	30
3.3 Materials	31
3.4 Research methods	33
3.4.1 Unnotched three-point bending test (UN-TPB)	33

3.4.2	Single edge notch three-point bending test (SEN-TPB)	33
3.4.3	Area measurement	37
3.4.4	Microscopic analysis	38
3.4.5	Density measurement	39
3.4.6	Back-analysis	40
4	Experimental observations	43
4.1	General mechanical behaviour	43
4.2	Crack plane observations	46
4.3	Microscopic analysis	46
4.4	Discussion	51
4.4.1	Key findings	52
4.4.2	Interpretation of the results	53
5	Estimation of the mechanical properties	56
5.1	Density	56
5.2	Fracture energy	57
5.3	Modulus of elasticity	58
5.4	Tensile strength	59
5.5	Correlation material properties	60
5.6	Characteristic length	61
5.7	Evaluation of the material properties	63
5.7.1	Key findings	63
5.7.2	Interpretation of the results	63
5.8	Limitations of the experiment	68
5.9	Conclusions	69
6	Numerical modelling	71
6.1	Introduction	71
6.1.1	Scope and limitations	71
6.1.2	Methodology	72
6.2	Numerical model	73
6.2.1	Finite element model	73
6.2.2	Numerical results	79
6.3	Numerical model calibration	81
6.3.1	Key findings	81
6.3.2	Discussion numerical results	83
6.3.3	Model calibration	84
6.4	Influence of the material properties on the numerical results	93
6.5	Conclusion	96
7	Practical implications	97
7.1	Theoretical energy release analysis	97
7.1.1	Linear-elastic analytical model	97
7.1.2	Energy-based failure criterion	100

7.2	Recommendations for design	102
8	Conclusion	104
8.1	Answer to the secondary research questions	104
8.2	Answer to the main research question	105
9	Recommendations	107
	References	110
	Bibliography	112
A	Reliability study DIC	113
B	Density of the samples	115
C	Load levels load-displacement curve numerical model	116
D	Mesh sensitivity and convergence	117
E	Calculations theoretical energy release analysis	121

LIST OF FIGURES

1.1	Wake Tech Community College timber bridge collapse. From (Van Voorhis, 2016).	1
1.2	Notched beams and beams with holes where the structural members are loaded perpendicular to the grain. From (Blaß & Sandhaas, 2017).	2
1.3	Flow chart research approach.	6
2.1	Section planes and wood axes: longitudinal (L), radial (R) and tangential (T). Adapted from (Dourado et al., 2015).	11
2.2	Schematic illustration of the microscopic structure of (a) softwood and (b) hardwood. Adapted from (Blaß & Sandhaas, 2017).	12
2.3	Microscopic structure of (a) oak and (b) bilinga.	12
2.4	Influence of the orientation of the growth rings on the modulus of elasticity for softwoods. From (Danielsson, 2013).	16
2.5	Typical perpendicular to the grain stress-strain curve for clear wood. Adapted from (Fransen, 2016; Blaß & Sandhaas, 2017).	17
2.6	(a) Schematic illustration and (b) scanning-electron micrograph of crossover fibre bridging in a carbon-fibre reinforced composite. From (Gamstedt, Bader, & De Borst, 2012).	18
2.7	The tensile strength perpendicular to the grain for beech and ash. From (Kovryga, Stapel, & van de Kuilen, 2020)	19
2.8	The constitutive model for a quasi-brittle material.	20
2.9	The exponential and bi-linear tension softening models for a numerical model. Adapted from (Stanzl-Tschegg, Tan, & Tschegg, 1995).	21
2.10	Fracture modes. From (Blaß & Sandhaas, 2017).	22
2.11	Crack propagation systems. From (Danielsson, 2013)	23
2.12	The three phases which can be distinguished when a material point is loaded until fracture	24
2.13	Schematic representation of the horizontal stress distribution over the height at mid-span during loading.	25
3.1	Geometry of the test specimen.	32
3.2	(a) Photo and (b) schematic representation of the test setup.	34
3.3	The Keyence VR-6000 optical profilometer.	38

3.4	(a) The HistoCore Multicut R microtome to prepare the samples and (b) the Keyence VHX 6000 microscope to produce the microscopic images.	39
3.5	Flow chart of the back-analysis to determine the values for the modulus of elasticity.	41
3.6	Flow chart of the back-analysis to determine the values for the tensile strength.	42
4.1	Load-displacement curve of the experimental results.	45
4.2	Contour plot of the highest principal strains for a spruce sample, showing how the stress distribution changes around the notch.	45
4.3	Horizontal stress distribution over the height of the beam for spruce (sample: 24_NSP_2). The parameter x is the distance along the length/axis of the beam.	46
4.4	3D image of the fracture surface captured with the profilometer.	47
4.5	Top view of the out-of-plane crack propagation path.	49
4.6	Cell structure spruce.	50
4.7	Cell structure oak.	51
4.8	Cell structure bilinga.	51
4.9	Cell structure azobé.	51
4.10	Images of the fiber-bridging process in a AZ_0_80 sample (sample: 16_NAZ_10) obtained with the DIC cameras.	52
4.11	Failure modes and cell orientation of the different azobé orientations.	54
5.1	Correlation between the density and the fracture energy, with values from literature and this research.	62
5.2	Load-displacement curves of a wedge splitting test with the growth rings under an angle of (a) 0 degrees (TL-orientation) and (b) 90 degrees (RL-orientation). From (Reiterer, Sinn, & Stanzl-Tschegg, 2002).	66
6.1	The finite element model of the SEN-TPB test for (a) the series with a height of 80 mm and (b) with a height of 120 mm.	74
6.2	The finite element mesh of (a) the series with a height of 80 mm and (b) with a height of 120 mm.	76
6.3	Detailed image of the area around the notch and interface elements. The image shows the location of the interface elements and the direction of the local axes.	77
6.4	Load-displacement curve of the numerical models of each series.	80
6.5	The crack tip opening displacement (CTOD) at the notch end during the loading process.	83
6.6	Constitutive law with the material properties of the AZ_0_80 series with a linear and a bi-linear tension softening curve.	84
6.7	Load-displacement curve for the experimental results and the numerical models, with the linear tension softening curve and the bi-linear tension softening curve.	85

6.8	Line diagram of the horizontal traction (STNy) along the interface elements for multiple points throughout the loading process for the AZ_0_80 series with a linear tension softening curve.	86
6.9	Line diagram of the horizontal traction (STNy) along the interface elements for multiple points throughout the loading process for the AZ_0_80 series with a bi-linear tension softening curve.	87
6.10	Load-displacement curve for the experimental results and the numerical models, with the linear tensions softening curve, the bi-linear tension softening curve and the model with the adjusted fracture energy.	89
6.11	Load-displacement curve for the AZ_0_80 series with a discrete crack model and a smeared crack model.	90
6.12	Contour plot of the highest principal strain (E1) for multiple points throughout the loading process for the AZ_0_80 series with a bi-linear tension softening curve and a smeared crack model.	92
6.13	Constitutive law of the material model with the tensile strength found in the back-analysis and the adjusted fracture energy considering the cracked surface area.	94
6.14	Load-displacement curve of the AZ_0_80 series showing the influence of the material properties on the general mechanical behaviour.	95
7.1	Effective height distribution over the length of the beam.	98
7.2	Load-displacement curve of the experimental results, the numerical model and the analytical model.	101
7.3	Example of a linear orthotropic softwood material model in Autodesk Revit 2023.	103
A.1	Test setup of the reliability study of the DIC showing (a) the location of the horizontal LVDT and (b) the location of the strain gauge.	113
A.2	Horizontal strain results during testing from the DIC, strain gauge and LVDT.	114
D.1	Load-displacement curve for (a) the AZ_45_80 series and (b) the AZ_0_80 series, for a mesh size of 0.5, 1.0, 2.0 and 5.0 mm.	117
D.2	The number of iterations in each load step for the AZ_45_80 series, with mesh size: 0.5, 1.0, 2.0 and 5.0 mm.	118
D.3	The number of iterations in each load step for the AZ_0_80 series, with mesh size: 0.5, 1.0, 2.0 and 5.0 mm.	119
D.4	The computation time for (a) the AZ_45_80 series and (b) the AZ_0_80 series.	120
D.5	Load-displacement curve for (a) the AZ_45_80 series and (b) the AZ_0_80 series with different load step sizes.	120
E.1	Linear-elastic symmetry model to obtain the load-displacement relation.	121

LIST OF TABLES

2.1	Microscopic structure of wood species (Wagenführ & Scheiber, 2006). . . .	13
2.2	Poisson's ratios at approximately 12% moisture content. From (Green, Winandy, & Krestschmann, 1999)	17
2.3	Values for the fracture energy perpendicular to the grain found in literature.	26
3.1	Series details.	33
3.2	Displacement rate during the loading process, where the range is given of the vertical displacement.	37
5.1	Average density of the testes samples at an estimated moisture content of 12%.	56
5.2	Total external work, cracked surface area and fracture energy for each sample including the average and standard deviation per series. (<i>Table continues on next page</i>)	57
5.3	The modulus of elasticity prior to and following the back-analysis.	59
5.4	The tensile strength prior to and following the back-analysis.	60
5.5	Correlation coefficients material properties.	61
5.6	Characteristic length and brittleness number of the test series.	62
5.7	Comparison of the mean and standard deviation values for the fracture energy of azobé with the estimated cracked area and the exact cracked area.	64
5.8	Mechanical properties for each series.	69
6.1	Element geometries.	74
6.2	Finite element types.	75
6.3	Linear elastic material properties.	78
6.4	Fracture properties.	78
6.5	Load steps.	79
7.1	Comparison of the reaction force for a vertical displacement of 1 mm between the numerical and analytical model.	99
7.2	Experimental and theoretical critical load for the series where Eq. 7.2 applies.	100
8.1	Influence of the growth ring orientation on the fracture characteristics and properties of azobé.	106

INTRODUCTION

1.1. Background

On November the 13th 2014 a 61-meter pedestrian bridge collapsed at the Wake Technical Community College, unfortunately killing one and injuring four more construction workers. The bridge was made of large glue-laminated timber beams, one example of an "engineered wood product". The use of timber products like glue-laminated timber, also known as glulam, have seen an increase in their use in construction in the last decade. The contribution of the ordinary construction materials (concrete and structural steel) to the emission of greenhouse gasses has led to a rapid transition to more sustainable construction materials and the trend to build in wood. However the problem arises that the desire to build in wood outpaces the ability to build in wood. Research on the strength and application of wood in construction is limited and many characteristics of wood are still unknown.



Figure 1.1: Wake Tech Community College timber bridge collapse. From (Van Voorhis, 2016).

The accident at the Wake Technical Community College is a good example where negligence and lack of knowledge resulted in the collapse of the timber beams. In Fig. 1.1 can be seen how the bridge collapsed. At the connection of the beams with the support a large horizontal crack propagated parallel to the beam axis, causing the top part of the beam to

separate from the bottom part. The cause of the failure as seen in Fig. 1.1 is in the way the connection of the beam-ends are designed. At the corner of the connection there is an irregularity in the geometry of the beam causing a sudden change in the stress flow. This causes a stress concentration in the corner of the beam which consequently could lead to crack formation. For steel and concrete this usually is not a big problem as steel is often not used in these types of connections and concrete is reinforced with steel bars to prevent failure. However, Fig. 1.1 exposes a major drawback of why building with wood did cause this failure: its lack of strength perpendicular to the grain.

Wood is an anisotropic material, meaning that its material properties vary for different directions of loading. Along the longitudinal (L) direction, the direction in which the tree grows and the wood fibres run, wood is significantly stronger than in the other two directions, the radial (R) and tangential (T) direction. Due to this anisotropy and the strong contrast in strength properties, the aim in timber engineering is to avoid loading in the weaker perpendicular to the grain direction. However, there are many engineering, utility and architectural reasons where this is unavoidable. In Fig. 1.2 a couple of examples are shown where the structural element is loaded in the perpendicular to the grain direction. In the picture of the Wake Tech accident (Fig. 1.1) we can recognise situation (a) of Fig. 1.2, the case of a notched end beam.

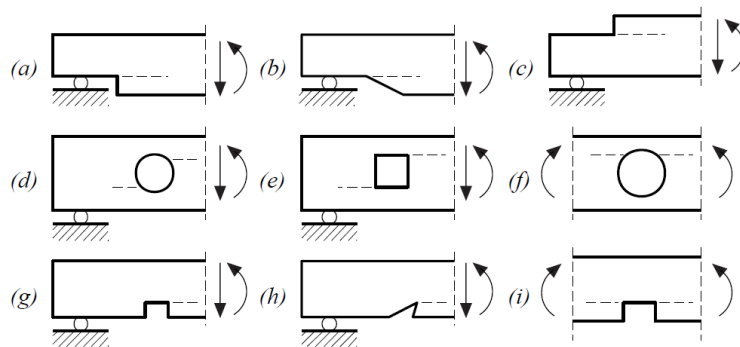


Figure 1.2: Notched beams and beams with holes where the structural members are loaded perpendicular to the grain. From (Blaß & Sandhaas, 2017).

1.2. Problem statement and scientific relevance

The design of structural elements is guided and prescribed by regulations and properties stated in (inter-)national building codes. In the Netherlands this is regulated by the European Union in the Eurocodes (EN). Timber is a material which just recently has been widely adopted by the construction industry. The prescribed material properties and formulas prescribed in the codes and regulations of the Eurocode are often purely based on empirical relations, relations that have been adopted by fitting a mathematical expression to test results (Serrano, n.d.). In the rapid increasing use of timber in construction, this poses the problem of situations which have not been tested before. This uncertainty often leads to an underestimation of the actual strength of wood products. In design this leads

to the overdimensioning structural elements which then leads to an unnecessary increase in building costs. Thus the problem is not only structural, where the weaker properties of wood perpendicular to the grain lead to a low overall strength and catastrophic fracture, but also design related, where the prescribed regulations are based on empirical relations and underestimated strength properties.

Recently more studies are performed on the material properties and fracture characteristics of wood. However, almost all of these studies have been based on experiments and theoretical models for softwood. Wood species are subdivided in two groups, softwood and hardwood. Most structural elements of timber are made of softwood because it is more readily available and cheaper due to its quicker development. The drawback however is that softwood is often less superior in strength and durability. Due to both these drawbacks, it is often much more desirable and efficient to build with hardwood. Examples where the strength and durability of the material is of the essence is in bridges, the exoskeleton of a building or sluice gates. But in general, wooden buildings are built with softwood. Therefore, tests are mostly performed on softwood, and thus their applicability to hardwood is still unknown. Moreover, most codes and regulations make no distinction between the use of their formulas for softwood or hardwood.

The problems described above pose a large research gap in the understanding of the fracture process perpendicular to the grain for hardwood. The aim of this research is to reduce this knowledge gap and have a better understanding of how wood in general, but more specific hardwood, fractures perpendicular to the grain. Based on fracture tests on several wood species, the relevant properties and characteristics can be determined which form the basis for a numerical and analytical models.

1.3. Scope

In this research the fracture process of hardwood is explored. That requires an extensive study on the parameters which describe and characterize the fracture process and the material resistance to cracking. For the quasi-brittle material wood, this involves an elaborate study on the fracture energy $G_{f,90}$, the tensile strength $f_{t,90}$ and the modulus of elasticity E_{90} (Aicher, 2009; Dourado et al., 2015; Larsen, 1990; Reiterer et al., 2002). Only the material properties are considered in the perpendicular to the grain orientation, denoted with 90 in the subscript of the parameters. The research is not only focused on obtaining the numerical values of the parameters but also how they relate to other properties of the wood specie. This is done by also exploring the cell structure and composition of the given wood specie. This research is defined by the following conditions and limitations:

- This research is only limited to fracture occurring due to tension. Although the test performed during this research is a bending test, which is a combination of tension and compression, the influence of compression is neglected. The influence of shear on the results of the experiment is discussed in Section 3.4.
- Only mode-I fracture is considered in this research. Mode-I fracture is the opening mode where the tensile stress is applied normal to the crack plane (Fig. 2.10). In Section 2.2 the fracture modes are explained in more detail. Assuming the tensile

stress to be normal to the crack plane, excludes any shear stress forming parallel to the crack plane. How this is achieved is discussed in Section 3.4.

- In this research only the perpendicular to the grain properties and characteristics of fracture are examined and evaluated. It is here assumed that the fibres run exactly perpendicular to the tensile stress at the fracture plane and the fibres are not stressed parallel to their orientation. This assumption is true if the highest principal stress is equal to the horizontal stress at a material point.
- This research does not take into account any time-dependent effects of the structural behaviour of wood, such as creep or relaxation. Moreover, loading conditions are quasi-static, meaning loading is applied over time but the inertial effects are ignored.
- This research is only focused on solid timber elements, other timber structural elements, such as glulam or laminated veneer lumber (LVL), are not covered (exceptions may be applied to the literature study).
- The experiments are performed with clear wood. At a size between 1 meter and 0.01 meter the wood samples are small enough to assume the absence of imperfections and/or irregularities such as knots. Samples larger than 1 meter are considered structural timber, and the assumption of clear wood no longer holds. In contrast to structural timber, clear wood has homogeneous material properties, meaning the physical and mechanical properties are uniform over the sample. In structural timber the imperfections and irregularities lead to weaker points in the material and thus lower mechanical properties.
- In this research the influence of moisture on wood is not treated. Wood is a hygroscopic material, meaning it absorbs moisture from the surrounding environment. The environmental conditions during the experiments are air-dry and the moisture content is assumed to be constant between 10 and 15%. In the literature study only a qualitative analysis of the relation between the moisture content and mechanical behaviour is performed. A quantitative analysis on the influence of the moisture content will not be tested and treated during this research.
- During this research the microscopic structure of wood is studied. This study is only limited to the microscopic level and does not expand to the submicroscopic level, where the composition of the cell types is described.
- In the problem statement (Section 1.2) the design of timber elements in buildings codes and regulations is mentioned. In this research the focus is only on Dutch and European codes and standards.

1.4. Research questions

The goal of this research is to reduce the knowledge gap of the fracture process and characteristics of hardwood. The knowledge gained with this research provides an answer to the main research question of this thesis:

Which parameters should be considered when describing the constitutive model of a (tropical) hardwood in mode-I tension?

Secondary research questions are presented to aid the research process and answer the main research question.

Literature review

1. How is crack propagation analysed and modelled in timber structural elements?
2. Which material properties are relevant in modelling the fracture process?
3. What are the differences in the fracture process between softwood and hardwood, and does the Eurocode make a distinction between the two groups?
4. How is fracture (of hardwood) currently taken into account in the strength verification in European codes and standards?

Experiments

5. Are the fracture observations seen during testing reflected in the material properties?
6. What is the fracture energy of (tropical) hardwood?
7. Can the linear relation between the density and the fracture energy determined for softwood be expanded to wood species with higher densities (hardwood)?
8. Is the fracture process dependent on the orientation and size of the hardwood samples?
9. Can the observations from this research be expanded to other hardwood species?

Numerical model

10. How can the results of this experiment be implemented in a discrete cracking model?

Practical implications

11. Can an analytical approach model the perpendicular to the grain fracture behaviour of wood accurately?
12. How do the results of this research influence the design considerations of timber structural elements?

1.5. Research approach

In this section the methodology to answer the main research question is presented. The purpose of this research is to determine the fracture characteristics of tropical hardwood related to its microscopic structure and growth ring orientation. This is done by studying multiple features of wood which characterize the fracture behaviour. A qualitative study is performed on the general mechanical behaviour, the anatomical features and observations from the fracture process. In addition, a quantitative study is performed to determine the mechanical properties which influence the fracture process. The separation between the two studies is illustrated in the flow chart in Fig. 1.3. In the figure the different parts of the research are shown and how they are connected throughout the research. The qualitative study is done in Chapter 4 and the quantitative study in Chapter 5.

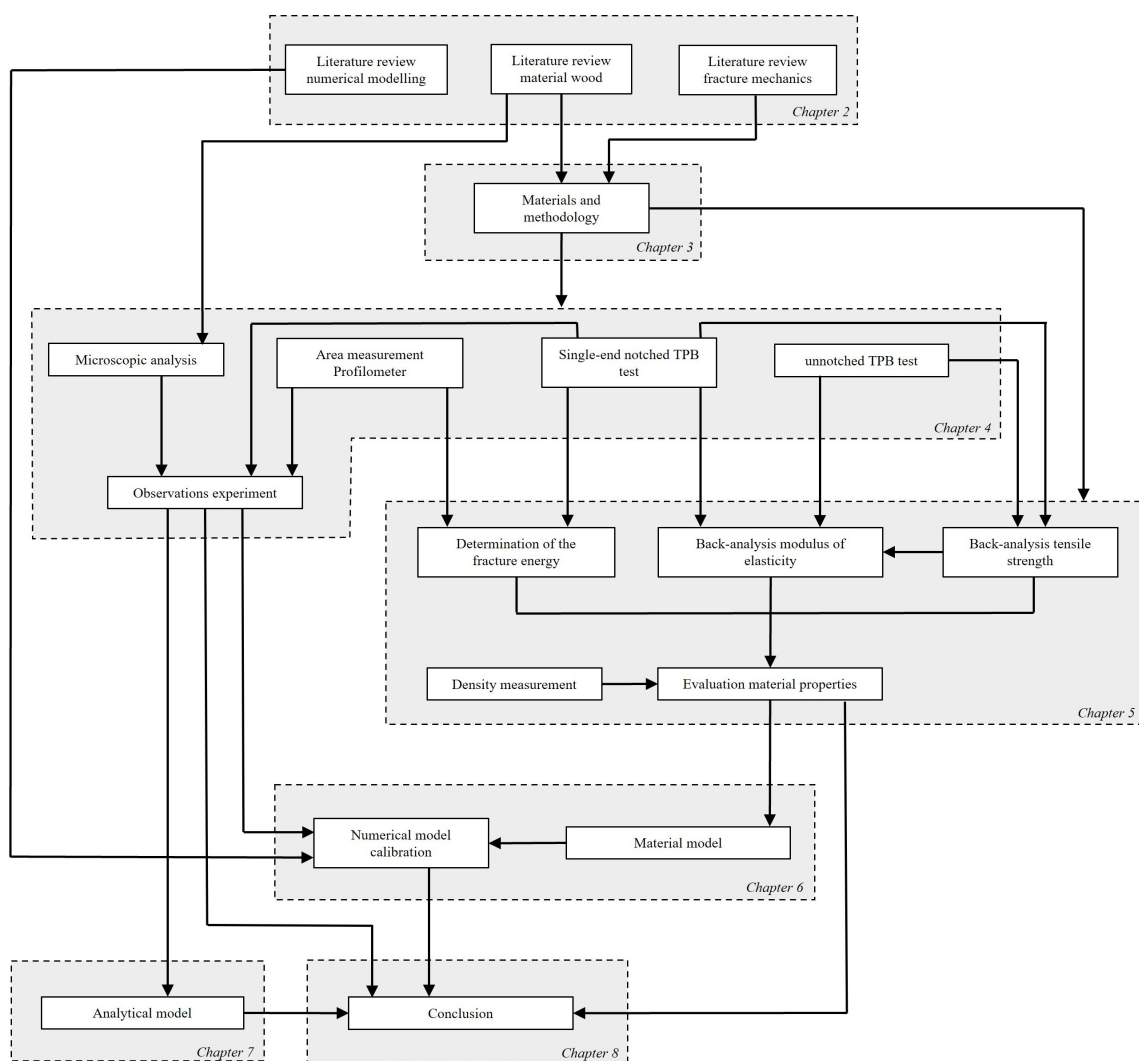


Figure 1.3: Flow chart research approach.

1.5.1. Qualitative analysis

The qualitative analysis consists of a study of the general mechanical behaviour, the anatomical features and the fracture surface. The goal of the qualitative analysis is to investigate the fracture process based on visual observations of the experiment which can not be quantified. The qualitative analysis is subdivided in three parts. The first analysis is a microscopic analysis, where not only the anatomical features of the different hardwood species are studied but also the path of crack propagation through the sample. Differences in the crack path on a microscopic level might give an indication of how the crack develops on structural element level. Secondly, an analysis is performed of the cracked surface area. This is done by a profilometer and a visual inspection. Similar to the microscopic analysis, a study of the crack plane gives an indication of how the crack propagates. Furthermore, the total cracked surface, obtained with the profilometer, is required to determine the fracture energy. Lastly, the load-displacement curve of the single-end notched TPB test is studied, which gives an indication of the overall stiffness throughout the fracture process.

1.5.2. Quantitative analysis

In the quantitative study mechanical properties which influence the fracture process are estimated. The goal of the quantitative study is to present estimate values of the properties which describe the constitutive law and are needed as input parameters in the material model in a numerical analysis. This research is focused on three material properties which describe the fracture behaviour, namely the modulus of elasticity of Young's modulus E_{90} , the tensile strength $f_{t,90}$ and the fracture energy $G_{f,90}$. All material properties are determined in the perpendicular to the grain orientation.

The method to determine the material properties is different. The fracture energy is the only property which can directly be determined with the single-end notched three-point bending test (SEN-TPB). The test setup of the fracture test and how the fracture energy is determined is described in Section 3.4. The modulus of elasticity (MoE) and tensile strength are indirectly determined with the results from the bending test and a back-analysis. The back-analysis is an iterative process where the material property considered is used as an input parameter in a numerical model and adjusted until the results of the numerical model coincide with the results from the experimental model. The back-analysis is a relatively comprehensive process which is described in more detail in Section 3.4.6.

1.5.3. Numerical model calibration

The third and final part of the research approach is the calibration of the numerical model. The qualitative study gives a broad view on how wood fractures and how the different properties influence the fracture process. On the other side, in the quantitative study the values of these properties are determined. Both studies are important in a numerical model. In the third part of this research, the observations of the qualitative and the numerical values from the quantitative studies are combined to evaluate existing models and calibrate them to accurately model the fracture behaviour of hardwood.

1.5.4. Theoretical approach

The last part of the thesis is focused on the practical implications of the report. In this chapter the conclusions of the experimental and numerical analysis are translated to a recommendation for practical applications. This also includes a parameter study where the influence of the mechanical properties on the peak load is evaluated and a theoretical approach to the problem where the cracking load is estimated based on linear-elastic beam theory.

1.6. Thesis outline

First, a literature review is performed in Chapter 2, which provides an overview of the current literature on the fracture characterization of (hard)wood. First basic characteristics of wood are explained. Here the anatomy of wood is explained and how softwood and hardwood are different from each other. After this introduction on the material wood, the mechanical properties of wood are explained, where the focus is on the elastic strength properties of wood, the modulus of elasticity and the behaviour in compression and tension. The second part of the literature review is on fracture mechanics. The general modelling of the propagation of cracks is explained. A distinction is made here between linear elastic fracture mechanics (LEFM) and non-linear fracture mechanics (NLFM), and how they are used in modelling the fracture process of wood. Next, advantages and drawback of current numerical and analytical models are presented.

In Section 1.5 a broad outline of the research methodology was given, visualized by the flow chart in Fig. 1.3. Here the methods of the thesis are presented. A detailed methodology of the research approach and the different methods used is given in Section 3.4. Here the details of the experiment and the exact procedure of the back-analysis is presented. Two bending tests are performed, an unnotched three-point bending test (Section 3.4.1) and a single edge notch three-point bending test (Section 3.4.2). Furthermore, the cracked surface area is measured using a profilometer (Section 3.4.3). Next, microscopic images are taken of the samples to investigate the cell structure and crack propagation path (Section 3.4.4). The density of the samples is measured (Section 3.4.5). And lastly, back-analyses are performed to determine the MoE and tensile strength (Section 3.4.6).

In Chapter 4 the results of the qualitative study are presented. This consists of a presentation of the general mechanical behaviour, the observations from the crack plane and the results from the microscopic analysis. These results are then evaluated and discussed in Section 4.4.

In Chapter 5 the results of the quantitative study are presented. Here the estimated values for the density, the fracture energy, the MoE and the tensile strength are presented. Then, these results are discussed by means of the a correlation coefficient and the relation to the results of the qualitative study in Chapter 4. At last, the conclusions of both studies are presented in Section 5.9.

The results of the experiment, both qualitative and quantitative, provide input for the numerical model. First, in Section 6.2 the material model is presented which is used in the numerical model. Results of the quantitative study provide the input for the material

model. Then in Section 6.3, the numerical model is calibrated and any improvements to existing models are suggested.

The last part of the research are design recommendations for structures built with timber. Chapter 7 consists of a parameter study (Section 6.4), an analytical model of the problem (Section 7.1) and a recommendation for designing with timber (Section 9).

LITERATURE STUDY

The literature study is comprised of two sections. The first section is focused on the material wood, where the anatomy and characteristics of the material are explained. In the second section the fracture mechanics of wood are explained and previous studies on the fracture behaviour of wood are treated. The purpose of the literature study is to present on the current knowledge and literature of the fracture behaviour of wood in general. Very little research has been performed on the fracture behaviour of hardwood and therefore literature on softwood is studied. From the literature study on softwood and a clear picture of the difference between softwood and hardwood, a hypothesis can be presented of the fracture behaviour of hardwood.

2.1. Material wood

To understand how wood deforms and fractures under load, the composition and characteristics of the material should be well documented and known. Due to the biological nature of the material, there is a large range of different wood species with each their own characteristics and compositions and this can lead to very different mechanical properties. A study on the anatomy and the characteristics of the material forms the basis from which the constitutive model can be understood.

2.1.1. Anatomy

Section planes

In contrast to the ordinary construction materials, wood is a biologically produced material and is formed by the environment where the tree lives. Wood is an anisotropic material, meaning that the material properties of wood depend on the orientation. Therefore, it is important to first define these orientations. In Fig. 2.1 a schematic representation of a wood section is given. The starting point here is the pith, which is the center and oldest part of the tree, the growth rings form around the pith. Similar to the x-,y-,z-axis in the Cartesian coordinate system, a three-dimensional orthogonal coordinate system is used for wood with the longitudinal (L), radial (R) and tangential (T) axis/direction.

The longitudinal direction is the direction in which the tree grows and we define as the "parallel to the grain" direction. The other two directions are orthogonal to the longitudinal

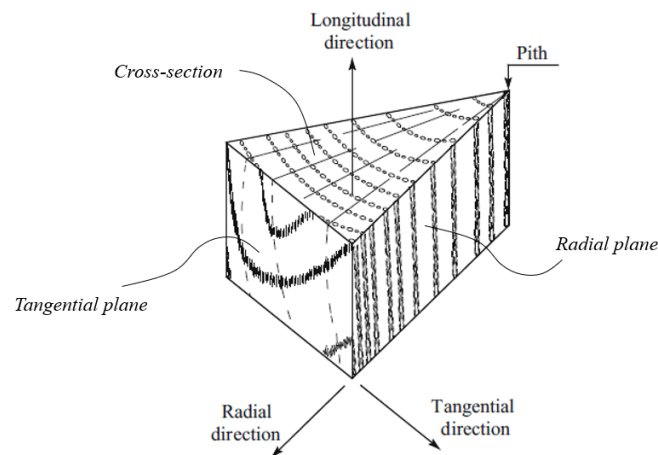


Figure 2.1: Section planes and wood axes: longitudinal (L), radial (R) and tangential (T). Adapted from (Dourado et al., 2015).

axis and is defined as the "perpendicular to the grain" direction. In this plane we define the direction outward from the pith, the radial direction, and the tangential to the annual rings direction orthogonal to the radial direction, the tangential direction. The three corresponding planes are the cross section (RT-plane), the radial plane (RL-plane) and the tangential plane (TL-plane). From the structure and composition in a given plane, we can identify the wood specie.

Softwood and hardwood

Wood can be divided in two main groups of plants: softwoods and hardwoods. Softwoods is wood from the *gymnosperm* which are better known as conifers or evergreens. Hardwoods come from the *angiosperm* and are mostly deciduous, meaning "tending to fall off" (of the leaves). Note that not all hardwoods are deciduous, some tree in the tropics are also evergreens. The contrast in structure and composition between the two groups has to due with the climate the tree are typically found. Softwoods often grow in the colder more variable climates, whereas hardwoods typically grow in more temperate and tropical areas around the equator. In Fig. 2.2 a schematic representation of the two groups is shown. Softwood is mostly comprised of two cell types, tracheids and parenchyma cells. For most softwood types the longitudinally orientated tracheids have a volume fraction of 90 to 95% (Blaß & Sandhaas, 2017). The function of the tracheids in softwood is not only to give the tree strength but also to for sap and water conduction. In Fig. 2.2a two different sizes of tracheids can be distinguished. The larger sized tracheids, called earlywood, are formed in the spring when there are long days and enough water and nutrients in the soil for the tree to grow. The smaller tracheids called latewood is formed in the winter when, especially in the colder climates, the conditions can be harsh and the tree goes dormant. This is the beauty of this biological material where can see back in time and see what the tree has been through.

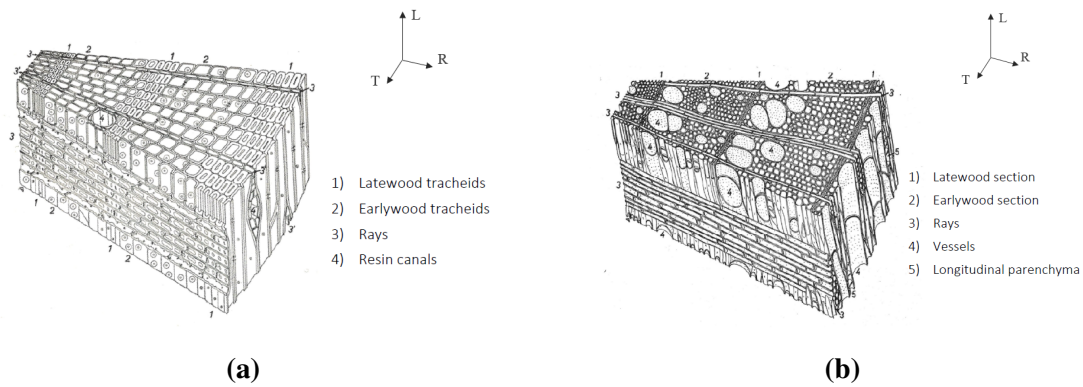


Figure 2.2: Schematic illustration of the microscopic structure of (a) softwood and (b) hardwood. Adapted from (Blaß & Sandhaas, 2017).

For hardwood this distinction between the seasons is much less pronounced due to the more constant climate around the equator. In contrast to softwood, hardwood has a much more complex and extensive anatomy. Softwood mainly consisted of longitudinal tracheids which had multiple functions. Hardwood has multiple cell types, each with its own function. In the longitudinal direction we make a distinction between three cell types: vessels, parenchyma and fibers. The vessels, or pores as it is commonly referred to, are the large holes in the wood which conduct the water. Similar to the annual rings in growth rings in softwood, can the arrangement of pores can tell much about the climate a tree lives in. For hardwood trees around the equator the climate is fairly constant, which results in a homogeneous distribution of the pores, these trees are called diffuse porous. Hardwood trees which grow in a more temperate climate the vessels are more aligned in rings as a result of the oscillation in climate conditions. These trees are called ring-porous. In this research this distinction can be seen in the structure of oak (ring-porous), Fig. 2.3a, and azobé (diffuse-porous).

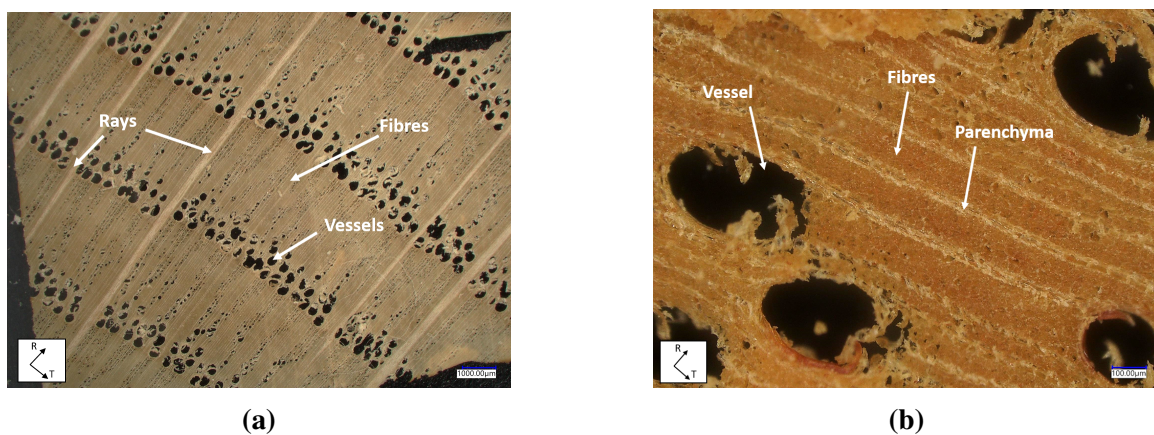


Figure 2.3: Microscopic structure of (a) oak and (b) bilinga.

The second cell type are the longitudinal orientated parenchyma cells, which serve as storage cells. The volume fraction of the parenchyma cells differs widely per wood species,

for oak (Fig. 2.3a) the parenchyma cells are almost non-existent whereas for bilinga (Fig. 2.3b) they can easily be spotted. The last cell type in hardwood are the fibers, which are thick and strong cells which support the tree. For most hardwoods the fibers make up the majority of the trees cross-section and result in a stronger wood than softwood. In contrast the tracheids in softwood which run almost parallel, the fibers are often orientated in a very complex and interlocking manner resulting in higher strength, which is the case for azobé (Fransen, 2016). In the radial direction softwood and hardwood are comparable. In both wood groups the radial direction is comprised of rays which are radially orientated parenchyma cells that transfer nutrients and water. The difference however is that in softwood the rays are usually one or two cells wide, called uniseriate and biseriate, whereas for hardwood these bands are usually multiseriate, meaning they are comprised of multiple cells. In Tab. 2.1 the volume fraction of the cell types are shown for the wood species that are tested in this experiment.

Table 2.1: Microscopic structure of wood species (Wagenführ & Scheiber, 2006).

Wood specie	Volume fraction (vol%)				
	Vessels	Parenchyma	Rays	Fibers	Tracheids
Spruce	N/A	1.5 - 5.8	4.0 - 7.0	N/A	94.5 - 96.5
Oak	3.9 - 13.0	2.8 - 8.1	14.4 - 17.9	50.0 - 60.0	N/A
Bilinga	11.0 - 16.0	6.0 - 7.0	22.0 - 23.0	55.0 - 60.0	N/A
Azobé	7.7 - 10.6	17.7 - 20.5	12.3 - 14.0	57.2 - 60.8	N/A

To summarise, softwood (Fig. 2.2a) is in the longitudinal direction almost completely comprised of one cell type, the tracheids, which stores and conducts the trees sap and strengths the tree. In hardwood (Fig. 2.2b) these functions are subdivides over three components of the cross-section: the vessels, the parenchyma cells and the fibers. In the radial direction wood is comprised of rays, short for radially orientated parenchyma cells, which transfer the trees sap radially. In softwood these rays are only one or two cells wide and in hardwood usually more.

2.1.2. Wood characteristics

The previous section made clear that there is a large variation in the anatomy of wood species. Between softwood and hardwood there are different cell types with each its own purpose in the tree. Also, the presence of these cell types might very significantly per wood specie, for example in Fig. 2.3 a clear distinction can be seen in the presence of the longitudinal parenchyma which are almost absent in oak and very present in bilinga. The variation between in the cell composition of the tree also leads to a variation in the mechanical properties of the wood specie. In this section the causality between the anatomy and the mechanical properties of wood is inspected.

Density

Due to the diverse purpose of the longitudinal tracheids mentioned in Section 2.1.1, softwood is generally less strong than hardwood which is mainly composed of fibers with the sole purpose to strengthen the tree. Therefore, the dry density of hardwood is usually higher than softwood. The density¹ of softwood ranges from 350 to 520 kg/m³ and of hardwood from 570 to 1080 kg/m³ (European Standard, 2016). In this research spruce, oak, bilinga and azobé are tested, which have an average density of 460, 640, 740 and 960 kg/m³ respectively. Note that these values are based on their categorization in the Eurocode (European Standard, 2016, 2012), their exact values of the specimen are determined during the experiment and stated in Section 5.1. The variation in density between the wood species has a large influence on the hygroscopicity, durability and fire resistance of wood. These characteristics are presented in the next sections.

Hygroscopicity and durability

Hygroscopicity is defined as the ability of the material to absorb moisture. This is important because the strength and fracture characteristics of wood are dependent on the moisture content (Ravenshorst, 2015; Reiterer & Tschegg, 2002; Blaß & Sandhaas, 2017). Hoffmeyer and Andriamitantsoa state in (Blaß & Sandhaas, 2017) that the compression and tensile strength perpendicular to the grain change 5 and 2% respectively with 1% change in moisture content. The study by Reiterer (2002) concludes that a higher moisture content leads to an increase in fracture energy due to an increase in ductility. Furthermore, the study concludes that the linear elastic stiffness and maximum stress state decrease with an increase in moisture content. In general it can be concluded that the higher the moisture content the weaker and more ductile the wood sample will react to the external load. The influence of the moisture content on the fracture behaviour is studied by Boerenveen (2019). He conducted a similar fracture test on bilinga and azobé samples with a moisture content between 10-15% (dry) and samples between 25-40% (wet). The results by Boerenveen (2019) demonstrate a significant difference in the mechanical behaviour between the dry and wet samples. The peak load of both wood species reduced a factor two when considering the wet samples. Furthermore, the fracture energy (Section 2.2.2) of the wet azobé samples is on average a factor 1.43 lower than the dry samples. For bilinga the difference in the fracture energy between the wet and dry samples is less pronounced, the fracture energy of the wet samples is a factor 1.09 lower than the dry samples on average. Note that these ratios are all considering a flat fracture plane. In this research the exact surface area of the fracture is measured, thus no definitive conclusions can be drawn from the ratio's between the dry and wet fracture energy values. A quantitative analysis of the influence of the moisture content on the mechanical properties is outside the scope of this research and will not further be investigated. Due to the hygroscopic nature of wood and the variation in the density, the choice of wood specie is important when considering durability and fire resistance. This is discussed in the next section.

¹The given values are compatible with timber at moisture content consistent with a temperature of 20 °C and a relative humidity of 65%, which corresponds to a moisture content of 12% for most species (European Standard, 2016).

Thermal properties and fire resistance

The thermal properties and combustibility of wood is a complex topic and the resistance to fire depends on many factors. In buildings, the resistance to fire is mainly determined by: the availability of oxygen in the environment, the size of the structural element, magnitude of loading and the density of the wood specie (Blaß & Sandhaas, 2017). Extensive research has been performed on the influence of these factors on the first resistance of wood. The thermal properties and fire resistance of wood is outside the scope of this research and thus the relation between fire and fracture is not investigated in this report.

Elastic properties

For isotropic materials the stiffness is only defined by the two linear elastic constant, the Poisson's ratio ν and the modulus of elasticity E . As mentioned before wood is considered to be an anisotropic material where the two linear elastic constants are not independent of the direction of loading. The modulus of elasticity (MoE) has to be expanded to the three orthogonal direction resulting in three separate stiffness values: E_L , E_R and E_T . It is important to note that the stiffness anisotropy is now expanded from two directions to three directions. Previously, wood was characterized by a strong direction and a weak direction, parallel and perpendicular to the grain respectively. It was assumed that in the perpendicular to the grain plane, i.e. the cross-section (Fig. 2.1), the material is isotropic. The scope of this research is limited to the perpendicular to the grain orientation, and the difference between the stiffness in the radial and tangential direction is no longer negligible. In the Eurocode this distinction is not made, and only the parallel and perpendicular to the grain stiffness values are prescribed (European Standard, 2016). Moreover, these values are based on bending tests and the MoE value parallel to the grain. The perpendicular to the grain stiffness values are based on the following equations:

$$\begin{aligned} E_{90,mean} &= E_{0,mean}/30 && \text{for softwoods} \\ &= E_{0,mean}/15 && \text{for hardwoods} \end{aligned} \quad (2.1)$$

In the standard no distinction is made between the MoE in tension or in compression. Kovryga, Stapel and Van de Kuilen (2020) report that the difference between the MoE in tension and compression is approximately 10%. Also, the difference between the stiffness in the radial and in the tangential direction will not be neglected and therefore the stiffness is characterized in the L-,R- and T-direction and not in the 0-,90- direction. From various literature (Carrington, 1923; Danielsson, 2013; Green et al., 1999) the following relations can be found between the radial and tangential stiffness with respect to the longitudinal stiffness. These relations are based on wood species at 12% moisture content. For softwood,

$$\begin{aligned} E_R &\approx E_L/12 \\ E_T &\approx E_L/20 \end{aligned} \quad (2.2)$$

and for hardwood,

$$\begin{aligned} E_R &\approx E_L/8 \\ E_T &\approx E_L/17 \end{aligned} \quad (2.3)$$

This results in the following relation between the stiffness in the radial and the tangential direction: for softwood $E_T \approx 1.7E_R$, and for hardwood $E_T \approx 2.1E_R$. Note that there is a large variation between wood species, and that these values give an indication of the relation between the stiffness in the different orientations. In Fig. 2.4 the MoE is shown in relation to the orientation of the growth rings. It can be seen that the orientation has a significant influence on the stiffness, and that the variation in the perpendicular to the grain can not be ignored. Most of these relations are based on either bending tests or derived from the density of the wood species. Little to no research has been performed on the perpendicular to the grain properties with a uni-axial test, the proper way to determine these values.

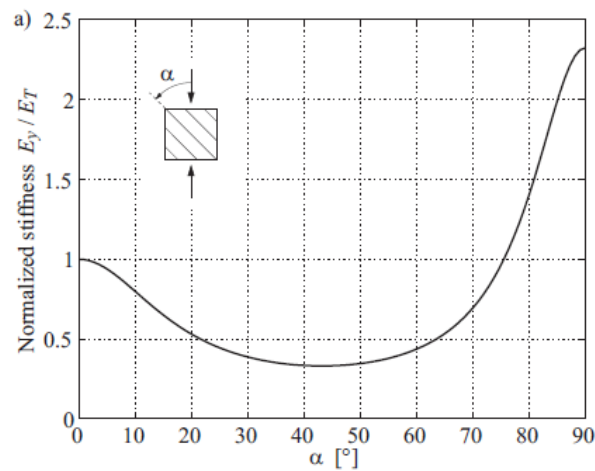


Figure 2.4: Influence of the orientation of the growth rings on the modulus of elasticity for softwoods. From (Danielsson, 2013).

The second elastic property is the Poisson's ratio. Not much literature is available on the Poisson's ratio for hardwood. In practical applications or finite element simulations usually a uniform Poisson's ratio is used, and not much attention is given to the different orientations. In Green (1999) the Poisson's ratio is given for well known wood species in the United States. In the table below, only the values for spruce and oak are shown. In the table the first index in the subscript stands for the direction in which the stress is applied, and the second index is the direction of the strain.

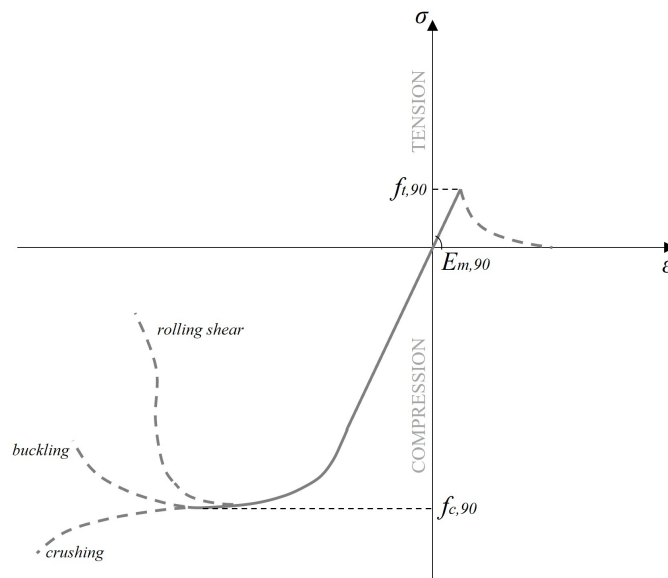
Strength properties

The strength values for wood vary widely depending on the load direction. For wood the stress-strain curve is different in the parallel and the perpendicular to the grain orientation. In this research the focus is only on the perpendicular to the grain orientation. In Fig. 2.5 a typical stress-strain curve is shown for wood loaded perpendicular to the grain. The

Table 2.2: Poisson's ratios at approximately 12% moisture content. From (Green et al., 1999)

	Spruce	Oak
μ_{LR}	0.422	0.350
μ_{LT}	0.462	0.448
μ_{RT}	0.530	0.560
μ_{TR}	0.255	0.292
μ_{RL}	0.083	0.064
μ_{TL}	0.058	0.033

difference between the strength properties in the radial and tangential direction is still unknown. Hence, the graph only shows the perpendicular to the grain orientation and makes no distinction between the radial and tangential direction.

**Figure 2.5:** Typical perpendicular to the grain stress-strain curve for clear wood. Adapted from (Fransen, 2016; Blaß & Sandhaas, 2017).

This research is only focused on the behaviour of wood in tension. For the behaviour in compression data is adopted from (Fransen, 2016) and (European Standard, 2016). According to these references for softwood $f_{c,90,k} \approx 6f_{t,90,k}$ and for hardwood $f_{c,90,k} \approx 13f_{t,90,k}$. This relation is an average of multiple species and can vary per wood specie. For example in the study by Kovryga, Stapel van de Kuilen (2020) the compression values found for ash and beech are approximately twice the strength in tension.

In Fig. 2.5 a clear distinction between the mechanical behaviour in the tension and compression regime can be seen. In many researches and literature, wood is considered to behave brittle in tension and ductile in compression. However realistically the the mechan-

ical behaviour of wood is slightly more nuanced. According to Fransen (2016) the strength of wood in compression depends on the failure mode. In compression three failure modes are considered, also illustrated in Fig. 2.5, namely: rolling shear, buckling and crushing. The strength in compression is assumed to be constant but once the compression strength is reached, the mechanical behaviour is heavily dependent on the failure mode.

In tension the fracture behaviour is not fully brittle, but can be considered to be more quasi-brittle. Due to the biological and fibrous nature of the material, there are multiple non-linear phenomena taking place during loading. These phenomena are mainly fiber-bridging and micro-cracking (Aicher, 2009; Dourado et al., 2015; Reiterer et al., 2002; Stanzl-Tschegg et al., 1995). Micro-cracking occurs when very small defects or imperfections in the wood are stressed and cause the stress in a material point to reduce. Fiber-bridging is the phenomena where the fibers in a fibrous material "cross-over" to the other side of the crack. A schematic and realistic representation of fiber-bridging in a carbon-fiber reinforced composite is shown in Fig. 2.6. The fiber-bridging mechanism is similar in wood as in the carbon-fiber reinforced composite in the figure.

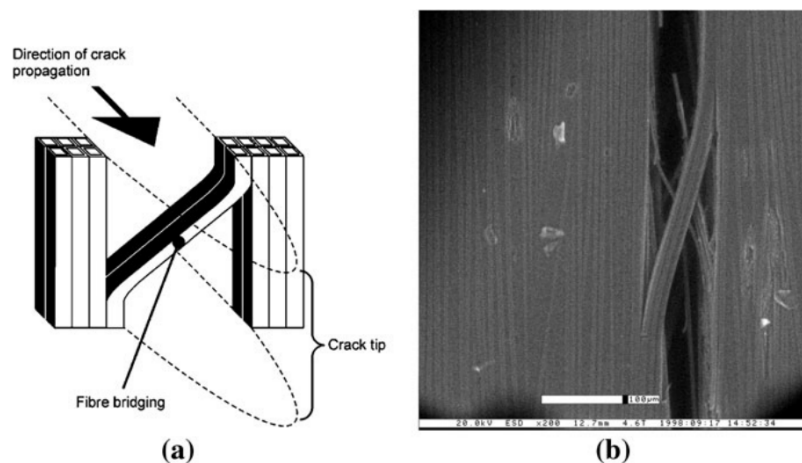


Figure 2.6: (a) Schematic illustration and (b) scanning-electron micrograph of crossover fibre bridging in a carbon-fibre reinforced composite. From (Gamstedt et al., 2012).

Instead of brittle failure and the formation of a traction-free crack once the tensile strength is reached, these phenomena are "activated" once the tensile strength is reached. In tension wood can thus be considered quasi-brittle, where tension softening takes place due to non-linear phenomena. The exact fracture process and how these non-linear phenomena are modelled is further discussed in Section 2.2.

In the Eurocode a characteristic tensile strength value of 0.4 N/mm^2 for softwood and 0.6 N/mm^2 for hardwood is listed (European Standard, 2016). These values are not based on any testing results, but instead a uniform conservative value is assumed. To obtain an accurate value for the tensile strength, a uni-axial tensile test needs to be performed. Kovryga et al. (2020) performed an uni-axial tensile test on beech and ash. The results are presented in Fig. 2.7. Literature on the perpendicular to the grain properties of hardwood is very limited.

Similar to the Eurocode, Kovryga et al. (2020) proposes a single value for the tensile

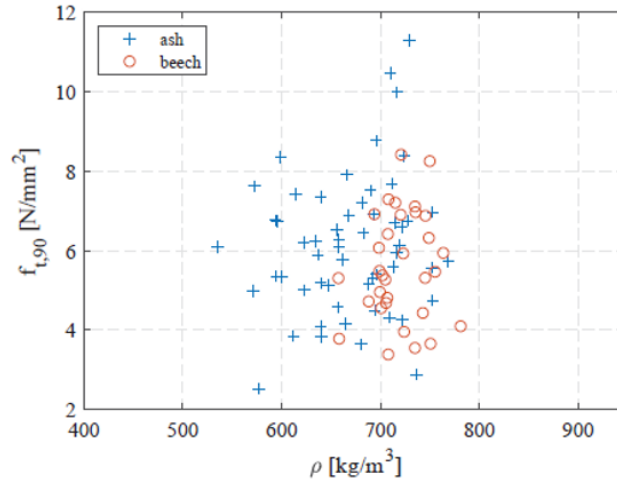


Figure 2.7: The tensile strength perpendicular to the grain for beech and ash. From (Kovryga et al., 2020)

strength perpendicular to the grain for medium-dense hardwood species. Literature on the mechanical properties perpendicular for softwood is more extensive. Literature gives a range for the tensile strength perpendicular to the grain for spruce between 2 and 5 N/mm² (Berblom Dahl, 2009; Schmidt & Kaliske, 2009), significantly higher than the 0.4 N/mm² prescribed by the Eurocode. Both references also state the tensile strength in the radial direction is approximately 1.5 times higher than in the tangential direction.

Although most wood properties are considered to be constant, the tensile strength is size-dependent. The tensile strength declines when the sample size increases. In the case of brittle failure, usually the case in tension and shear, defects and imperfections form a weak link in the specimen and the larger the specimen, the larger the amount of weak links. In the Eurocode the size effect is taken into consideration with the parameter k_h . For structural elements with a height above 150 mm, the strength is multiplied with the parameter k_h .

2.1.3. Constitutive model

The constitutive model of a material describes the response of the material to external stimuli. In the case of wood the constitutive model is relatively complex from other material due to its anisotropy and tension-compression asymmetry. In this research only the constitutive model is described in the perpendicular to the grain tension loading.

Wood in tension is often characterized as brittle (Blaß & Sandhaas, 2017; Danielsson, 2013), neglecting the non-linear phenomena and tension softening described earlier. However due to these non-linear phenomena, the material wood exhibits tension softening, which can be characterized as quasi-brittle. In a quasi-brittle constitutive model we can characterize two stress states, the linear-elastic stress state and the softening stress-state. In the linear-elastic stress state no point in the material has reached the tensile strength. In the linear-elastic state, both the stress and the strain increase. Once the tensile strength has been

reached, the considered material point(s) enter the softening state, where the stress reduces while the strain or relative displacement increases. These two states of the constitutive model are illustrated in Fig. 2.8.

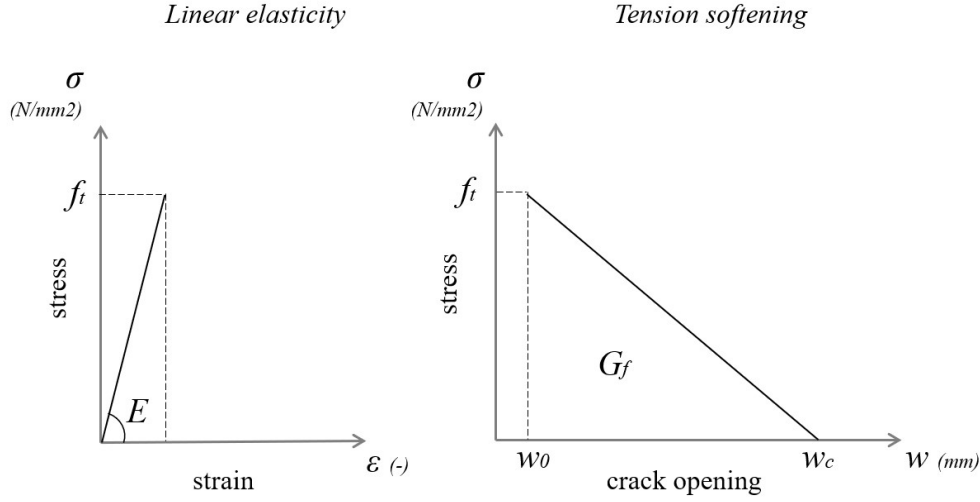


Figure 2.8: The constitutive model for a quasi-brittle material.

Linear regime

In linear elasticity the stress-strain curve is described by the modulus of elasticity, the slope of the curve, and the tensile strength. In the most general form the constitutive equation in the linear regime is described by Hooke's law Eq. 2.4.

$$\bar{\sigma} = \bar{D}\bar{\varepsilon}^e \quad (2.4)$$

In this equation the stiffness tensor \bar{D} is introduced, which describes the relation between the stress tensor and the elastic strain tensor. In modelling wood, the use of an anisotropic constitutive model is too complex as then 36 elastic constants have to be described. Therefore, wood is usually described as an orthotropic material, where the material has three orthogonal planes of symmetry (Fig. 2.1). Sometimes, wood is modelled as a transverse isotropic material reducing the number of elastic constants to five. However, in a transverse isotropic model the elastic constants E_R and E_T are assumed to be equal. Thus the orthotropic constitutive model in the elastic regime is reduced to Eq. 2.5.

$$\begin{bmatrix} \varepsilon_{LL} \\ \varepsilon_{RR} \\ \varepsilon_{TT} \\ \gamma_{LR} \\ \gamma_{LT} \\ \gamma_{RT} \end{bmatrix} = \begin{bmatrix} \frac{1}{E_L} & -\frac{\nu_{RL}}{E_R} & -\frac{\nu_{TL}}{E_T} & 0 & 0 & 0 \\ -\frac{\nu_{LR}}{E_L} & \frac{1}{E_R} & -\frac{\nu_{TR}}{E_T} & 0 & 0 & 0 \\ -\frac{\nu_{LT}}{E_L} & -\frac{\nu_{RT}}{E_R} & \frac{1}{E_T} & 0 & 0 & 0 \\ 0 & 0 & 0 & \frac{1}{G_{LR}} & 0 & 0 \\ 0 & 0 & 0 & 0 & \frac{1}{G_{LT}} & 0 \\ 0 & 0 & 0 & 0 & 0 & \frac{1}{G_{RT}} \end{bmatrix} \begin{bmatrix} \sigma_{LL} \\ \sigma_{RR} \\ \sigma_{TT} \\ \tau_{LR} \\ \tau_{LT} \\ \tau_{RT} \end{bmatrix} \quad (2.5)$$

Softening regime

The second part of the constitutive model is the tension softening regime. This part of the constitutive model is not described by a stress-strain relation but by a stress-displacement relation. The tension softening regime is characterized by the non-linear phenomena mentioned earlier, fiber-bridging and micro-cracking. These phenomena are not described by a stiffness modulus but by an energy related parameter. The tension softening behaviour is described by the fracture energy G_f , which is a function of the external work and the cracked area. More on the fracture energy in Section 2.2. The energy approach is in contrast with the continuum damage mechanics (CDM) approach, where the tension softening is also described by the stiffness modulus. The non-linear phenomena are now described by a damage parameter, which reduces the elastic stiffness parameter E (Sandhaas, Sarnaghi, & van de Kuilen, 2020). In this research the tension softening is only modelled with the fracture energy approach, not by the CDM approach.

In Fig. 2.8 the tension softening law is depicted as a linear relation. For wood the tension softening curve can better be modelled by an exponential or bi-linear softening curve (Boström, 1992; Dourado et al., 2015; Stanzl-Tschegg et al., 1995). In a bi-linear tension softening model, the softening curve can be subdivided in two parts. The first part belonging to the phenomena of micro-cracking and the second part to fiber-bridging. In Fig. 2.9 this is illustrated in the bi-linear model.

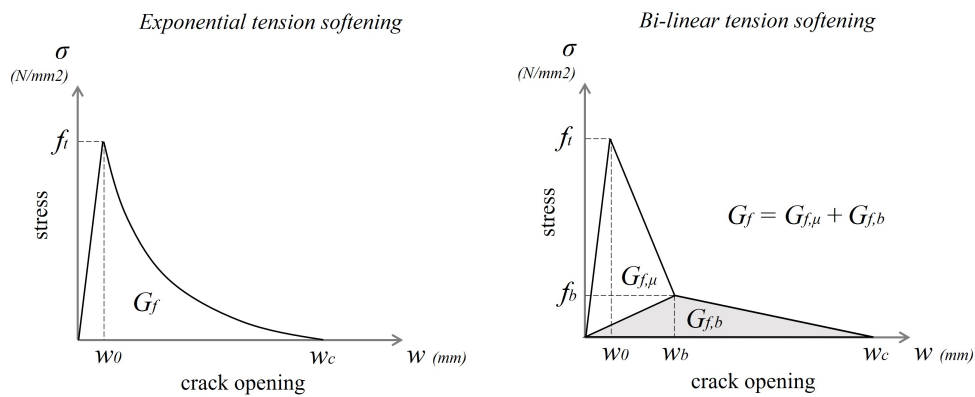


Figure 2.9: The exponential and bi-linear tension softening models for a numerical model. Adapted from (Stanzl-Tschegg et al., 1995).

In the bi-linear softening model, micro-cracking and fiber-bridging have a separate contribution to the total energy which is being released by the fracture process, indicated by $G_{f,\mu}$ for micro-cracking and $G_{f,b}$ for fiber-bridging. This constitutive model requires three additional material properties, the fracture energy corresponding to the micro-cracking and the fiber-bridging components and the stress or cracking opening displacement at which the transition between both models takes place. This requires an elaborate study on the non-linear phenomena which are hard to identify with ordinary fracture and strength test setups. In (Stanzl-Tschegg et al., 1995) an approximation is done using numerical models. The study concludes that the energy consumed by the fiber-bridging component is larger than the micro-cracking component, $G_{f,b} > G_{f,\mu}$. Furthermore, the study concludes that

the energy component of fiber-bridging is larger in the radial direction than in the tangential direction. Note, that this is based on a study on softwood (spruce), where firstly, there is the distinction between early- and latewood and secondly the anatomy is significantly different from hardwood. Hence, the contributions of fiber-bridging and micro-cracking for hardwood is still unknown and difficult to determine. Bostrom (1992) approximates that the break-point in the bi-linear softening curve is at the coordinate (0.20, 0.12), meaning the fiber-bridging occurs at a stress $0.20f_t$ and a relative displacement $0.12w_c$.

2.2. Fracture mechanics

Fracture mechanics is a field of mechanics concerning the formation and propagation of cracks in a material. Fracture mechanics is different from conventional stress criterion. According to linear elasticity theory the stress at a notch or crack tip is infinity. The capacity of a structural member can thus not be modelled with conventional stress criteria where the strength is finite. There are two general methods to model the infinite stress at the crack tip and model the crack propagation, linear elastic fracture mechanics (LEFM) and non-linear fracture mechanics (NLFM). In LEFM the stress state around the notch or crack tip is described by a single parameter, the stress intensity factor K or the energy release rate G . In NLFM the stress state is modelled by a fracture process zone and described by a constitutive model. Both approaches are discussed in the next sections.

First, the different types of fracture are presented. In fracture mechanics four possible fracture modes are considered: the opening mode (mode-I), the sliding or in-plane shear mode (mode-II), tearing or out-of-plane shearing mode (mode-III). The last mode is a mixed mode where a combination of prior mentioned modes occurs. The three main modes are illustrated in Fig. 2.10. The scope of this research is only on the opening mode, the pure tension mode-I fracture.

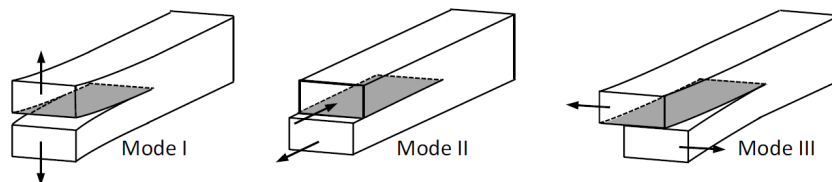


Figure 2.10: Fracture modes. From (Blaß & Sandhaas, 2017).

Because of the unsymmetrical nature of wood different fracture systems can be recognised. In Fig. 2.11 the six possible crack propagation systems are illustrated. A crack propagation system is indicated by two letters, the first of which is the direction which is normal to the fracture plane, and the second is the direction in which the crack propagates. In the case of perpendicular to the grain fracture, only two systems are important, the RL and TL fracture systems. In Fig. 2.11 these two are highlighted.

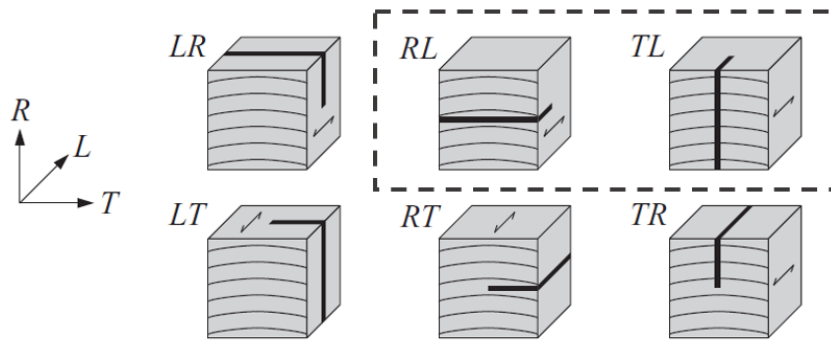


Figure 2.11: Crack propagation systems. From (Danielsson, 2013)

2.2.1. Linear elastic fracture mechanics

In linear elastic fracture mechanics the formation and propagation of cracks is based on an energy balance, first developed by Griffith (1921). In the energy balance Eq. 2.6 the total energy of the system Π is equal to the sum of the strain energy U_s , the potential energy by the external load U_p , which is equal to the work by the external load, and the energy which goes into crack propagation U_c .

$$\Pi = U_s + U_p + U_c \quad (\text{Nmm}) \quad (2.6)$$

According to Griffith (1921) a crack will propagate if the total energy is unchanged or reduced. Rewriting Eq. 2.6 yields the function of the energy release rate, which is the energy available to grow a crack a unit area (Smith, Landis, & Gong, 2003).

A limitation of LEFM is that it accepts that the stresses at the notch or crack tip are theoretically infinity. The acceptance of the stress going to infinity is only possible when the plastic or cohesive zone is equal to zero. The cohesive zone is the part ahead of the traction-free crack where the non-linear phenomena micro-cracking and fiber-bridging are developed. So, the assumption of a cohesive zone with size zero is a reasonable assumption in the case of a fully brittle material, where these non-linear phenomena do not occur. Wood is quasi-brittle and the non-linear phenomena, and thus the size of the cohesive zone, can not be neglected. LEFM is thus an inaccurate and unsuitable method to describe a quasi-brittle material (Benabou & Sun, 2015; Boström, 1992; Smith et al., 2003). LEFM is better suited as an analytical tool where the physical processes in the FPZ can be ignored (Smith et al., 2003). In non-linear fracture mechanics (NLFM) the size of the cohesive zone is not equal to zero, which makes it a better method to model fracture in wood.

2.2.2. Non-linear fracture mechanics

In contrast to LEFM, non-linear fracture mechanics (NLFM) does not follow the theoretical infinite stress, but instead adopts the quasi-brittle softening model as shown in Fig. 2.5, where non-linear phenomena contribute to a tension softening in the material. The area where the tension softening develops is the before mentioned cohesive zone. Other appl-

lations of this zone are plastic zone or fracture process zone, all indicating this non-linear process zone.

Fictitious crack model

In the non-linear fracture mechanics field the fictitious crack model is an approach which is often chosen. The fictitious crack model is developed by Hillerborg (1978) and takes into account the non-linear phenomena with a fictitious crack forming ahead of the "real" traction-free crack. The fictitious crack model is also referred to as the cohesive zone model (CZM). In the fictitious crack model three phases of material state are distinguished (Hillerborg, 1978). The three phases are illustrated in Fig. 2.12.

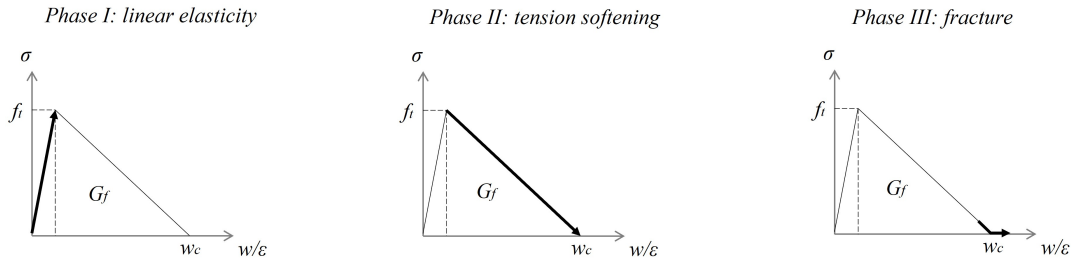


Figure 2.12: The three phases which can be distinguished when a material point is loaded until fracture

The first phase describes a material point during the linear elastic state, where the tensile strength of the considered point has not yet been reached. During this phases, the constitutive model is described by the linear elastic stress-strain relation of the material. The load is increased and the stress in the material point increases until the tensile strength has been reached. The moment the tensile strength is reached, the material point enters the second phase, during which the material develops micro-cracking and fiber-bridging. During the tension softening phase a cohesive zone is formed. All the points in this cohesive zone are in the second phase. The micro-cracking and fiber-bridging processes lead to the formation of a fictitious crack. The relation between the stresses and the opening displacement of the fictitious crack is defined by the tension softening relation, as mentioned in Section 2.1.3. The area under the stress-crack opening curve is the fracture energy (Hillerborg, 1978):

$$G_f = \int_0^{w_c} \sigma(w) dw \quad (\text{N/mm}) \quad (2.7)$$

In the tension softening state the stress in the material point decrease until it has reached zero stress. This is the point where a traction-free crack is formed and the third phase, the fracture phase, is entered. At the point the crack opening displacement has reached a critical value, the critical crack-opening displacement w_c .

To illustrate how the fictitious crack model and the tension softening state influence the stress distribution during loading, Fig. 2.13 shows how the horizontal stress distribution over the height changes during the loading and fracture process. In the figure the three material states can be distinguished for a material point at notch end. In the first phase the

horizontal stress distribution over the height is linear elastic as no material point has reached the tensile strength in the tension zone and the compression strength in the compression zone. Once a material point has reached the tensile strength, it enters the tension softening regime, see Fig. 2.12, and the stress reduces. When the loading process proceeds, i.e. the applied displacement at mid-span increases, the point where the stress is equal to the tensile strength moves up along the beam height and the stress at the notch end decreases until it has reached zero stress. The material point is now traction-free and a crack is formed. Again proceeding the loading process, both the point where the tensile strength is reached and the point where the traction is zero move up along the beam. The zone between these two points is the cohesive zone. In this zone all material points are in the tensions softening regime of the constitutive law (Fig. 2.12). Note that here the assumed shape of the tension softening curve is linear. If the shape of the tension softening curve is different, the stress distribution in the cohesive zone will be different.

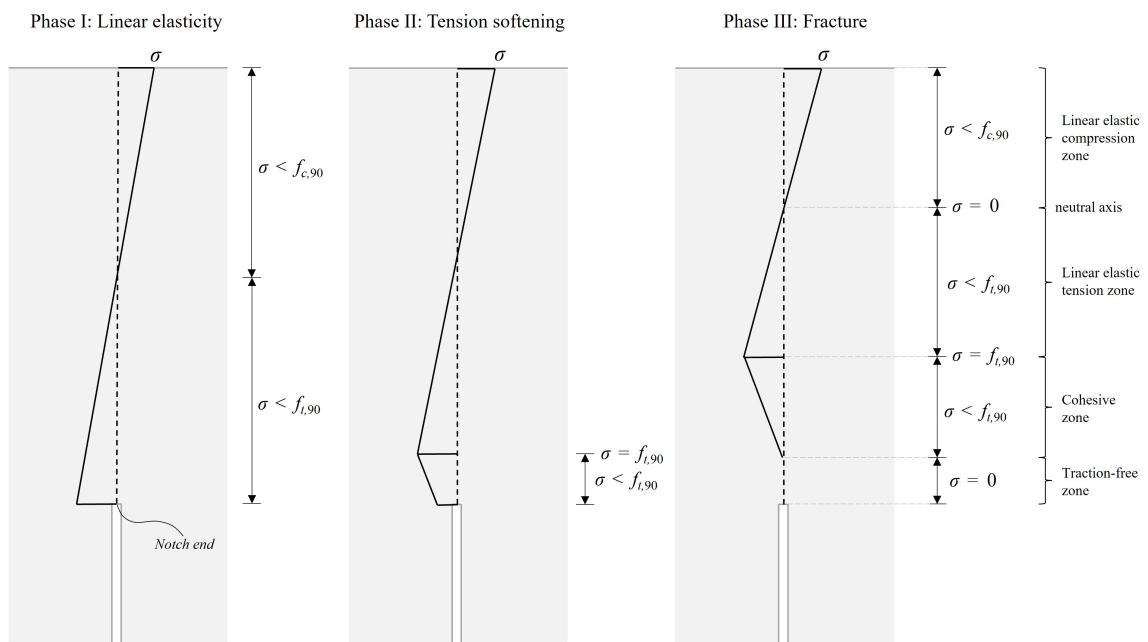


Figure 2.13: Schematic representation of the horizontal stress distribution over the height at mid-span during loading.

A measure for the length of the cohesive zone, or fracture process zone, can be given by the the characteristic length (Boström, 1992). The characteristic length l_{ch} is not the exact length of the cohesive zone, but instead it is derived from three material properties which influence the size of the cohesive zone. The equation for the characteristic length is shown in Eq. 2.8. The equation is retrieved from Bostrom (1992).

$$l_{ch} = \frac{G_f E}{f_t^2} \quad (\text{mm}) \quad (2.8)$$

Fracture energy

The fictitious crack model is characterized by the shape of the tension softening curve and the fracture energy, the area under the stress-crack opening curve. According to Hillerborg, the cohesive zone and thus the fracture energy is a material property. The fracture energy is defined as the energy required to form a unit area of traction-free crack and can thus be measured by determining the total work under the load-displacement graph and dividing it by the total cracked area (Danielsson, 2013; Hillerborg, 1978; Larsen, 1990):

$$G_f = \frac{W_{ext}}{A_c} = \frac{1}{A_c} \left(\int_0^{u_f} P(\delta) du \right) \quad (\text{N/mm}) \quad (2.9)$$

Where W_{ext} is the total external work, A_c the area of the cracked surface and u_f the vertical displacement upon failure. Multiple studies conclude that due to the quasi-brittle nature of wood, the approach of the fictitious crack model and the fracture energy is an excellent method to describe the fracture of wood (Aicher, 2009; Boström, 1992; Hillerborg, 1991; Stanzl-Tschegg et al., 1995). In this research the fracture energy is determined for several hardwood species. Prior studies were performed on the fracture energy of wood, mostly on softwood.

Table 2.3: Values for the fracture energy perpendicular to the grain found in literature.

Wood specie	$G_{f,I}$ (N/mm)	Reference	Notes
Spruce	0.291	(Larsen, 1990)	
	0.346	(Larsen, 1990)	
	0.286	(Larsen, 1990)	
	0.240 - 0.290	(Aicher, 2009)	Beam height: 10 - 320 mm
	0.337 (<i>R</i>)	(Reiterer et al., 2002)	Test setup: CT-specimen
	0.213 (<i>T</i>)	(Reiterer et al., 2002)	Test setup: CT-specimen
	0.210	(Reiterer & Tschegg, 2002)	Test setup: Wedge splitting
	0.500	(Sandhaas et al., 2020)	
Oak	0.280	(Schmidt & Kaliske, 2009)	
	0.348 (<i>R</i>)	(Reiterer et al., 2002)	Test setup: CT-specimen
	0.271 (<i>T</i>)	(Reiterer et al., 2002)	Test setup: CT-specimen
Bilinga	0.728	(Boerenveen, 2019)	
Azobé	0.979	(Boerenveen, 2019)	
	1.340 (<i>T</i>)	(Gijzenberg, 2022)	
	0.710	(Sandhaas et al., 2020)	

Tab. 2.3 constains the fracture energy values found in literature. In the table the (*T*) refers to the fracture energy in the tangential direction and the (*R*) to the fracture energy in the radial direction. Not every test setup is the same, the test setup and geometry conditions can differ, but also the environmental conditions in the lab and loading configuration can cause different results. The purpose of Tab. 2.3 is to give an overview of previous research and to show the order of magnitude for fracture energy values. The study by Reiterer, Sinn

and Stanzl-Tschegg (2002) is also focused on the orientation of the sample. He concluded that the fracture energy in the radial direction is higher than in the tangential direction due to the anatomical features. The orientation of the rays is here an important factor. The presence of rays in hardwood is significant compared to softwood and therefore it is important to analyse the influence of the rays on the fracture energy and fracture process. This is investigated in this research by placing the azobé samples in different orientations. Larsen (1990) found in his study on the fracture energy of softwood that there is a linear relation between the density and the fracture energy, see Eq. 2.10 from (Larsen, 1990).

$$G_f = -0.146 + 0.00104\rho \quad (\text{N/mm}) \quad (2.10)$$

However this equation is applicable to wood densities up to 800 kg/m^3 , and its accuracy to higher densities is unknown and not tested in the experiments in the meta-study by Larsen (1990).

Hillerborg (1991) concluded in his research that in the fictitious crack model the tension softening curve is described by the fracture energy and can thus be regarded as a material property. In the study by Aicher (2009) the dependency of the fracture energy on the specimen size is investigated. The increase in beam height resulted in an increase in the fracture energy. The same observation and conclusion is found by Larsen (1990), who concluded that the fracture energy increase by 20% when the height of the sample is doubled from 40 to 80 mm and 80 to 160 mm. Bazant and Planas (2019) generalised the size effect on the fracture energy and concluded that the fracture energy of a quasi-brittle material is size dependent. However, the size effect of the fracture energy on hardwood is still unknown. The hypothesis that the fracture energy of hardwood species is also size dependent is investigated in this research on azobé samples.

include brittleness number

2.3. Numerical models

The anisotropic nature of wood can give rise to different failure modes. It is therefore hard to define an integral robust numerical (fracture) model for wood, which can accurately predict each failure mode. There are thus different approaches to treat fracture and failure of wood. In this section the use of discrete interface/spring elements, smeared cracking models, continuum damage models and lattice spring models are explained.

A common approach to model tensile fracture of a (quasi-)brittle material is with a discrete crack model. A discrete crack model is the preferred approach when modelling a geometrical discontinuity, which is the case for wood where a softening process is caused by the non-linear phenomena of micro-cracking and fiber-bridging (Rots & Blaauwendraad, 1989). At the discontinuity interface or spring elements are placed which are described by a stress-displacement relation, such as the constitutive law in Fig. 2.8. The fictitious crack model can easily be implemented in a discrete interface model. Several studies have adopted the fictitious crack model by Hillerborg (1978) in the numerical model. Schmidt and Kaliske (2009) assume brittle failure in tension perpendicular to the grain and in shear. Using a continuum plasticity approach yields discretisation dependent results, which is undesirable. Hence, Schmidt suggests using cohesive elements, or interface elements. A

discrete cracking material model is introduced where the traction-separation law, i.e. the stress-crack opening law in Fig. 2.8, is defined by the strength and the fracture energy. Anisotropic behaviour is considered by including the strength and fracture energy values for the different fracture modes as shown in Fig. 2.10. Similarly, Vasic, Smith and Landis (2005) implement the fictitious crack model with springs that have a negative spring constant. This spring constant is related to the stress-crack opening curve in Fig. 2.8. Again, the tensile strength and fracture energy are the input parameters of the model. Prior to the tensile strength being reached in the springs, the stiffness is initially very high.

Both references indicate that the use of discrete cracking elements requires that the crack path is known a priori. In two dimensions this will not give rise to an inaccurate model, because crack propagation will almost always occur parallel to the grain. However, in the case of a three dimensional model the strong anisotropy of wood might lead to an inaccurate prediction of the assumed crack path (Vasic et al., 2005).

Opposite to the discrete crack model is the smeared crack model. The smeared crack model is a continuum model where fracture is described by a stress-strain relation (cf. stress-displacement relation for the discrete model). A major advantage of a continuum model like the smeared cracking model, is that there are no restrictions with respect to the location and path of the crack. Recall that in a discrete model the crack path needs to be defined a priori, this is not the case for the smeared cracking model. Modelling the fracture of wood with a smeared crack model is not very common. A similar approach, the concept of continuum damage mechanics (CDM), is more common. Fracture is here modelled as a stiffness reduction in the form of damage variable d_i , where each failure mode has its own damage variable. CDM is a general constitutive approach where compression, shear and tension failure are combined in a single constitutive model (Sandhaas et al., 2020). To model the post-elastic behaviour in tension, a damage evolution law is defined which includes the tensile strength and fracture energy. In addition to the material properties, the damage evolution law contains a damage threshold parameter κ , which is a function of the equivalent strain $\tilde{\epsilon}$ in an element. Similar to a smeared cracking model, CDM suffers from mesh sensitivity. The fracture energy value is thus dependent of the element size. And if the fracture energy is not constant between the elements, the constitutive law is unequal in the elements. Energy will be concentrated in the smallest elements, where the fracture energy is smallest. The problem of mesh sensitivity can be avoided by introducing a specific value for the fracture energy, $g_f = G_f/l_{ch}$, where l_{ch} is the characteristic length (see Section 2.2.2) (Benabou & Sun, 2015; Sandhaas et al., 2020). The element mesh size must then not exceed the characteristic length in order for the model to remain physically relevant. Although the discrete model mentioned earlier does not suffer from mesh sensitivity, the main drawback of the discrete model is its non integral approach to model the mechanical behaviour of wood by the requirement to define the crack planes a priori (Sandhaas et al., 2020). The CDM and smeared cracking model are not restrained by this drawback, the constitutive model is prescribed in every element in the model.

Lastly, a common technique to model the fracture process of brittle material is with the lattice spring model (LSM). In a LSM the material is modelled as an arrangement of beams interconnected with spring/truss elements (Vasic et al., 2005). In this model the beams represent the tracheids or fibers in wood, while the spring elements represents the bonding between the tracheids/fibers. The advantages of using the LSM for wood: (1)

singularity-related issues are avoided due to the discontinuous nature of the model, which is advantageous for (quasi-)brittle materials, and (2) the material heterogeneity of wood can easily be implemented (Pan, Ma, Wang, & Chen, 2018; Vasić, Ceccotti, Smith, & Sandak, 2009). Furthermore, a predefined crack path is not necessary, which is the case for the other discrete models mentioned earlier. The major drawbacks of LSM are: (1) the computational demand is relatively high, making it a time-demanding and costly model to use in practice, and (2) the material properties require a calibration process with experimental data (Vasic et al., 2005). The advantages and drawbacks of LSM make it an excellent model to predict fracture of wood at the microscopic level. Wittel (2005) use the LSM to predict the fracture behaviour in the growth rings, and how the crack develops in early- and latewood. The report concludes that LSM is an excellent model to predict the complicated stress fields around the crack.

MATERIALS AND METHODOLOGY

3.1. Introduction

In this chapter the methodology of the research is explained in detail. This research consists of various methods to determine the fracture characteristics of hardwood. First the scope and limitations of the experiments are presented in Section 3.2. Then the research methods are explained in detail in Section 3.4. In Section 1.5 the research approach is presented briefly and explained how the different research methods are used in determining the fracture characteristics. In this chapter, the methodology and determination of the material properties is explained in more detail.

Multiple references in the literature study (Section 2) indicate that wood is a quasi-brittle material. After reaching the tensile strength in a material point, non-linear phenomena are activated and the constitutive law is described by a tension softening law. This tension softening law is mainly described by the fracture energy G_f (Eq. 2.7). Thus the fracture energy is an important part in characterizing the fracture process of wood. The higher the fracture energy, the more energy is required to form the crack. In Tab. 2.3 some researchers also focused on the orientation and the size of the sample, and saw different values for the fracture energy. In this experiment the dependency of the orientation and size is tested for azobé.

To understand how the material properties relate to other characteristics of wood, multiple wood species are tested, namely: spruce, oak, bilinga and azobé. Except for spruce, all wood species are hardwood. Spruce is tested to compare the experimental results with literature. Azobé is also tested in different orientations to evaluate the dependency of the fracture behaviour on the orientation in which the specimen is placed. Furthermore, azobé specimens are tested where the dimensions of the sample are increased to evaluate the dependency of the fracture properties on the sample size. The three main fracture properties determined in this research are the fracture energy, the tensile strength and the modulus of elasticity. The former can directly be determined with the experimental analysis, the latter two require a linear elastic numerical model to estimate their value.

3.2. Scope and limitations of the experiments

In Sections 1.3 and 2.1.3 is stated that the fracture model of a quasi-brittle material is described by three parameters, the fracture energy G_f , the tensile strength f_t and the MoE E .

In this experiment a three-point bending test is performed, meaning no accurate values can be determined for the tensile strength and the MoE (in tension), as they have to be measured in a uni-axial tension test or four-point bending test according to EN 408 (European Standard, 2003). The methodology to estimate the tensile strength and MoE is explained in Section 3.4.6.

The properties of wood are prescribed by the Eurocode, in EN 338 (European Standard, 2016). Most of these values are however based on either relations to other strength classes or on their relation to other properties within the strength class. Thus for accurate definitions, these properties need to be measured in this research. As mentioned before, some properties require different test setups, which are out of the scope of this research. Apart from the fracture energy, the density and anatomical structure will be accurately determined. The other properties are obtained from literature or assumed from the numerical model.

The scope of this research is only limited to clear wood. Before testing the samples are checked on any large pre-existing (drying) cracks or irregularities. After testing the fracture plane will also be investigated on any imperfections such as knots or cracks. If the sample contains an imperfection, this will be noted and the sample might be excluded from the results. Shear is also neglected in this experiment, With a slenderness ratio of 0.17 ($h/l = 80/480$) at mid-span, the beam is slender enough to neglect the contribution of shear to the displacement and rotation (Blaauwendraad, 2006).

A secondary goal of this experiment is to explore the dependency of the fracture energy on the orientation of the samples. This is done by studying samples with an orientation of the growth rings under 0, 45 and 90 degrees to the normal of the fracture plane. This is further elaborated in the methodology (Section 3.4), but it is important to note that due to curvature in the tree during its development, the growth rings might not be perfectly orientated at 0, 45 or 90 degrees. It is expected that minor deviations from this orientation will lead to negligible differences in the fracture behaviour. If the angle of the growth rings deviates significantly from the prescribed angle, this will be noted and the sample might be excluded from the results.

3.3. Materials

Test specimen

In Fig. 3.1 the geometry of the representative test specimen is shown. The test specimen is a joint beam with two spruce end parts and a middle part which is orientated such that the direction of the fibers is perpendicular to the beam's axis. The parts of the specimen are glued together with an epoxy adhesive (Griffon houtlijm VB20). The geometry of the test specimen is copied from the setup by Nordtest (1993). The dimensions are related to a parameter a , which is the height of the specimen. The length of the two spruce parts is $3a$ and the length of the middle part is a . The parameter a in this experiment is equal to 80 mm. The total span and width of the beams are kept constant at 240 mm and 40 mm respectively. The length of the notch is equal to 48 mm and a thickness of 3 mm. All dimensions are shown in Fig. 3.1. By inserting the notch in the beam the crack propagation

path is known a priori. Large stresses will concentrate at the notch tip which ensures that cracking will only occur at the notch tip. A modification to the specimen geometry in Fig. 3.1 is made for the azobé series. Due to the smaller dimensions of the beam from which the azobé samples are cut, the length of the middle part the azobé samples is only 70 mm instead of 80 mm, all other dimensions are the same. According to Larsen (1990), this has negligible influence on the value for the fracture energy. In Annex A1 of the report by Larsen the length of the middle part is adjusted from 80 mm to 20 mm, which leads to a change in fracture energy of 5%. The fracture energy only changes 1.5% if the length is decreased from 80 mm to 70 mm, assuming a linear relation between the length of the middle part and the fracture energy.

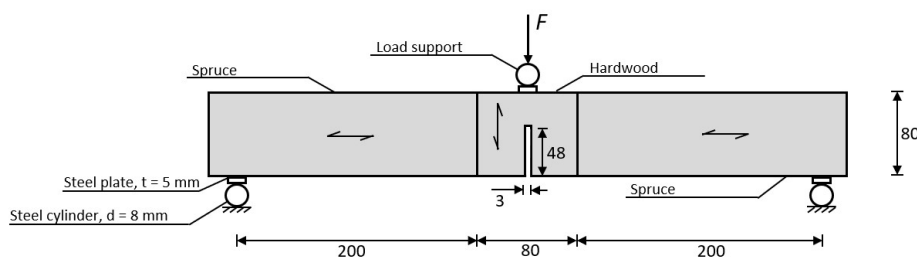


Figure 3.1: Geometry of the test specimen.

In this study four wood species are tested, one softwood and three hardwoods. Spruce (botanical name: *Picea Abies*), English oak (*Quercus robur*), bilinga (*Nauclea diderrichii*) and azobé (*Lophira alata*) are tested in the unnotched three-point-bending (UN-TPB) and single-end notched three-point-bending (SEN-TPB) test. The samples are stored in a climate chamber where the temperature is kept constant at 20°C and the relative humidity at approximately 64%. No direct measurements are taken of the moisture content of the samples. Based on the test conditions the moisture content of the samples is approximated between 10 and 15%. The density values described in the Eurocode (2016) are based on the designation of a wood specie to a certain strength class and are thus not accurate. The exact density of the samples is measured in this research and stated in Section 5.1. The methodology to determine the density is explained in Section 3.4.5.

In the experiment different wood species, orientations and dimensions of the specimens are tested to evaluate the influence of the structure, orientation and size on the fracture behaviour. The test specimens are subdivided in series, shown in Tab. 3.1. Each series has a series code which is a description of the specimens details. The series code is constructed as *AA_BB_CC*, where *AA* is the abbreviation of the wood specie: SP = spruce, OA = oak, BI = bilinga and AZ = azobé. *BB* stands for the angle (in degrees) of the growth rings with respect to the normal of the crack plane, for example: the specimens where the growth rings are orientated parallel to the crack plane (the RL-orientation, Fig. 2.11), are denoted with 90. The *CC* in the series code stands for the height of the specimen in millimeters. In Tab. 3.1 the details of the series are shown.

A couple remarks regarding the samples. Due to damage to one of the oak samples prior to testing, only four samples are tested instead of five. Also, the length of the azobé samples is 70 mm instead of 80 mm. This is due to the size of the log from which the azobé

Table 3.1: Series details.

Wood specie	Series code	Orientation	Geometry (l×h×b) (mm)	Initial notch length (mm)	N of samples
Spruce	SP_45_80	45°	80 × 80 × 40	48	5
Oak	OA_45_80	45°	80 × 80 × 40	48	4
Bilinga	BI_45_80	45°	80 × 80 × 40	48	5
Azobé	AZ_45_80	45°	70 × 80 × 40	48	5
	AZ_0_80	0° (TL)	70 × 80 × 40	48	5
	AZ_90_80	90° (RL)	70 × 80 × 40	48	5
	AZ_45_120	45°	70 × 120 × 40	48	5

samples were cut. It was impossible to cut samples with a length of 80 mm. The azobé sample with the growth rings orientated at 0-degrees is often called the TL-orientation, and in 90-degrees the RL-orientation, see Fig. 2.11.

3.4. Research methods

In the introduction, Section 1.5, an overview of the research approach is given, where the different processes are briefly explained. In this section a detailed methodology of the methods and equipment used are explained. How the methods and processes are connected is shown in Fig. 1.3.

3.4.1. Unnotched three-point bending test (UN-TPB)

A three-point bending test is performed on two different specimens, one with a notch at mid-span and one without. The unnotched specimen three-point bending test (UN-TPB) is used in the back-analysis to estimate the MoE and the tensile strength. During the UN-TPB test the specimen is only loaded in the linear elastic regime. An unnotched test specimen is used because the stress and strain distribution is known in the linear elastic state. The approximation of the stress in the specimen is then used in the back-analysis to determine the MoE and tensile strength, further explained in Section 3.4.6. The UN-TPB test is performed prior to the second test, the single edge notch three-point bending test (SEN-TPB), to calibrate and evaluate the test setup and testing equipment. The details of the materials and the testing equipment is similar to the SEN-TPB test and explained in Section 3.4.2.

3.4.2. Single edge notch three-point bending test (SEN-TPB)

In contrast to the UN-TPB test, which is only used for the back-analysis (the quantitative study), the single edge notch three-point bending test (SEN-TPB) is used in both the qualitative and the quantitative study. There are several test setups suitable for evaluating the

fracture behaviour of a material. The test setup used in this experiment is notched joint beam element loaded by a single force at mid-span and support at the two ends (Fig. 3.1). The test setup is stated by Nordtest (1993) and based on ISO standard 3130 (currently: ISO 13061-10). The SEN-TPB is chosen because it yields stable crack propagation. In a bending test the internally stored energy is minimized compared to a CT specimen or uni-axial tensile test (Boström, 1992; Larsen, 1990). Furthermore, only one crack will form at the notch end and the material properties can directly be determined from the results of the test.

Testing equipment

The major components of the three-point bending test are shown in Fig. 3.2. The test machine consists of two load cells, however the displacement will only be applied from the bottom load cell, the position of the upper load cell is thus fixed. The upper load cell is directly fixed to a roll support which is the connection with the test specimen. Note here that this roll support is referred to as the "load roll support", which is misleading because the displacement is applied from the bottom load cell.

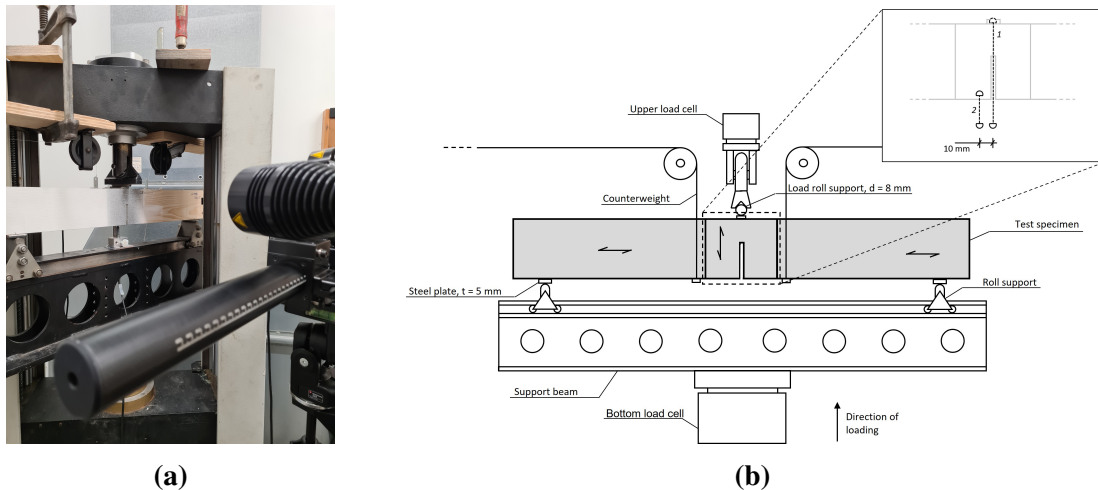


Figure 3.2: (a) Photo and (b) schematic representation of the test setup.

For sake of consistency in appellation in analytical, numerical and experimental models, the support attached to the upper load cell will be referred to as the load support as if the load was applied here. The bottom load cell is not directly connected to the supports, between the supports and the load cell a support beam is placed. The function of the support beam is to provide enough stiffness to prevent any relative displacements between the supports and the bottom load cell. The function of the support beam is also as a reference and attachment point for the LVDTs. The support beam is connected to the roll supports which can be moved to adjust the span of the beam. The supports are placed to have a consistent span of 480 mm. The supports are connected to the test specimen with a steel plate of which the dimensions are $30 \times 50 \times 5$ mm for the two roll supports and $16 \times 50 \times 5$ mm for the load support. The steel plates are positioned as such that the long side is in the out-of-plane dimension in Fig. 3.2b. The final component of the test setup is the counterweight.

The function of the counterweight is to provide an accurate measurement of the fracture energy. The counterweight is attached at the bonding line between the softwood and the hardwood part. The counterweight is applied to counter the self-weight of the beam which influences the determination of the fracture energy. By excluding the potential energy from the deformation due to self-weight, the total external work is only done by the load applied by the load cell.

Measuring equipment

The measurement equipment of the test setup are the load cells, LVDT sensors and the DIC cameras. In addition to these devices, a weight scale is used to measure the counterweights and the weight of the samples, a (digital) caliper to measure the dimensions of the samples, and a camera for images of the samples and to capture any inconsistencies prior to testing.

First, the load cells apply the displacement at the supports. Only the bottom load cell moves, however the force is measured at both load cells. Both load cells might give a slight difference in the reaction force due to different levels of accuracy. The values of the bottom load cell are taken as the reaction force. The bottom load cell also measures the deflection, however from a trial test was concluded that the results for the deflection are inaccurate because of the low relatively low deflection values for the load cell. Therefore LVDTs are placed on the surface of the specimen to measure the deflection. The LVDT is placed on the support beam and connected to the steel plate connecting the specimen with the load support, this LVDT is named sensor 1 in Fig. 3.2b and measures the mid-span deflection with respect to the support beam. The reason behind the placement of sensor 1 on the support beam is because the presence of the notch and the crack path is assumed to be in line with the notch orientation. The sensor measures now the exact displacement where the load is applied, which is required for an exact measurement of the external work. The steel load plate is extended (out-of-plane in Fig. 3.2b) over the specimen so that the LVDT is not in contact with the test specimen. A second LVDT sensor, sensor 2, is used to measure the deflection just next to the notch. Due to fracture the spruce parts will experience a rigid body rotation, which can be determined by the difference in displacement of sensors 1 and 2. This sensor serves as a backup to the DIC. The sensor is also placed on the support beam and attached to a small L-shaped steel plate connected to the specimen. The steel plate is placed on the specimen but will have negligible influence on the results, the dimensions of the plate are very small.

The third element of the measurement equipment are the digital image correlation (DIC) cameras. The purpose of the DIC is to determine the dimensions of the crack and the strains around the crack. DIC works with a scatter pattern on the samples. Digital image correlation is an optical technique to measure to strains and displacement of the sample. The DIC consists of two cameras shown in Fig. 3.2a, which after calibrating, can capture an accurate 3D image of the samples. The displacements and strains in the DIC image are measured using sub-pixel interpolation. The DIC image is split up into small pixels containing a certain pattern, in this case black dots surrounded by a uniform white background. Due to deformation the pattern of black dots distorts and the grey level value of the pixel changes. Using interpolation the displacements and strain within the pixel can be determined. The rate at which the pictures of the samples are taken vary between 1/10 and 1/20

Hz. Different capture rates are chosen because the duration of the fracture process differs per sample and the maximum amount of pictures per sample is limited. The capture rate has no influence on the results.

The reliability and accuracy of the DIC is evaluated before the bending tests are performed. The accuracy is evaluated in a comparison with a strain gauge and a LVDT. An overview of the reliability and accuracy study of the DIC is shown in Appendix A.

Test and measurement procedure

To start off the test, a new DIC and LVDT excel file is created. In the excel file the applied displacement along with the applied force from the load cell are stored. The displacement data from the LVDTs are also stored in this excel file. The DIC file contains the correlation images captured by the cameras. To pair the data from the load cell to the frames of the DIC, the output from the load cell is also connected to the computer containing the DIC software. During the test the force/displacement curve needs to be accurately computed to calculate the external work. To achieve this the displacement is applied in very small steps. According to the test setup defined by Nordtest (1993), the peak load must be achieved at a constant rate in three minutes, which in the tests by Gustafsson (1988) and Boerenveen (2019) is approximately 0.4 mm/min (0.007 mm/s). However Boerenveen also mentions this displacement rate frequently leads to an unstable post-peak behaviour and concludes this value for the displacement rate is too high. He proposes the rate needs to be decreased to 0.05 mm/min (≈ 0.001 mm/s). Vasic, Ceccotti, Smith and Sandak (2009) also recommend a displacement rate of 0.05 mm/min. They state it is required to keep a very low displacement rate to achieve stable tension softening during the loading process. If the loading rate is too high, the increase in strain energy is too high for the non-linear processes (fiber-bridging and micro-cracking) to fully develop. Hence, brittle failure is observed when the strain energy in the sample is too high. Keeping this low displacement rate is however very ineffective as this rate is also applied in the linear elastic state and at the end of the softening branch, where a slow rate is not necessary. Therefore an adaptive displacement rate is applied to the samples where during the peak load and start of the softening curve a slower rate is applied than during the elastic state and the end of the softening curve. The approximate applied displacement rate is shown in Tab. 3.2. Note that these are approximate values of the average vertical displacement. Between the samples the range where the displacement rate is applied can vary.

During the test the specimen and the load-displacement curve is carefully monitored to ensure that when the gradient of the load-displacement curve is changing, the displacement rate is decreased to prevent unstable behaviour and sudden drops in stiffness. The test is done if the specimen has reached complete failure, meaning the load-displacement curve has reached an horizontal asymptote around zero reaction force. The load-displacement curve might not reach exactly zero due to irregularities, rigid body movement of the specimen or an inaccuracy in the weight of the counterweight. When the force has reached zero, the load is released and the measurements are stopped. If the horizontal asymptote does not reach zero, the residual force is taken into account in the calculation of the material properties. This is done by subtracting the work due to the residual force. After the test is finished, the output files are stored externally. The output data is collected and evaluated

Table 3.2: Displacement rate during the loading process, where the range is given of the vertical displacement.

Series	Displacement rate (mm/s)					
	0.002	0.001	0.002	0.005	0.01	0.02
SP_45_80	0 - 1	1 - 2	2 - 2.5	2.5 - 3	3 - 4	4 - 6
OA_45_80	0 - 1.5	1.5 - 3	3 - 3.5	3.5 - 4	4 - 4.5	4.5 - 7
BI_45_80	0 - 1	1 - 2.5	2.5 - 4	4 - 5	5 - 7	7 - 10
AZ_45_80	0 - 1.5	1.5 - 2.5	N/A	2.5 - 3	3 - 4.5	4.5 - 8
AZ_0_80	0 - 1	1 - 2.5	2.5 - 3.5	3.5 - 4	4 - 5	5 - 8
AZ_90_80	0 - 1	1 - 2	2 - 2.5	2.5 - 3	3 - 4	4 - 6
AZ_45_120	0 - 1	1 - 2	2 - 3	3 - 3.5	3.5 - 4.5	4.5 - 9

to determine the parameters required to characterize the fracture behaviour of the wood species.

To calculate the fracture energy, determined through Eq. 2.9, the work done by the external force needs to be computed from the load-displacement curve. The total work is determined by applying the trapezoidal rule in python where the load-displacement curve is integrated over one hundred steps ($\Delta\delta_k \approx 0.1$ mm). Important here is to evaluate the deflection at the point where the load is applied, which is in this case at the top of the hardwood part, just below the steel plate connecting the specimen to the top load cell. The deflection is measured using an LVDT, the position of which is shown in Fig. 3.2b. The LVDTs are the primary measurement source for the displacement. The DIC is only used to determine the strains and crack length. A data point on the load-displacement curve is measured every second, transferred from the LVDT to the computer where it is connected to the corresponding reaction force from the load cell. The load-displacement curve is thus extracted from two measurement devices, the LVDT and the load cell. The other important parameter involved in the fracture energy is the area of the cracked surface. This is measured with a profilometer and explained in Section 3.4.3.

Note that it is assumed that only mode-I fracture occurs, and all the external applied energy is transferred into solely opening fracture. To check whether mode-II and mode-III fracture (Fig. 2.10) are significant, the relative displacement in the y-direction (orthogonal to the beams axis) and the z-direction (out-of-plane in Fig. 3.1) is computed on opposite sides of the crack. The total displacement in the z-direction is also computed to check whether there is a rigid body movement out-of-plane which, if significantly large, could influence the results.

3.4.3. Area measurement

In addition to the three-point bending tests, there are more analysis performed to determine the fracture characteristics of hardwood. Firstly, the determination of the fracture energy requires an exact value of the cracked surface area, see Eq. 2.9. The total cracked surface area of the samples is measured using an optical profilometer (Keyence VR-6000, Fig.

3.3). Due to the organic nature of the material, the crack plane will most likely have some curvature and will not be a flat surface. Therefore, to determine the exact value of the fracture energy (Eq. 2.9) the exact area of the crack plane has to be determined, and a simple calculation of a_c times b might lead to inaccurate results. A profilometer is a combination of multiple lenses which capture the texture and topography of a surface or volume. The 3D surface is mapped using shadows and color contrasts. On the monitor in Fig. 3.3 it can be seen how the straight lines are distorted due to the curvature of the sample. In practice this device is often used to determine volume loss or the corrosion of a surface. In this research the device will only be used to measure the exact surface of the crack plane and the roughness of the surface.

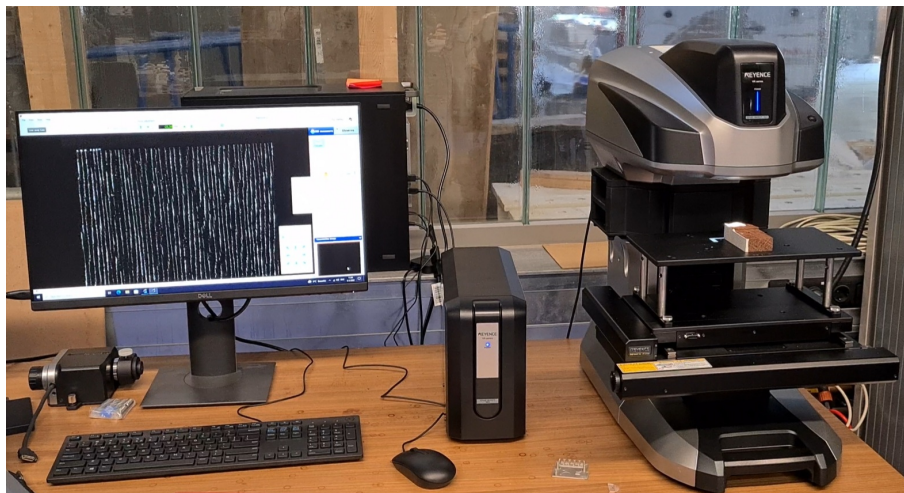


Figure 3.3: The Keyence VR-6000 optical profilometer.

In preparation for the area measurements, the samples need to be modified to fit on the profilometer. The hardwood part of the sample is cut parallel to the fracture plane to a specimen of approximately 50 mm thick. The sample is then placed under the profilometer with the crack plane facing upwards under the lenses, as seen in Fig. 3.3. The device then creates a 3D image of the sample. From this image the cracked surface area and roughness of the crack plane can be extracted. This procedure is done for every sample.

3.4.4. Microscopic analysis

The purpose of the microscopic analysis is to investigate the cell structure of the hardwood species and the crack propagation path through the sample. The microscopic analysis is performed following the fracture tests. From microscopic images it is difficult to exactly determine the composition of the wood specie. The exact amount of cell types is also retrieved from literature. In the Holtzatlas by Wagenfuhr and Scheiber (2006) a range is given for the amount of cell types in each wood specie (Tab. 2.1). These values are average values and can vary significantly per tree and even throughout the tree. Therefore in addition to what is stated in the Holtzatlas, the samples are also analysed with a microscope. To prepare the samples for the microscope is a very time consuming process, and therefore

only one sample is analysed per series. It is assumed that the cell composition is constant throughout the tree.

Before the samples can be analysed they need to be prepared to obtain the best results. This requires paraffin sectioning each sample. This is done using a HistoCore Multicut R microtome, which is a device able of cutting the samples to extremely thin dimensions. This procedure can be seen in Fig. 3.4a, where an azobé sample is trimmed to a width of 20 μm thick. To obtain the best results with the microtome, the samples need to be properly hydrated. This is done by soaking the samples in water three days in advance. After the tissues are cut, they are first shortly soaked in distilled water and then stored between two glass panels in 70% ethanol to dehydrate the tissue. The tissues are then analysed with a microscope, the Keyence VHX 6000 shown in Fig. 3.4b. The wood samples as seen in Fig. 3.4a are trimmed in different orientations. This is done to properly define the composition of each wood specie. For example, to define the quantity of the parenchyma and the rays, the samples needs to be analysed in the cross-section and the tangential plane. A cross-section of the samples also reveals how the sample has fractured. This is especially important in the comparison between the TL- and the RL-orientation. The orientation of the growth rings are different and thus the crack propagation might be different.

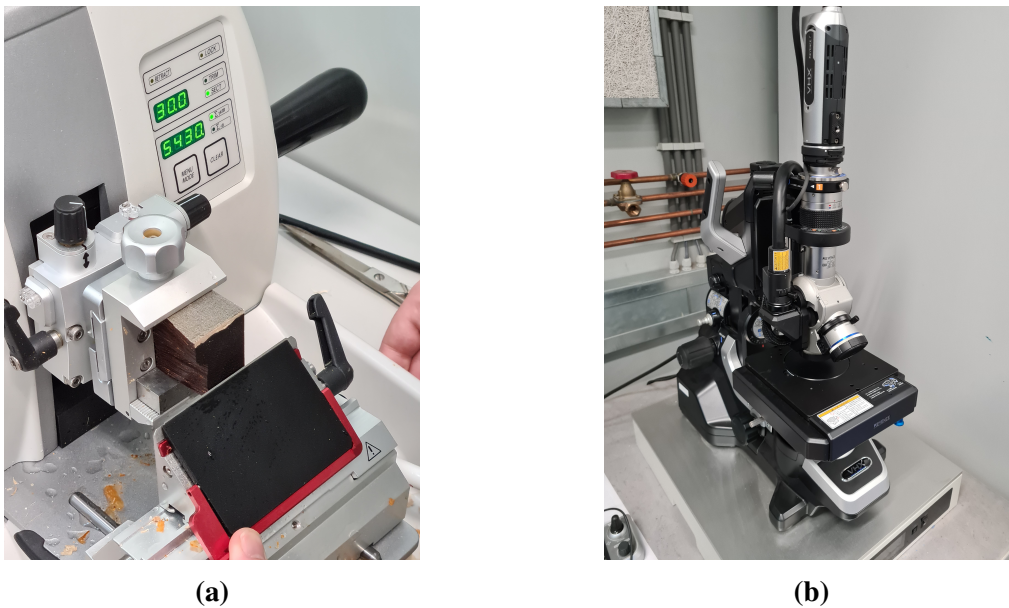


Figure 3.4: (a) The HistoCore Multicut R microtome to prepare the samples and (b) the Keyence VHX 6000 microscope to produce the microscopic images.

3.4.5. Density measurement

The density of the samples is measured by weighing a small sample of the specimens. A sample is manually sawn of approximately $40 \times 30 \times 20 \text{ mm}^3$. The dimensions of the sample are then precisely measured with a caliper to determine the exact volume. The weighing is done in the same conditions and environment as for the values prescribed by the Eurocode,

which is at a temperature of 20 °C and a relative humidity of 65%. This results in a moisture content between approximately 10 and 15%.

3.4.6. Back-analysis

The final method in this research is the back-analysis. The back-analysis is a method used to estimate the properties which can not directly be determined from the fracture tests. A back-analysis is an iterative process where material properties are estimated based on a comparison between experimental and numerical results. Both the MoE and tensile strength are estimated using a back-analysis. The process to determine the values is however slightly different. In the sections below, the process is described to estimate both material properties. A detailed report of the numerical model which is used in the back-analysis is written in Section 6.

Modulus of elasticity

The modulus of elasticity (MoE) is determined using a back-analysis with the linear elastic numerical model of the unnotched test specimen, the UN-TPB test. The UN-TPB test specimen is chosen because the stress and strain distribution are known during the linear elastic stage. It should be noted that this statement is based on bending test on softwood. If the test setup yields stable results for hardwood is still unknown. From the test an initial estimation of the MoE is obtained. Thereafter, the initial estimation of the MoE is applied in a linear elastic numerical analysis of the notched specimen. The choice to then perform the back-analysis with the notched specimen instead of the unnotched specimen, is to evaluate the relation between the MoE and the orientation of the growth rings. The tests with the unnotched specimens were only performed in a single orientation of the growth rings. The linear elastic behaviour of the numerical model is then compared with the results of the experiment of the notched specimen. The comparison is done by evaluating the stiffness in the linear elastic regime, which is a reasonable indication of the MoE of the wood specie. The contribution of the softwood parts of the specimen (Fig. 3.2) to the stiffness of the member is negligible. If the linear elastic curves do not coincide, the MoE input parameter of the numerical model is updated accordingly. This iterative procedure is repeated until the linear elastic curves coincide and the initial stiffness values are within a range of 5%. The applied MoE of the numerical model is then a realistic estimation. This iterative process is visualized in a flow chart in Fig. 3.5.

Tensile strength

The tensile strength is estimated in a similar manner, using a back-analysis with the numerical model. However, there are some key differences. Firstly, the tensile strength is determined from the stress at the onset of cracking, hence the back-analysis is not performed with a linear elastic numerical model of the specimen but with a non-linear numerical model. Secondly, the iterative procedure of the back-analysis is linked to the comparison of the peak load in both experimental and numerical analysis, because the peak load is mainly determined by the tensile strength in the highest stresses fibers. Thirdly, because a

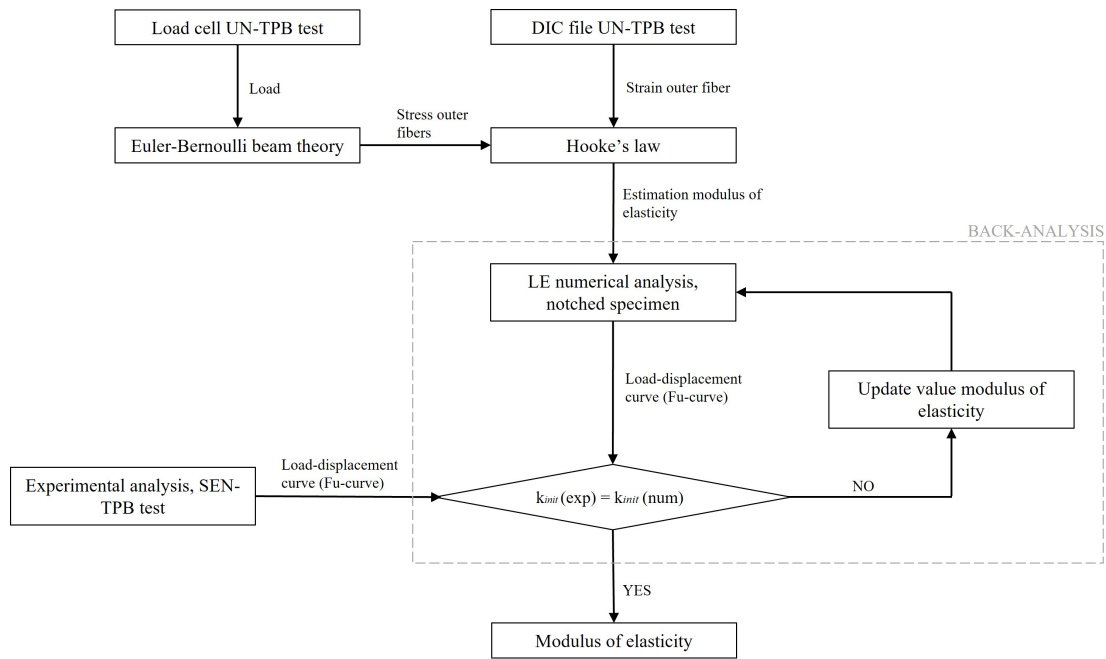


Figure 3.5: Flow chart of the back-analysis to determine the values for the modulus of elasticity.

non-linear analysis is performed, other parameters are involved such as the softening behaviour and the considered crack model. These parameters need to be prescribed as well. In Fig. 3.6 a flow chart is shown of the procedure to determine the tensile strength.

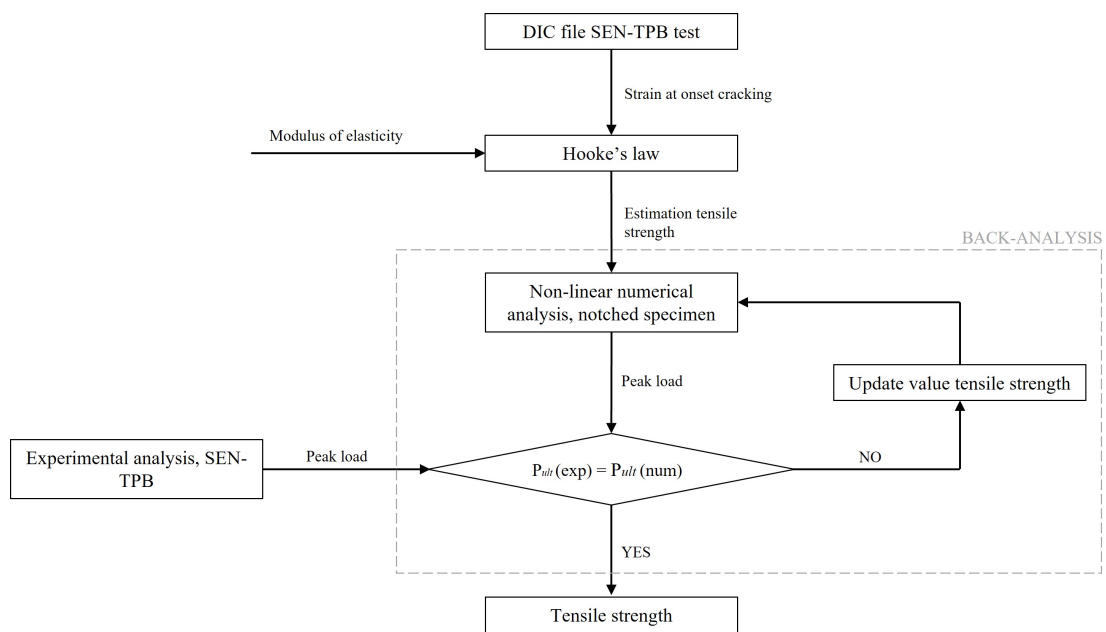


Figure 3.6: Flow chart of the back-analysis to determine the values for the tensile strength.

EXPERIMENTAL OBSERVATIONS

The presentation of the results is separated in two chapters, one where the results of the qualitative study are presented and one chapter where the quantitative results are shown. This distinction is illustrated in the flow chart of this research, Fig. 1.3. In this chapter, Chapter 4, the observations of the experiment are presented. This includes the results of the microscopic analysis, the results from the profilometer and general observations from the fracture test. In Section 5 the quantitative results of the experiments are obtained, i.e. the values for the density, fracture energy, MoE and the tensile strength.

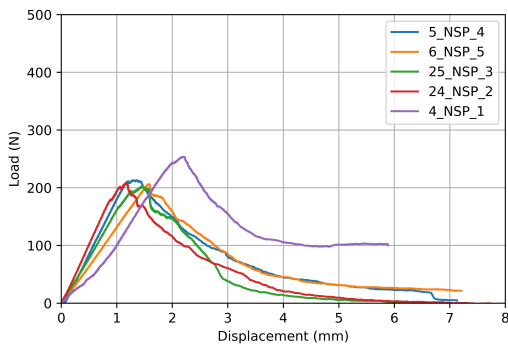
First, the general mechanical behaviour of the fracture tests is presented. Then, the results of the profilometer and the microscopic. The results are then discussed and put in context with findings in literature. Also, the limitations of the experiment are discussed. At last, conclusions of the qualitative study are presented.

4.1. General mechanical behaviour

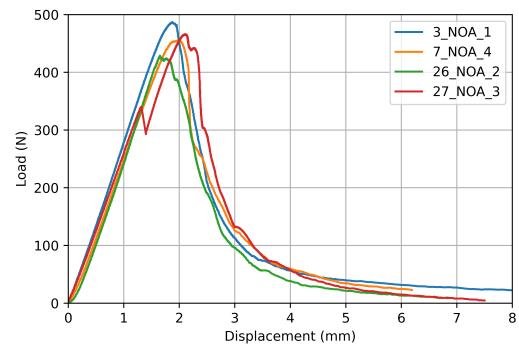
During the tests some irregularities occurred which need to be explained first:

- The first sample of the spruce series (Fig. 4.1a), sample 4_NSP_1, is excluded from the results and determination of all material and fracture properties. This is because a knot was present perpendicular to the crack plane, which led to higher values for the peak load and fracture energy than the other samples. This thesis is limited to clear wood, and therefore this sample is excluded from the analysis.
- On the linear elastic branch of sample 27_NOA_3 (Fig. 4.1b) there is a small drop in load when the load reaches 345N. This can be explained by a shift of the sample in the out-of-plane direction. This is concluded from the DIC images. This can be due to a crack forming at the back of the sample or a irregularity at the contact between the sample with the (load)supports.
- Sample 17_NAZ_11 shows a rapid increase in vertical displacement at the start of the loading process. This can be explained by a misplacement of the load support. Due to a shift of the load support there is a sudden increase in the displacement without any resistance from the beam. The shift in displacement is taken into account in the analysis.

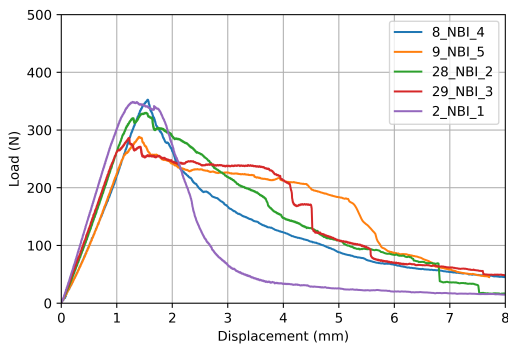
From the load-displacement curves of the wood species indications of the general mechanical behaviour can be seen. As can be seen in Fig. 4.1, the stiffness, peak load and post-peak behaviour can be very contrasting between wood species and even between the orientations. As expected the stiffness and peak load of the softwood spruce is lower than the hardwood species (Fig. 4.1a-d). The elastic properties of spruce, acquired in the literature study (Section 2.1.2), are lower than the hardwood species. Between the TL-orientation (Fig. 4.1e) and the RL-orientation (Fig. 4.1f) a significant contrast is seen between the peak load and the softening behaviour. If the fracture plane is parallel to the growth rings, i.e. the RL-orientation, the peak load is approximately 1.5 times larger than when the growth rings are orientated perpendicular to the fracture plane (TL-orientation). Furthermore, not only is there a difference in the peak load but also in the softening behaviour.



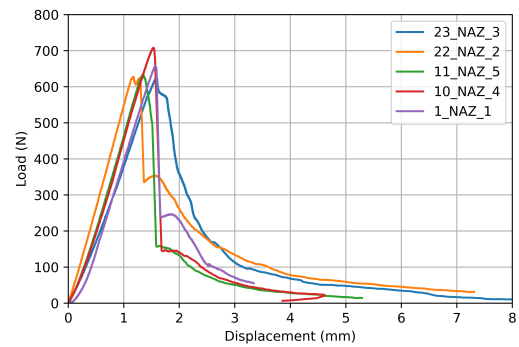
(a) SP_45_80



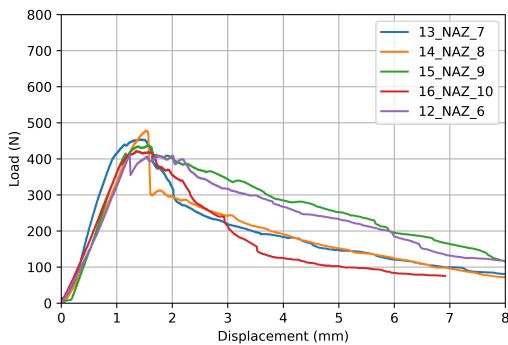
(b) OA_45_80



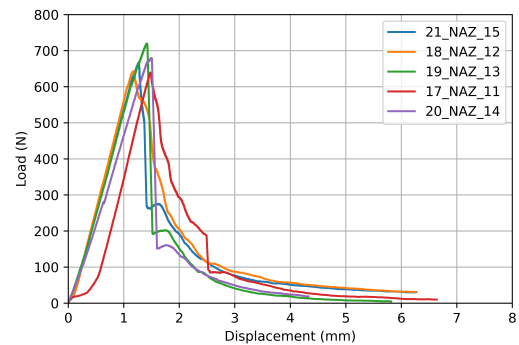
(c) BI_45_80



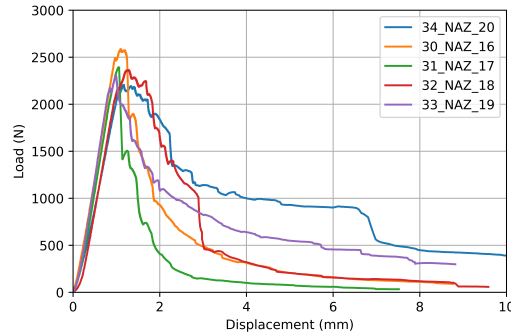
(d) AZ_45_80



(e) AZ_0_80



(f) AZ_90_80



(g) AZ_45_120

Figure 4.1: Load-displacement curve of the experimental results.

In addition to the load-displacement curve, the horizontal stress distribution over the height of the beam is analysed at multiple points along the beam's length. Important here is to show how the stress distribution changes close to the notch.

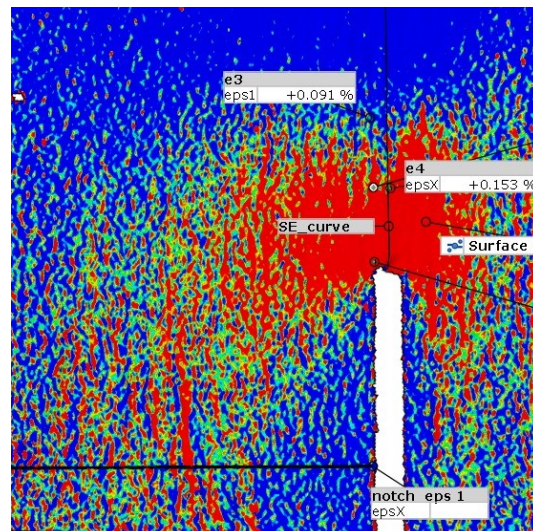
**Figure 4.2:** Contour plot of the highest principal strains for a spruce sample, showing how the stress distribution changes around the notch.

Fig. 4.2 shows how the stresses form around the notch. Analysis of the horizontal strains in the beam show that the horizontal stress distribution over the height is according to the linear-elastic stress distribution of a slender beam. Instead, the stress distribution around to notch can be better represented by the stress distribution of a deep beam, where the neutral axis does not necessarily coincide with half the beam height.

Fig. 4.3 shows that the neutral axis changes over the length of the beam. At mid-span the neutral axis is 18 mm below the top of the beam. According to linear elastic theory, the neutral axis should be 16 mm below the top of the beam. In Fig. 4.3b the neutral axis is 24 mm below the top of the beam and in Fig. 4.3c, 35 mm from mid-span, the stress distribution approaches the expected linear distribution, with the neutral axis at half the

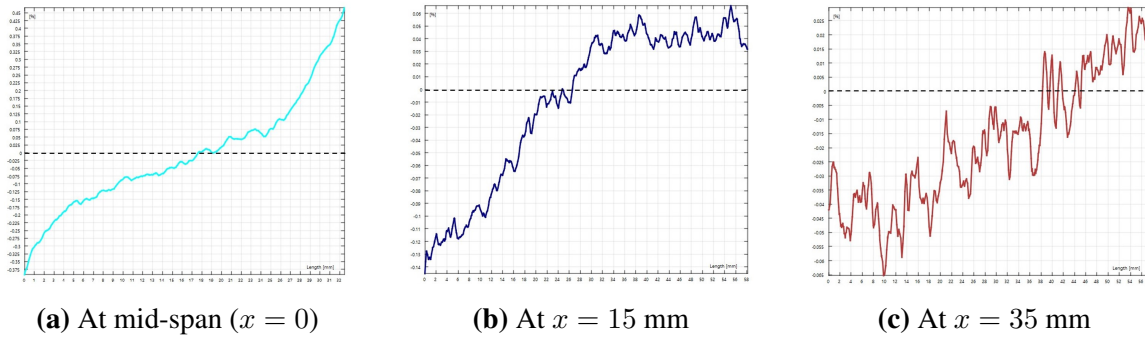


Figure 4.3: Horizontal stress distribution over the height of the beam for spruce (sample: 24_NSP_2). The parameter x is the distance along the length/axis of the beam.

height of the beam. Note that for Fig. 4.3b and 4.3c the stress distribution is not computed over the full height. This is due to the capture frame of the DIC, which is limited to the top part of the beam.

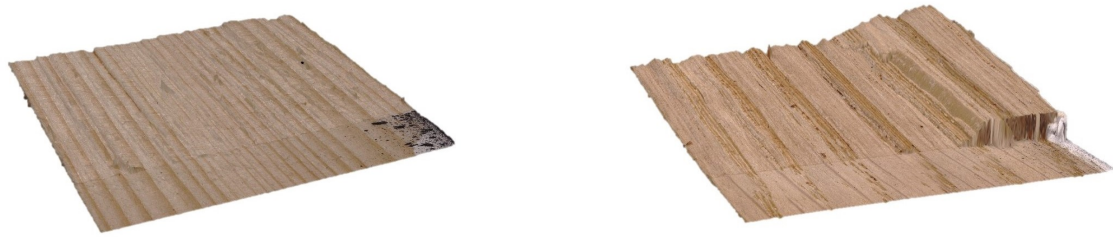
4.2. Crack plane observations

In Fig. 4.4 3D image are shown of the cracked surface. All samples within a series show comparable crack plane roughness, thus only one sample is shown for each series. From the figures contrasting crack plane roughness can be seen. The spruce series (SP_45_80) and the azobé-90° series (AZ_90_80) show a very flat cracked surface, whereas the bilinga series (BI_45_80), the azobé-0° series (AZ_0_80) and the azobé series with an increased size (AZ_45_120) show a more undulating cracked surface. The roughness of the oak (OA_45_80) and azobé-45° series (AZ_45_80) is within the two extremes.

In addition to the 3D images from the profilometer, the samples are also visually inspected from the top of the beam with the naked eye to see how the crack developed over the width of the beam. In Fig. 4.5 a top view is shown of the samples and the crack path along the width of the beam. All samples within a series show comparable crack plane roughness, thus only one sample is shown for each series. Similar to Fig. 4.4, differences are observed in the crack path roughness between the wood species. Contrasting to the relatively flat crack plane of the AZ_45_80 and AZ_90_80 samples, the crack plane of the AZ_0_80 and AZ_45_120 series is more undulating. The same undulating crack path is observed in the bilinga series. The crack path of the spruce and oak series are also relatively flat.

4.3. Microscopic analysis

In this section the results of the microscopic images is presented. Not for every wood species a clear tissue could be obtained due to difficulties with the microtome which was due to the high density and rigid structure of bilinga and azobé. Changing the blades of the microtome did not result in a more clear tissue of the sample. In Fig. 4.6 - 4.9 a selection



(a) SP_45_80

(b) OA_45_80



(c) BI_45_80



(d) AZ_45_80



(e) AZ_0_80



(f) AZ_90_80



(g) AZ_45_120

Figure 4.4: 3D image of the fracture surface captured with the profilometer.



(a) SP_45_80



(b) OA_45_80



(c) BI_45_80



(d) AZ_45_80



(e) AZ_0_80



(f) AZ_90_80



(g) AZ_45_120

Figure 4.5: Top view of the out-of-plane crack propagation path.

is shown of the samples. Due to the 45 degree orientation of the spruce, oak and bilinga samples, it is difficult to have a perfect representation of the tangential or radial plane. Only clear tangential and radial images of azobé could be obtained. However the purpose of the figures is to show the cell structure and how the crack propagates through the wood cells. The difference between softwood and hardwood, explained in Section 2.1.1, is clearly visible in the microscopic images. The simplicity of softwood is clearly visible in the images of spruce, Fig. 4.6. The high volume fraction of the tracheids, and the distinction between earlywood and latewood can be seen in the figures. The anatomy of the hardwood species is much more complex, and distinguishing the different cell types is more difficult. In Fig. 4.7-4.9 the cell types are highlighted. A good example of the variation between hardwood species, is the amount and distribution of vessels. The distribution is characteristic of the environment in which the hardwood grows. Oak is a ring-porous hardwood, meaning the vessels are distributed in rings. This is characteristic for a hardwood growing in temperate climate, similar to early- and latewood in softwood. In Fig. 4.7a these ring distribution of vessels is clearly seen. On the opposite is diffuse-porous hardwood which is hardwood growing in more tropical climates, where there is little distinction in the seasons. This is the case for bilinga and azobe where the vessels are more evenly distributed over the cross-section. The amount of vessels also varies largely per wood specie, the amount of vessels for bilinga (Fig. 4.8a) is much more than for azobé (Fig. 4.9a).

Tab. 2.1 gives an indication of the quantity of each cell type in the wood species. From the microscopic images it can be seen that the parenchyma are (almost) absent in the spruce and oak wood structure, this is consistent with the values in the Holzatlas (Tab. 2.1). Fig. 4.8 shows that the amount of parenchyma cells in bilinga are higher than indicated by the Holzatlas. The amount of rays is much harder to define from the microscopic images. In Fig. 4.8b the rays can be seen in bilinga, but because the growth rings are orientated at a 45-degree angle the rays are not positioned orthogonal and the exact amount of rays is hard to define. In the AZ_90_80 series the rays are positioned orthogonal and thus the rays are easier to observe, see Fig. 4.9c. Moreover, there is also a clear color distinction between the fibers and the rays in azobé.

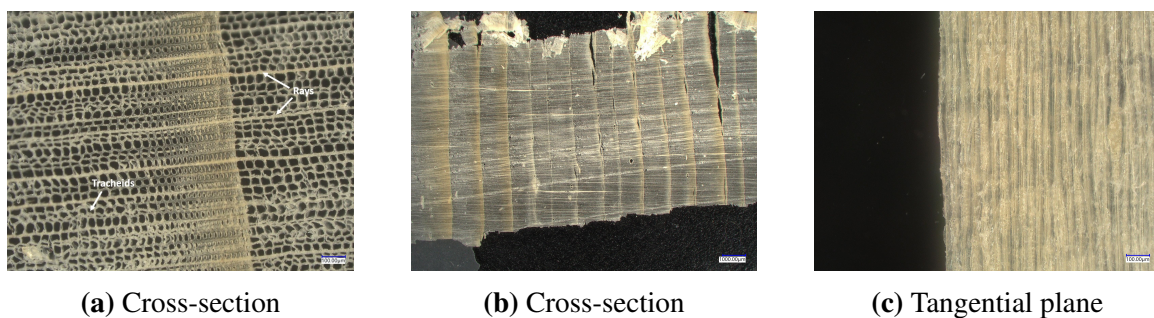


Figure 4.6: Cell structure spruce.

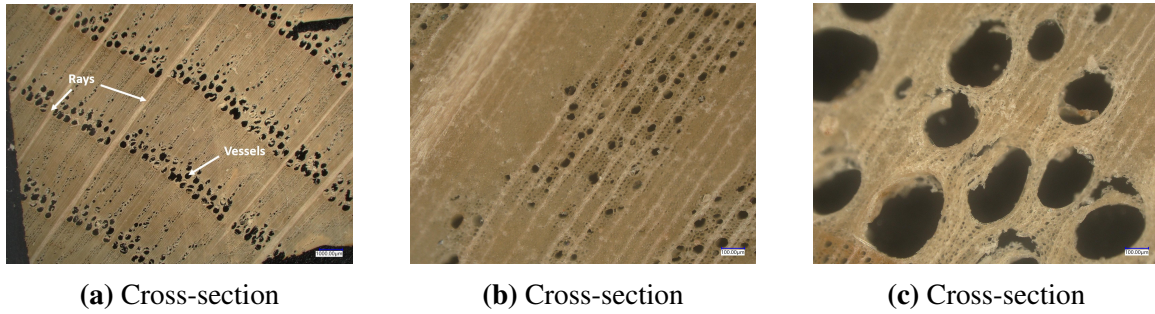


Figure 4.7: Cell structure oak.

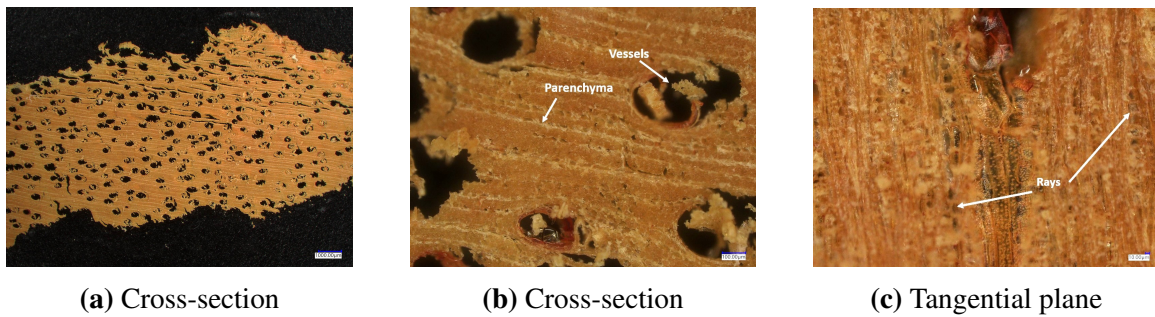


Figure 4.8: Cell structure bilinga.

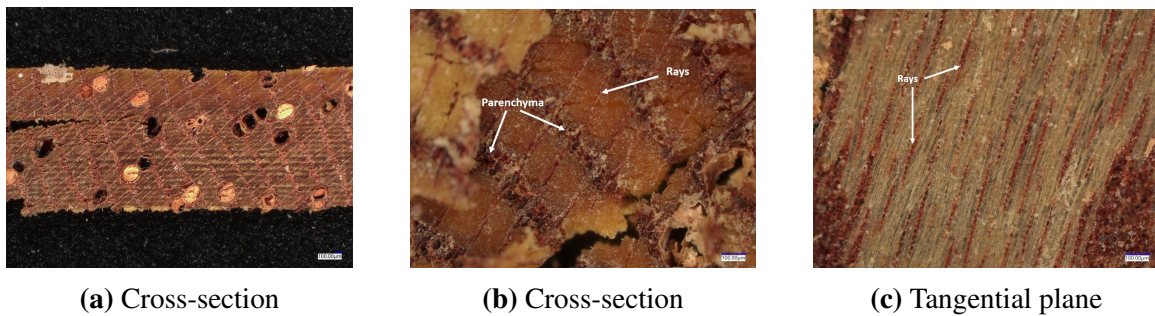


Figure 4.9: Cell structure azobé.

4.4. Discussion

In this section the results and findings of the experiment are discussed and interpreted in relation to the main research question and the secondary research questions regarding the experimental analysis. First, the key findings of the experiment are briefly summarised. Secondly, these key findings are interpreted and correlations and patterns are identified. Next, the results will be placed in the context of the literature study, and the similarities and/or differences are discussed. Lastly, the limitations or weaknesses of this research are presented.

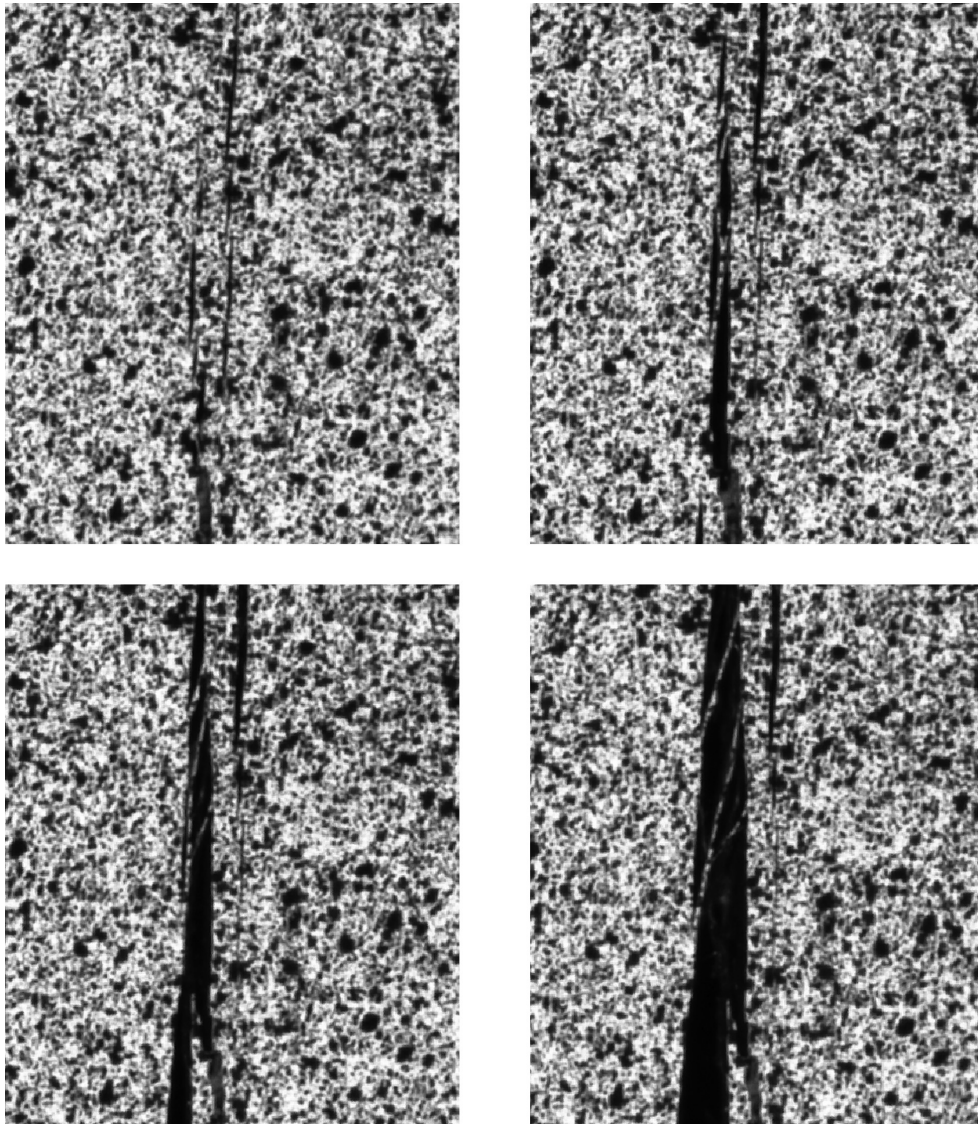


Figure 4.10: Images of the fiber-bridging process in a AZ_0_80 sample (sample: 16_NAZ_10) obtained with the DIC cameras.

4.4.1. Key findings

In this subsection the key findings of the experiment are presented.

- The overall strength of spruce is significantly lower than the three hardwood species.
- The shape of the softening curve of the azobé samples varies with the orientation of the sample.
- The peak load of the AZ_0_80 series is significantly lower than for the other azobé series (excluding the AZ_45_120 series).
- Unstable crack behaviour only occurred in the AZ_45_80 and the AZ_90_80 series.

- The shape of the softening curve in the bilinga series is inconsistent.
- In the azobé samples the crack mainly propagated through the parenchyma cells.
- There is a significant difference in the roughness of the crack plane between the different samples.
- Amount of vessels of azobé is lower than stated in the Holzatlas (Wagenführ & Scheiber, 2006).

4.4.2. Interpretation of the results

From the load-displacement curve (Fig. 4.1) it can be seen that the overall strength, i.e. the peak load and slope of linear elastic regime is much lower for spruce than for the hardwood species. This difference can be explained by the dissimilarities between softwood and hardwood. In Section 2.1.1 it is explained how the anatomy is different between softwood and hardwood. Softwood almost completely consists out of the multi-functional tracheids, whereas for hardwood the strength and transportation of nutrients is subdivided over different cell types, namely the fibers (dead cells) and the vessels. The presence of fibers cause hardwood to be much stronger and stiffer than softwood.

A second key observation from the test, is the difference between the three azobé series with different orientations. For the 45- and 90-orientation (series: AZ_45_80 and AZ_90_80) an average peak load of approximately 650 N is found, whereas for the 0-orientation (series: AZ_0_80) the average peak load is approximately 430 N. Furthermore, the shape of the softening curve and the roughness of the cracking plane is also different. These inconsistencies between the different orientations can be explained by the anatomy of hardwood and the direction in which the cells are orientated. Section 2.1.1 explains that the anatomy of hardwood is described by vessels, parenchyma, rays and fibers. A property of the latter two is that they are much stronger than the other hardwood cell types and than the tracheids in softwood (Blaß & Sandhaas, 2017). Thus if loading is in the direction of the rays, they reinforce the strength of the wooden structural element. In the case of this experiment, i.e. perpendicular to the grain mode-I fracture mode, the rays must be orientated perpendicular to the cracking plane to enhance the strength of the material. This is the case in the AZ_90_80 sample, which is illustrated in Fig. 4.11. In the figure it can be seen that in the AZ_90_80 series, the RL-orientation, the rays are orientated perpendicular to the crack plane. It is assumed here that the curvature in the growth rings is infinite and the rays are perfectly orthogonal to the growth rings. In the AZ_0_80 series the rays are orientated parallel to the crack plane. The higher peak load in the AZ_90_80 samples can be explained by the reinforcing action of the rays. In the AZ_45_80 series the rays are not orientated perpendicular to the crack plane, but under an angle the rays will still carry the load.

The difference in shape of the softening curve and the roughness of the crack plane can be explained by the orientation of the longitudinal parenchyma cells, see Fig. 4.8b and 4.9b. In contrast to the reinforcing action of the rays, the parenchyma cells provide a weakness in wood cross-section. This is due to the thin cells walls of the parenchyma cells. Thus, if loaded perpendicular to the grain, the crack has the tendency to run through the parenchyma

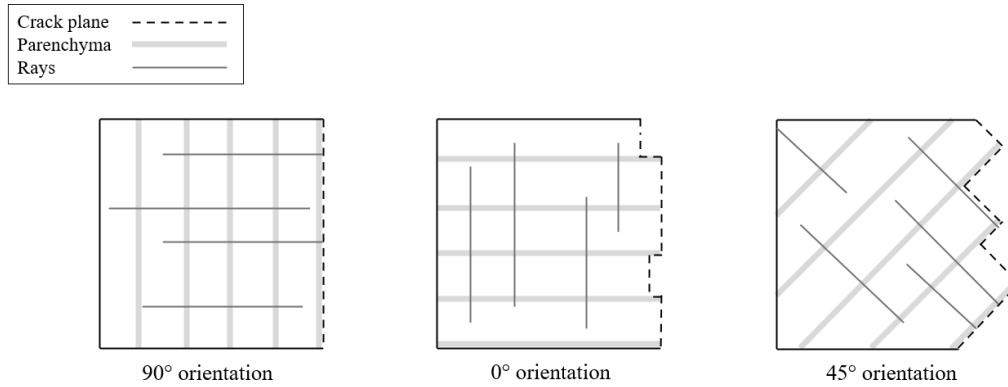


Figure 4.11: Failure modes and cell orientation of the different azobé orientations.

cells. This conclusion is drawn from visual inspection of the azobé samples, Fig. 4.5d-g. At the onset of cracking the crack will propagate through the weaker parenchyma cells, which run parallel to the growth rings and thus parallel to the crack plane in the case of the AZ_90_80 samples. When the parenchyma cells are orientated perpendicular to the crack plane, it is much harder for the crack to propagate through the wood. This results in much less flat fracture surface. The roughness of the fracture plane is thus caused by the orientation of the parenchyma cells, which is seen in Fig. 4.4d-f. The two different failure mechanisms, caused by the orientation of the rays and parenchyma cells, is illustrated in Fig. 4.11.

In the determination of the fracture energy, only stable cracking propagation is considered. Fig. 4.1 shows that unstable cracking occurred on several samples in the AZ_45_80 and the AZ_90_80 series. Although the SEN-TPB test minimizes unstable cracking (Boström, 1992; Larsen, 1990), samples are still prone to unstable cracking if the applied displacement rate is too high, as was found by Boerenveen (2019). The applied displacement rate was reduced to the almost minimum possible with this testing device. The cause of the unstable cracking is thus most likely not due to the test setup or applied displacement rate. Because cracking only occurred for the azobé samples which reached a relatively high peak load, the cause of the unstable crack behaviour is due to the amount of stored strain energy in the sample. Unstable cracking did not occur in the other series. The problem of unstable cracking in this research is thus wood specie and geometry specific. Because unstable cracking only occurred in the AZ_45_80 and the AZ_90_80 series, another explanation could be brittle failure of the rays. As mentioned earlier, in these two series the parenchyma cells act as a weak link through which the crack can easily propagate. If the rays fail in a brittle manner, the sample will fail abruptly under the applied load.

In the load-displacement curve of the bilinga series (BI_45_80) an inconsistent softening curve can be seen. Some samples show a softening curve comparable to the softening curve of the AZ_0_80 series. Due to the orientation of the parenchyma cells perpendicular to the crack plane in the AZ_0_80 series, the stiffness of the sample is higher in the post-peak regime compared to when the parenchyma cells are orientated parallel to the crack plane, as is the case in the AZ_90_80 series and to some extent in the AZ_45_80 series. In bilinga the presence of parenchyma cells is relatively low compared to azobé, Tab. 2.1.

The low volume fraction of parenchyma cells in bilinga thus prevents a weak link in the wood structure comparable to the AZ_0_80 series. The exact cause of the inconsistency of the softening curve of the bilinga samples is unknown. The cause of the inconsistency is probably due to a higher scatter in the composition of the different cell types compared to other hardwood species. Recall that the cell structure of hardwood is complex and that although in this research it is assumed that the composition of cell structure throughout the tree is uniform. In reality wood is not a uniform and homogeneous material. Thus in one part of the tree the amount of parenchyma cells and rays might be higher, leading to other mechanical properties than in other parts of the tree. According to the HoltzAtlas (2006) the composition of the ray cells in bilinga is heterogeneous whereas for oak and azobé the composition is homogeneous.

ESTIMATION OF THE MECHANICAL PROPERTIES

The second part of the experiment is the estimation of the material properties which are relevant in a fracture model. In Chapter 4 key observations of the experiment are discussed. In this chapter a similar discussion is done but based on the numerical results from the experiment. This is done by determining the density, fracture energy, MoE and tensile strength. In Section 2.1.3 and 2.2 the use of these material properties in a constitutive and fracture model is explained.

5.1. Density

In Tab. 5.1 the average values for the density are shown. In this table a distinction is made between the different azobé series, because they are sawn from different logs. The densities are similar to the values stated in the Eurocode, NEN-EN338. Only the average density value for oak in this experiment slightly deviates from the mean value stated in the Eurocode, 746 and 640 kg/m³ in the experiment and Eurocode respectively. No significant variation is seen in the density values within a series.

Table 5.1: Average density of the testes samples at an estimated moisture content of 12%.

Series	Density (kg/m ³)
Spruce	491.28
Oak	746.00
Bilinga	763.25
Azobé 45	1074.99
Azobé TL	1050.46
Azobé RL	1063.37
Azobé 120	1027.85

5.2. Fracture energy

In Tab. 5.2 the results of the fracture energy are shown. The fracture energy values are determined from the work by the external load and the total cracked area according to Eq. 2.9. The external work is obtained from the load-displacement curve and the cracked area with the profilometer (Section 3.4.3). In Tab. 5.2 the total external work and cracked surface area is shown for all samples in the experiment.

The results show that the fracture energy values for the hardwood species are around 0.5 N/mm, this is only true for the samples under 45 degrees and a height of 80 mm. Although literature on the fracture energy of hardwood is very limited, the values found in this experiment are different from the values found in literature, see Tab. 2.3. Only the average value for the fracture energy of spruce is consistent with the literature.

A notable difference can be seen between the fracture energy value for the different growth ring orientations. For azobé under 45- and 90-degrees the fracture energy values are approximately equal, while under 0-degrees the average fracture energy is a ratio 1.89 larger. This ties in with the conclusions made in Chapter 4, where the distinction between the orientations is also noticed. The relation between the observations of the crack plane and the numerical values is further discussed in Section 5.7.

Table 5.2: Total external work, cracked surface area and fracture energy for each sample including the average and standard deviation per series. (*Table continues on next page*)

Series	Sample	W_{ext} (Nmm)	A_c (mm ²)	$G_{I,f}$ (N/mm)	
Spruce	2	408.42	1499.0	0.273	
	<i>SP_45_80</i>	3	387.83	1654.2	0.235
	4	386.06	1544.1	0.250	
	5	372.22	1533.4	0.243	
	<i>Average</i>		<i>388.63</i>	<i>1557.7</i>	0.250
	<i>S.D.</i>		<i>14.92</i>	<i>67.16</i>	<i>0.01</i>
Oak	1	854.79	1529.3	0.559	
	<i>OA_45_80</i>	2	793.08	1547.4	0.513
	3	870.25	1622.1	0.537	
	4	900.97	1605.2	0.561	
	<i>Average</i>		<i>854.77</i>	<i>1576.0</i>	0.542
	<i>S.D.</i>		<i>45.39</i>	<i>44.63</i>	<i>0.02</i>
Bilinga	1	694.38	1653.1	0.420	
	<i>BI_45_80</i>	2	1120.48	1674.6	0.669
	3	854.65	1709.9	0.500	
	4	640.48	1675.3	0.382	
	5	858.34	1794.5	0.478	
	<i>Average</i>		<i>833.67</i>	<i>1701.48</i>	0.490
<i>S.D.</i>		<i>187.10</i>	<i>55.84</i>	<i>0.10</i>	
Azobe	1	791.15	1414.5	0.559	
	<i>AZ_45_80</i>	2	929.51	1581.1	0.588

	3	1132.99	1564.3	0.724
	4	809.65	1463.4	0.553
	5	728.70	1448.6	0.503
	<i>Average</i>	<i>878.40</i>	<i>1494.4</i>	<i>0.586</i>
	<i>S.D.</i>	<i>159.83</i>	<i>73.90</i>	<i>0.07</i>
Azobe	6	2085.87	1627.6	1.282
AZ_0_80	7	1645.31	1578.5	1.042
	8	1574.99	1542.8	1.021
	9	2231.36	1665.7	1.340
	10	1293.27	1498.6	0.863
	<i>Average</i>	<i>1766.16</i>	<i>1582.6</i>	<i>1.110</i>
	<i>S.D.</i>	<i>385.16</i>	<i>66.31</i>	<i>0.18</i>
Azobe	11	772.29	1418.7	0.544
AZ_90_80	12	814.03	1474.9	0.552
	13	780.17	1415.3	0.551
	14	749.03	1392.7	0.538
	15	721.46	1430.1	0.505
	<i>Average</i>	<i>767.40</i>	<i>1426.3</i>	<i>0.538</i>
	<i>S.D.</i>	<i>34.67</i>	<i>30.35</i>	<i>0.02</i>
Azobe	16	3879.58	3873.4	1.234
AZ_45_120	17	2775.83	3547.8	0.782
	18	4628.59	3975.0	1.391
	19	3950.66	3815.2	1.743
	20	6639.62	4118.3	2.584
	<i>Average</i>	<i>4374.86</i>	<i>3865.9</i>	<i>1.119</i>
	<i>S.D.</i>	<i>1429.66</i>	<i>211.79</i>	<i>0.28</i>

5.3. Modulus of elasticity

As mentioned earlier, the determination of the MoE and tensile strength is different from the determination of the fracture energy and density. Both the fracture energy and the density can directly be determined from the experiment using Eq. 2.9 for the fracture energy and simply calculating the weight/volume ratio for the density. The MoE and tensile strength can not directly be determined from the experiment and require a different approach using a numerical model and a back-analysis. In Section 3.4.6 the procedure is described in detail. The input of the back-analysis is an initial estimation of the MoE based on applying Hooke's law with the strain and stress values of the UN-TPB test. In Tab. 5.3 the initial estimations along with the result of the back-analysis is shown.

The initial estimation of the MoE values deviate significantly from the result of the back-analysis. Unfortunately, the UN-TPB test is not performed with different orientations of the growth rings for the azobé specimen, and can thus not be compared with the result of the back-analysis. The results of the back-analysis slightly deviate from the prescribed

Table 5.3: The modulus of elasticity prior to and following the back-analysis.

Series	Young's modulus (N/mm ²)	
	Initial estimation ¹⁾	Result back-analysis
SP_45_80	222	400
OA_45_80	808	1000
BI_45_80	1893	1050
AZ_45_80	2313	2200
AZ_0_80	-	1500
AZ_90_80	-	2600
AZ_45_120	-	2200

¹⁾ The initial estimation is determined from the UN-TPB test, see Section 3.4.6.

MoE values in the Eurocode. In the Eurocode the prescribed MoE values perpendicular to the grain are 400, 730, 930 and 1330 N/mm² for spruce, oak, bilinga and azobé respectively¹ (European Standard, 2016). All other parameters in the back-analysis are kept constant. The input for the fracture energy, is the value shown in Tab 5.8.

Regarding the relation between the orientation of the growth rings and the MoE, a significant dependency is seen. Although the sample size is very small, a correlation coefficient is found of 0.98 between the angle of the growth rings and the MoE. In literature a similar correlation is found. Fig. 2.4 shows the relation between the orientation and the MoE. The change in MoE between 0- and 90-degrees is similar to what is obtained in this research. The difference is that the drop in MoE in Fig. 2.4 for the intermediate angles of the growth rings is not seen in the results here. The MoE under 45-degrees is higher than for 0-degrees, which is in contrast to what is seen in Fig. 2.4.

There is no difference between the MoE value of the AZ_45_80 and the AZ_45_120 series. This is expected as the MoE is an intrinsic mechanical property, meaning it is independent of the specimen size.

5.4. Tensile strength

Similar to the MoE, the tensile strength is also estimated using a combination of the experimental results and the numerical model in a back-analysis. There are some differences to the back-analysis of the MoE, these are stated in Section 3.4.6. A notable difference is in the initial estimation of the value for the tensile strength. In the MoE back-analysis the initial value is determined with UN-TPB test results. Because the tensile strength needs to be determined from the onset of cracking this initial estimation is obtained from the SEN-TPB test results. The initial estimation is determined from the estimation of the MoE

¹In the Eurocode the elastic properties of the wood species are categorized in a strength class. The designation of a certain wood specie to a strength class is stated in NEN-EN 1912 (European Standard, 2012). The designated strength classes for the wood species relevant in this research are: spruce = C30, oak = D30, bilinga = D50 and azobé = D70.

(Section 5.3) and the strain values at onset of cracking from the SEN-TPB test. In Tab. 5.4 these initial values for the tensile strength are shown. These values are then calibrated in the back-analysis by comparing the peak load of the experimental and numerical load-displacement curve.

Table 5.4: The tensile strength prior to and following the back-analysis.

Series	Tensile strength (N/mm ²)	
	Initial estimation	Result back-analysis
SP_45_80	4.4	3.5
OA_45_80	9.7	9.7
BI_45_80	4.2	4.2
AZ_45_80	8.9	11.0
AZ_0_80	7.5	5.0
AZ_90_80	11.4	11.0
AZ_45_120	6.8	10.0

Similar to the back-analysis of the MoE, most of the initial estimations of the tensile strength require some iteration to calibrate the value. Only the OA_45_80 and BI_45_80 series requires no calibration for the numerical model to fit with the experimental results.

Similar to the MoE, there is a strong dependency of the tensile strength on the orientation of the growth rings. However, where the MoE increases linearly with the orientation, the influence on the tensile strength is different. The tensile strength in the 45- and 90-degree orientation is the same, but the tensile strength in 0-degrees is significantly lower.

The results here show the underestimated values stated in the Eurocode (2016). In the Eurocode a constant value for the tensile strength perpendicular to the grain is stated for all hardwood species. The prescribed value 0.6 N/mm² is significantly lower than the 11.0 N/mm² for azobé. An experiment by Kovryga et al. (2020), conducted on beech and ash, shows a range for the tensile strength between 4 and 10 N/mm². The density of both wood species is similar to the density of oak and bilinga, for which a tensile strength value is found of 9.7 and 4.2 N/mm². Although the values approximately lie within the range found by Kovryga et al. (2020), the scatter is too large to make any convincing conclusions.

5.5. Correlation material properties

According to Blaß and Sandhaas (2017) and Reiterer et al. (2002), most mechanical properties are positively correlated to the density of the wood specie. To verify this statement the correlation coefficient is computed between the density, the calculated material properties and the micro-structural properties. In Tab. 5.5 the correlation coefficients are shown for the series in 45-degrees. The calculation of the coefficient between the material properties and the micro-structural properties is limited to the hardwood species as the microscopic composition of spruce is different. The correlation coefficient with the microscopic

composition is determined with the volume percentage of the considered cell type. The coefficients are based on linear regression. In Tab. 5.5 the green colored cells indicate a positive correlation and the blue colored cells a negative correlation.

Table 5.5: Correlation coefficients material properties.

	Density	Fracture energy	MoE	Tensile strength
Density				
Fracture energy	0,950			
MoE	0,990	0,901		
Tensile strength	0,789	0,843	0,781	
Vessel	-0,341	-0,638	-0,350	-0,952
Parenchyma	0,924	0,768	0,969	0,706
Rays	0,398	0,560	0,272	0,106
Fibers	0,813	0,569	0,808	0,038

Tab. 5.5 indeed shows a positive correlation between the density and the mechanical properties determined in this research. The table also shows how the mechanical properties are correlated to the microscopic structure of wood. In Fig. 5.1 the correlation between the density and the fracture energy is shown. In the figure the linear relation found by Larsen (1990) is shown along with the linear relation found in this research. The accuracy of the predicted regression is evaluated by the mean absolute error (MAE). The MAE is a measure how large the spread is between the observed results and the predicted results. Evaluating the fracture energy results of this research with the linear relation found by Larsen (1990) yields a MAE value of 0.202. The new linear relation yields a MAE value of 0.079. Thus on average the error between the new linear relation and the result data from the bending test is 0.079 N/mm.

5.6. Characteristic length

The characteristic length is a measure for the size of the cohesive zone. Note that the value found for the characteristic length is not exactly the length of the cohesive zone, but a variable derived from material properties which influence the size of the cohesive zone. The brittleness number also takes into account the size of the tested sample and is a measure for the "brittleness" of the specimen. The brittleness of a material is a measure of the amount of elastic and plastic deformation prior to fracture. For a brittle material (high value for the brittleness number) there is less elastic and plastic deformation and less energy stored in the material. The characteristic length is determined according to Eq. 2.8, the brittleness number is simply the height of the beam divided by the characteristic length, $B = h/l_{ch}$. Unfortunately the value found for the cohesive zone according to Eq. 2.8 could not be compared with images from the DIC. In order to estimate the size of the cohesive zone, the exact location must be known where the stress is equal to zero and a traction-free crack is formed. This is very difficult to determine from the DIC images and therefore the comparison can not be made. In Tab. 5.6 the characteristic length l_{ch} and the brittleness

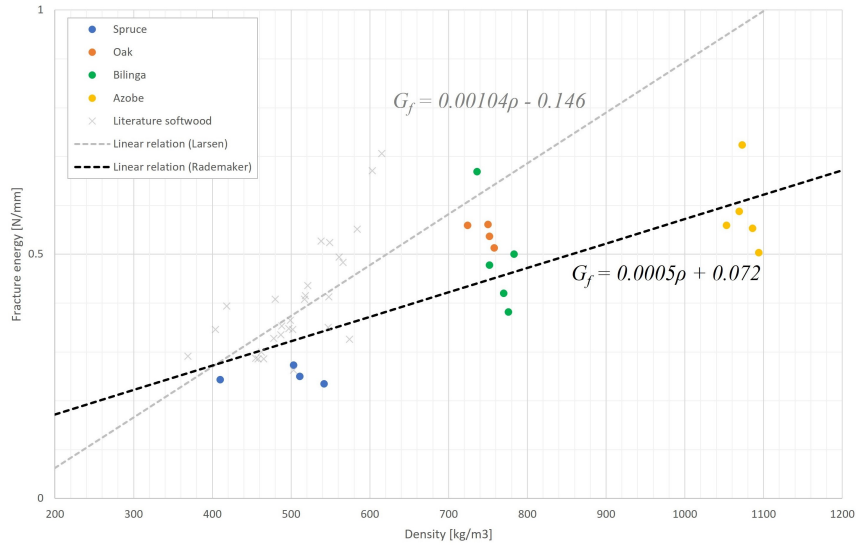


Figure 5.1: Correlation between the density and the fracture energy, with values from literature and this research.

number B are shown for all the considered series. In the determination of the parameters, the material properties stated in Tab. 5.8 are used.

Table 5.6: Characteristic length and brittleness number of the test series.

Series	Characteristic length (mm)	Brittleness number (-)
SP_45_80	8.16	9.80
OA_45_80	5.76	13.89
BI_45_80	17.00	4.71
AZ_45_80	11.93	6.71
AZ_0_80	66.60	1.20
AZ_90_80	9.86	8.11
AZ_45_120	53.24	2.25

Tab. 5.6 shows that for the BI_45_80, the AZ_0_80 and the AZ_45_120 series the characteristic length and thus the cohesive zone is significantly larger than for the other series. That is mainly due to a larger value for the fracture energy. A larger value for the fracture energy means a more gradual developing crack path, and thus a larger cohesive zone. This is also supported by the post-peak behaviour in the load-displacement curve for these series (Fig. 4.1). A notable remark from Tab. 5.6 is the relatively large brittleness number for oak. This number is larger than the AZ_45_80 and AZ_90_80 series. The load-displacement curve of oak in Fig. 4.1 would not suggest that the oak series is more brittle than the two azobé series. The reason for this is the high estimated value for the tensile

strength for oak. Future research is required on the exact value for the tensile strength of oak, to evaluate if this high brittleness value is accurate for oak. The other values found for the brittleness indicate how much strain energy U_s is stored in the system prior to fracture. The BI_45_80, the AZ_0_80 and the AZ_45_80 show a low brittleness number, meaning relatively more strain energy is stored in the system. For the BI_45_80 and AZ_0_80 series this is due to a more dominant role of the material non-linearity in the form of micro-cracking and fiber-bridging. For the AZ_45_120 series this is due to the lower slenderness ratio of the beam and thus a less linear-elastic distribution of horizontal stresses over the height of the beam.

5.7. Evaluation of the material properties

5.7.1. Key findings

In this subsection the key findings of the experiment are presented.

- Uniform fracture energy value for the hardwood species (for growth ring orientation 45-degrees).
- The fracture energy value of the AZ_0_80 series is a ratio 1.89 higher than the other orientations.
- The fracture energy value of the AZ_45_120 series is a ratio 1.91 higher than the AZ_45_80 series.
- Large deviation between the initial estimation and the result of the back-analysis for the MoE.
- High positive correlation between the growth ring orientation and the MoE.
- No drop in the MoE in the 45-degree orientation.
- No difference in the MoE and tensile strength value between AZ_45_80 and AZ_45_120 series.
- Accurate initial estimations of the tensile strength.
- Relatively low tensile strength value for bilinga.
- The tensile strength value of the AZ_0_80 series is a factor 2.24 lower than the other orientations.

5.7.2. Interpretation of the results

Most of the key findings of the estimation of the material properties are in line with the findings from the qualitative study in Section 4. In this section the key findings above are interpreted and compared to literature and to the qualitative observations from the experiments.

Fracture energy

Larsen (1990) stated in his research a linear relation between the density and the fracture energy of wood. According to Eq. 2.10 the fracture energy of the wood species in this research should be 0.365, 0.630, 0.648 and 0.972 N/mm for spruce, oak, bilinga and azobé respectively. These values differ significantly from the results from the experiment, Tab. 5.2. The fracture energy of spruce is in line with literature (Tab. 2.3) but the fracture energy of the hardwood species reaches a plateau around 0.5 N/mm. Eq. 2.10 can thus not be applied to higher densities. However, this is only based on one hardwood specie above 800 kg/m³. To properly confirm that the equation is only limited to lower and medium densities, more hardwood species above 800 kg/m³ should be tested. Unfortunately there is not much literature available on fracture behaviour of higher density hardwood species. For the evaluation of the fracture energy results for azobé, the results are compared with experiments performed by Gijzenberg (2022) and Boerenveen (2019). Both studies are also performed with a SEN-TPB test and the same specimen geometry is used. An important remark is that the tests performed by Gijzenberg are only in the TL-orientation, i.e. the growth rings are under 0-degrees. In the comparison a distinction is made between unstable and stable fracture behaviour and between calculations performed with the exact cracked area and an estimated cracked area. In the calculation of the fracture energy (Eq. 2.9) with an estimated cracked area, the area is calculated by multiplying the length of the crack a_c from the DIC images with the width of the specimen b . The exact cracked area is determined with the optical profilometer, see Section 4.2. The second distinction made is in unstable and stable post-peak behaviour. In this research only two azobé (45-degrees) samples behaved in a stable manner, samples 22_NAZ_2 and 23_NAZ_3 (Fig. 4.4d). Note that there is a small drop in the load-displacement curve of sample 22_NAZ_2, however this drop is relatively small and can thus be considered stable. In the research by Boerenveen three of eleven tests were stable.

Table 5.7: Comparison of the mean and standard deviation values for the fracture energy of azobé with the estimated cracked area and the exact cracked area.

Source	Fracture energy G_f (N/mm)			
	Estimated A_c		Exact A_c	
	<i>Unstable</i>	<i>Stable</i>	<i>Unstable</i>	<i>Stable</i>
This research (AZ_45_80)	0.82 (0.06)	0.92 (0.06)	0.54 (0.03)	0.66 (0.07)
(Boerenveen, 2019)	0.66 (0.06)	0.98 (0.18)	–	–
This research (AZ_0_80)	–	1.29 (0.32)	–	1.11 (0.18)
(Gijzenberg, 2022) (TL)	–	1.34 (0.17)	–	–

The most realistic value for the fracture energy is obtained by a stable test where the exact cracked area is used to determine the value for the fracture energy (Aicher, 2009; Larsen, 1990). This value for azobé is 0.66 N/mm. Unfortunately the exact cracked surface area is not determined by the other two researchers and can therefore not directly be

compared. However, from the values with the estimated cracked area, it can be seen that the stable fracture energy values are similar for both series. Please note, the sample size for both analysis is small. The research from Boerenveen had three samples with a stable crack propagation and a relatively large standard deviation. The standard deviation of this research is smaller but the sample size is also very small with only two stable crack propagation samples. So no convincing conclusions can be made in this comparison. For the AZ_0_80 series (Fig. 4.4e) unstable crack propagation is not a factor, no large drops in stiffness/load occurred during the loading process. The fracture energy in the TL-orientation obtained in this research is similar to the results obtained by Gijzenberg. From both experiments a fracture energy value of 1.3 N/mm^2 is obtained with the estimated crack area. Thus the azobé fracture energy value in the TL-orientation coincides with the results from Gijzenberg. With the exact cracked area a more accurate value for the fracture energy is obtained, 1.11 N/mm^2 in the TL-orientation.

One of the key findings of the qualitative study is the variation of the failure mode (Fig. 4.11), the total cracked surface area and slope of the softening curve between the different orientations of azobé. In the quantitative study a similar inconsistency is seen in the values for the fracture energy of azobé. Larsen (1990) conducted a study where the growth ring orientation is taken into consideration for spruce samples. In Annex A6 of his meta-study the conclusion is made that the fracture energy decreases with increasing angle of the growth rings. For spruce the report stated that the fracture energy for growth ring orientation 0-degrees is 1.6 times larger than the fracture energy in 90-degrees. In this report a slightly higher ratio was found, 1.89 for the azobé series. However the volume fraction of rays in azobé is higher than in spruce (Tab. 2.1). Contradicting results are found in the study by Reiterer et al. (2002), where the fracture energy values for spruce and oak in 0-degrees are actually lower than 90-degrees. In Fig. 5.2 the load-displacement curve of several wood species is presented in the two different orientations. From these curves the values for the fracture energy of spruce and oak are found and are shown in Tab. 5.7. As can be seen, the fracture energy under 90-degrees is larger than under 0-degrees, a contradictory result to the fracture energy values for azobé in the different orientations (Tab. 5.2). Although the results of the fracture energy are contradictory, the difference in the peak load of the different orientations is similar to this research. The peak load found by Reiterer is under 90-degrees a factor 1.54 and 1.48 higher than under 0-degrees for spruce and oak respectively. In this research the peak load of azobé under 90-degrees is a factor 1.48 higher than in the 0-degrees orientation.

Thus for the peak load similar results are obtained, whereas for the fracture energy contradicting results are seen in the comparison between the orientations. The reason behind this inconsistency can again be explained by the anatomy of the different wood species. In Section 6.3.3 it is explained that the peak load is influenced by the amount and orientation of the rays. Meanwhile, the shape of the softening curve and the decrease in post-elastic stiffness is determined by the parenchyma cells. Now, the composition of rays in oak and azobé is similar (Tab. 2.1). This results in a similar dependency of the peak load on the orientation of the sample. In contrast to azobé the amount of parenchyma cells in spruce and oak is low. Therefore, the shape of the softening curve and post-elastic stiffness is less affected by the orientation of the sample. Where in Fig. 4.1 there is a significant difference between the post-elastic behaviour for azobé, in Fig. 5.2 this difference is less pronounced

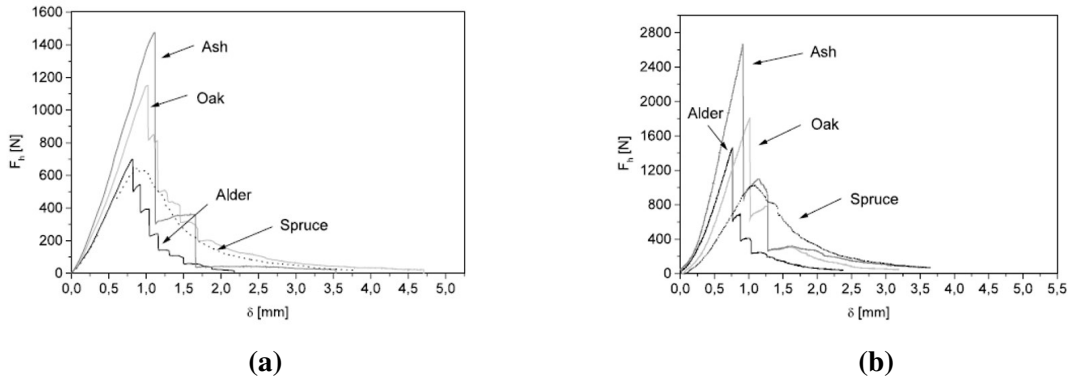


Figure 5.2: Load-displacement curves of a wedge splitting test with the growth rings under an angle of (a) 0 degrees (TL-orientation) and (b) 90 degrees (RL-orientation). From (Reiterer et al., 2002).

for spruce and oak. The fracture energy is thus higher due to the higher peak loads in the RL-orientation.

In Tab. 5.7 there are fracture energy results which are determined with other test setups or specimen dimensions. The results from the SEN-TPB tests performed by Larsen (1990) and Aicher (2009) are comparable to the results from this experiment. The dimensions of the test specimens only slightly deviate from the test setup used here. In Annex A6 the width is 45 mm and in the study by Aicher the tests were performed on specimens with a height of 10 mm to 320 mm. The studies by Reiterer et al. (2002) and Reiterer and Tschegg (2002) are performed with a different test setup, which led to a smaller value of the fracture energy. However not enough research is performed to conclude that the fracture energy is dependent on the test method. The value for the fracture energy obtained in this research is comparable to the results obtained from experiments performed with the same setup and specimen dimensions.

A notable difference is between the fracture energy of the AZ_45_80 and the AZ_45_120 series. An increase in height of 1.5 leads to an increase in the fracture energy of 1.9. In the meta-study by Larsen (1990) a study is performed on the size-effect of the fracture energy. The study concludes an increase in fracture energy of 20% when the height is doubled. The increase in this research is thus much more significant than in the study by Larsen. A second reference on the size-effect of the fracture energy is the study by Aicher (2009). Aicher also found a minor size-dependency of the fracture energy of spruce (Tab. 2.3). In both studies a SEN-TPB test setup is used. However, the difference with the test setup in this research is that the initial notch length here is not adjusted accordingly. In both references the initial notch length is changed according to $a_0 = 0.6h$, while in this experiment the initial notch length is kept constant at 48 mm. The stiffness of the AZ_45_120 is thus not proportional to the AZ_45_80 series. This is the probable cause of the large increase in the fracture energy when the height is increased from 80 to 120 mm. Because the initial notch length is not adjusted accordingly in this research, the strain distribution changes over the height of the beam. Meaning that the stored strain energy in the system is not in proportion to the smaller beam (AZ_45_80 series) where the initial notch length is equal to $0.6h$. The specimen in the AZ_45_80 series is more slender than the AZ_45_120 series meaning

that the beam fails in a more brittle manner. This can be seen from the load-displacement curves, Fig. 4.4d and 4.4g. Brittle failure is characterized by unstable fracture, which is not a factor for the AZ_45_120 series. For a proper comparison with literature and a definite conclusion of the size-effect of the fracture energy, the initial notch length had to be adjusted accordingly.

Modulus of elasticity

A notable observation from the MoE results, is the difference between the initial estimation and the end result of the back-analysis, see Tab. 5.3. This difference can be explained by the methodology of the initial estimation. The first step in the determination of the MoE is estimation the values from the UN-TPB test. In the computation of the MoE, the strains are obtained from the DIC files of the UN-TPB test. A difference between the UN-TPB test and the main SEN-TPB test is that in the UN-TPB test no LVDT's are used. Recall that the function of the LVDTs is to measure the vertical displacement. Therefore, the displacement had to be measured with the DIC as well. Thus the DIC cameras had to cover both mid-span and the support to measure the relative displacement between the two points. This led to a reduction of the resolution of the DIC images compared to the DIC images of the SEN-TPB where only an area around mid-span is recorded. A consequence is that small strains are difficult to measure. Thus the smaller the strains, the less accurate the initial estimation of the MoE is. A second reason for the difference could be the small sample size on which the initial estimation is based. Only one unnotched sample for each wood specie is tested, except for azobé where two sample are tested.

Two key observations are made regarding the relation between the orientation of the growth rings and the MoE. Firstly, a strong correlation is seen between the density and the MoE. Literature states that characteristics of wood are often related to the density of the wood species. Ravenshorst (2015) states that the density is an indication of the number of fibres in a wood species. The results of this research support this statement as the correlation coefficient between the density and the number of fibers is 0.81. Therefore, the overall strength of hardwood is related to the amount of fibres in a wood specie (Danielsson, 2013). Thus, according to the statements above and Tab. 5.5, the density should give an indication of the MoE of a wood specie. The influence of the growth ring orientation on the MoE shown in Fig. 2.4 indicates a reduction of the MoE between 0- and 90-degrees. This reduction is not seen in the estimation of the MoE for the AZ_45_80 samples. The explanation for this drop in Fig. 2.4 is due to the influence of rolling shear. Due to compression in the RT-plane the rolling shear action reduces the stiffness. Because in this experiment the fracture behaviour is mainly mode-I, there is no compression and thus the rolling shear action has no influence. Rolling shear could be of importance in mode-III fracture (Fig. 2.10). Results from the DIC file show that there is negligible relative displacement out-of-plane, and thus there is no mode-III action.

Tensile strength

In contrast to the MoE results, the initial estimations of the tensile strength are much more comparable to the eventual result of the back-analysis. This can be explained by the use

of the same test setup for the initial estimation and the back-analysis. For both the initial estimation and the back-analysis the SEN-TPB test is used which has a better accuracy than the UN-TPB test (for explanation: see above).

Tab. 5.4 shows a couple of notable results. Firstly, an unexpected low tensile strength value for bilinga is obtained². This result is unexpected because of the high density (Tab. 5.1) and high stiffness value (Tab. 5.3) of bilinga. Moreover, according to Ravenshorst (2015) and Danielsson (2013) the density and overall strength are related to the quantity of fibers in a wood specie. The quantity of fibers in bilinga is comparable to the other hardwood species (Tab. 2.1), which would suggest a comparable tensile strength value. Although there is not a perfect correlation between the quantity of fibers, the density and the tensile strength, the difference between bilinga and oak and azobé is significant. A possible explanation for the lower strength of bilinga could be explained by the high number of vessels in the wood specie. From Tab. 2.1 and Fig. 4.8a it can be seen that the number of vessels is higher than the other hardwood species in this research. The higher percentage of vessels could explain the reason behind the lower tensile strength value than expected, which is also substantiated by the high negative correlation coefficient between the quantity of vessels and tensile strength (Tab. 5.5). However, this would also suggest that the stiffness of bilinga should also be lower compared to the other hardwood species, which to some extent is not the case. On the contrary, a higher value for the tensile strength is expected when considering the quantity of rays in bilinga. It is mentioned earlier that rays act as reinforcement if loaded in their direction. According to Tab. 2.1 the percentage of rays in bilinga is higher than oak and azobé, suggesting a higher tensile strength value. It is thus unclear what the exact cause is for the relatively low tensile strength value of bilinga. Further research is required on the micro-structure of bilinga or a different test setup is needed to more accurately determine the tensile strength.

A second notable observation from the tensile strength results is the low value for the AZ_0_80 series compared to the other azobé series. The explanation for this difference is again the orientation of the rays and parenchyma cells. Due to the thick-walled rays, the strength and stiffness of the material increases when the sample is loaded in the direction of the rays. In the case of the AZ_0_80 series, the rays are orientated parallel to the fracture surface and thus do not contribute to this increase in strength. A more elaborate explanation is given in Section 6.3.3.

5.8. Limitations of the experiment

The results are limited by a couple of factors. First of all, the sample size of this experiment is relatively small. For each series only five samples were tested. According to the law of large numbers, if the sample size is low, the mean value obtained in the experiment might not be an accurate representation of the real expected value. For the azobé series this

²After calibration of the numerical model, the tensile strength for bilinga is readjusted from 4.2 to 5.5 N/mm². The reason for this is the change in shape of the tension softening curve from linear to bi-linear. In the back-analysis a linear softening curve is used. However, the experimental results and numerical model calibration shows that a bi-linear tension softening curve is more accurate and applicable to bilinga. For a more elaborate explanation, see Section 6.3.3 and 6.4.

consideration is important as the results from unstable cracking should be excluded in the determination of the material properties. In the case of the AZ_45_80 series, only two out of the five samples cracked in a stable manner. Furthermore, the samples within each series are sawn from the same beam, meaning that the obtained results only represent a single tree. This limits the generalizability of the results.

In Section 6.3.3 the relation between the fracture process and the orientation of the growth rings is treated. The conclusions made here are based on three orientations, 0, 45 and 90 degrees. Due to lack of data of the intermediate orientations of the growth rings, the results can not prescribe the fracture behaviour in these intermediate orientations.

In this research evaluation of the fracture energy and its dependency of the orientation in which the sample is placed, is only limited to one wood specie. To confirm the results and conclusions regarding the dependency on the orientation of the sample, more wood species with different compositions of the cell types are required in a more comprehensive study. However, based on the connection between the anatomy, i.e. the composition of cells, an estimation can be given on the fracture process and the properties related to fracture.

5.9. Conclusions

Some of the key observations of the quantitative analysis can be explained by the orientation of the rays and parenchyma cells, see Section 6.3.3. The higher value for the fracture energy and the lower value for the tensile strength of the azobé series in 0-degrees can be explained by the orientation of the rays and parenchyma cells. This also explains the high correlation between the growth ring orientation and the mechanical properties. The mechanical properties for each series is summed up in Tab. 5.8.

Table 5.8: Mechanical properties for each series.

Series	Fracture energy (N/mm)	Modulus of elasticity (N/mm ²)	Tensile strength (N/mm ²)
SP_45_80	0.250	400	3.5
OA_45_80	0.542	1000	9.7
BI_45_80	0.490	1050	5.5 ²⁾
AZ_45_80	0.656 ¹⁾	2200	11.0
AZ_0_80	1.110	1500	5.0
AZ_90_80	0.534 ¹⁾	2400	11.4
AZ_45_120	1.119	2200	6.8

¹⁾ Only stable fracture is considered here.

²⁾ Numerical calibration and change in shape of softening curve shows that the tensile strength had to be readjusted (Section 6.4).

The results obtained in this research are in line with literature and previous experiments performed on the fracture energy of softwood and hardwood. The average fracture energy

value for spruce is similar to the values obtained in studies by Aicher (2009), Larsen (1990) and Reiterer (2002). Furthermore, the results of the hardwood samples is comparable to the results from studies by Boerenveen (2019) and Gijzenberg (2022). More accurate results are obtained by computing the exact cracked surface. A limitation of the results is the small sample size due to unstable fracture results. Nonetheless, the scatter in the results is very small and are similar to the results by Boerenveen and Gijzenberg. A comparison of tensile strength and MoE with literature is difficult. There is limited literature available on the mechanical properties of hardwood, and not the ideal test setup is used to determine the tensile strength and the MoE.

A secondary goal of the experiment is to investigate the linear relation between the density and the fracture energy, as found by Larsen (1990). The linear relation, Eq. 2.10, found by Larsen (1990) does not apply to hardwood species with an density above 700 kg/m^3 . The three hardwood species tested in this experiment, all have a fracture energy value around 0.5 N/mm . The fracture energy thus reaches a plateau around 0.5 N/mm . This is based on the results of this experiment with three hardwood species. It should be noted that this value for the fracture energy only applies to an orientation of the growth rings of 45-degrees.

A strong dependency between the fracture process of azobé and the orientation of the growth rings is found in this research, see Tab. 5.8. This is due to the orientation of the rays and longitudinal parenchyma cells. The orientation where the rays are orientated perpendicular to the crack plane will result in a higher peak load. Meanwhile, the thin-walled parenchyma cells significantly reduce the post-elastic stiffness. The orientation where the parenchyma cells are orientated perpendicular to the crack plane, has a higher value for the fracture energy. This theory corresponds to the results found by Reiterer (2002). For wood species with a lower amount of parenchyma cells, the dependency between the fracture process and the orientation of the sample is less strong.

No definite conclusions can be made regarding the size-effect of the fracture energy. The initial notch length and span of the AZ_45_120 series are not in proportion to the smaller AZ_45_80 series. The dimensions of the beam are related to a parameter a as defined by Nordtest (1993). The defining parameter a is the height of the beam, and thus the length of the initial notch ($0.6a$) and span ($7a$) should be adjusted accordingly, which was not the case. For a complete overview of the test setup, see Section 3.4.2. Although a minor size-effect of the fracture energy is found in literature, this can not be compared to the results in this research.

A secondary research goal of the experiment is to investigate whether the results of this research can predict fracture behaviour of wood species not tested in this research. The results of both the qualitative and quantitative study show that an estimation of the fracture process can be given based on the micro-structure of the wood specie and the orientation is which it is placed. The quantity of the different cell types and the orientation is which they are placed during fracture influence both the mechanical properties of the material but also the softening behaviour and the crack propagation process. Thus if the micro-structure of the specie is know and attention is drawn to the orientation of the structural element, an estimation of the fracture process can be given. Combining the knowledge of this experiment with a numerical (Section 6) and analytical model (Section 7.1), the fracture process of an arbitrary chosen structural element can be predicted.

NUMERICAL MODELLING

6.1. Introduction

In this Chapter the focus is on the numerical modelling of the fracture behaviour of hardwood. The results of both the qualitative (Chapter 4) and the quantitative study (Chapter 5) are combined to form an accurate numerical model to be used in practical applications. The emphasis is made here on the material and fracture model which can validate the results from the experiment. The numerical model has two functions/goals: 1) the calibration of the material properties and 2) the calibration/validation of an accurate numerical model. In Section 5 the calibration of the material properties is performed, in this section the focus is on the numerical model itself.

In Section 1.4 the research question is stated in relation to the numerical model. "How can the results of this experiment be implemented in a discrete cracking model?", is a question which will be answered in the calibration of the numerical model, where knowledge from the literature study (Section 2.3) is applied to this research. In addition to these research question, the results of the experiment give rise to new questions regarding the numerical model:

1. The AZ_0_80 and BI_45_80 series show a relative irregular fracture surface. How can this be taken into account in a two-dimensional numerical model?
2. What is the most accurate shape of the tension softening curve?
3. Does the numerical model show similar unstable cracking behaviour for the AZ_45_80 and AZ_90_80 series?

6.1.1. Scope and limitations

In general, the goal of a numerical analysis is to predict and approximate the behaviour of a structural element. The numerical model involves many parameters which influence the stability and accuracy of the numerical model. As this thesis is only focused on a select part of the overall behaviour of wood, it is important to mention what is included in the numerical model and which assumptions are made regarding aspects of the material model which are outside the scope of this research.

- The numerical analysis is performed in DIANA FEA v10.4 (education version).
- Only a two-dimensional model is analysed. The structural elements are modelled with plane stress elements. This means that the stress components perpendicular to the face of the element are equal to zero. According to the DIC files there is almost no displacements and strains out-of-plane, thus the bending action outside the plane of the structure is negligible.
- Two models are considered to modelling the fracture process: a discrete cracking model and a rotating smeared cracking model. Both models consider cracking of the material as isotropic.
- Material properties not determined in this thesis are retrieved from literature or the Eurocode (NEN-EN 338 (2016)).
- Similar to the experiments, the load is applied in displacement control.
- A structural nonlinear analysis is performed with both physical and geometrical non-linear effects. The type of geometrical non-linearity is a total Lagrange, meaning all variables are formulated with respect to the initial configuration.
- It is assumed that there is no distinction between the radial and tangential orientation regarding the Poisson's ratio ($\mu_{LR} = \mu_{LT}$). According to Green (1999), there is a minor difference between both Poisson's ratio, however the influence of this difference is negligible.

6.1.2. Methodology

First, the numerical model of the SEN-TPB test setup is prescribed. This includes the description of the finite element model in DIANA, the finite element types and the geometry of the elements. Next the material model is described in detail. With knowledge from the literature study (Section 2.3) and the estimation of the material properties, an initial material model is constructed. This material model is presented in Section 6.2. In addition to a description of the material properties, the non-linear material behaviour and the cracking models are prescribed. It is explained which cracking model is used and how the tension softening behaviour is prescribed.

This initial numerical model is run in a non-linear structural analysis. The results are then compared with the results from the experiments. First, the load-displacement curves are compared for each series. The linear elastic curve should be identical as the MoE is estimated based on the numerical and experimental results. The focus is thus mainly on the peak load and the softening curve of the load/displacement curves. These characteristics are mainly the result of the tensile strength, fracture energy and the shape of the tension softening curve. The chosen fracture model has also a major influence on the fracture process. In addition to the load/displacement curve, the crack width of the experimental and numerical is determined. This is done by evaluating the crack tip opening displacement (CTOD) at the notch end during the fracture process. This curve gives an indication of the moment cracking is initiated at the notch end. For both the load-displacement and the

CTOD curves various load levels are shown. These load levels are chosen at distinctive moments in the fracture process. These load levels are chosen at: (A) the tensile strength reached at notch-end, (B) the peak load, (C) a traction-free crack is initiated at notch-end and (D) complete failure/separation of the sample. Load level (C) is the moment that the traction in the node at notch-end is equal to zero. The relative displacement between the opposite nodes in the elements has then reached the critical value w_c (see Fig. 2.8). For load levels (A) and (C) the horizontal traction (traction in the local y-direction) in the node at notch end is considered. Due to the addition of the load support and the boundary conditions, the specimen will not completely separate, but instead rotate around the upper most node. Load level (D) is when the relative displacement in the integration point closest to the upper most node is not equal to zero. The comparison of different wood species or orientations on a specific load level reveal the characteristic features of the fracture behaviour.

Based on the results of the initial model, the numerical model is calibrated in order to suggest an accurate fracture model for the fracture behaviour of hardwood. The chosen cracking model and constitutive model are evaluated. The most accurate material model is then presented for each series.

6.2. Numerical model

6.2.1. Finite element model

The numerical analysis is performed in a two-dimensional space. The element type which is used to model the material are 8-noded quadrilateral plane stress elements. In Fig. 6.1 the numerical model is shown. The figure shows the geometry of the test specimen similar to Fig. 3.1 along with the boundary conditions and the location of the applied load. In the numerical model three different boundary conditions can be distinguished. The beam is simply supported at both ends, where on the left side the support constrains movement in the x- and y-direction and at the right support only the vertical displacement is constrained. The third boundary condition is at the location of the applied load. Here the prescribed displacement is applied in the vertical direction. Rotation is unconstrained at all support locations. No constrains are applied in the z-direction. The applied prescribed vertical displacement is applied at mid-span, shown by the green arrow. The vertical displacement applied is 10 mm in the negative y-direction. Self-weight is excluded from the numerical model. In the experiments the self-weight is excluded in the results by making use of counterweights (Fig. 3.2) equal to the weight of the sample.

Geometry

The geometry of the numerical model is comprised of three main parts: the spruce end parts, the middle hardwood part and the support plates. In Tab. 6.1 the dimensions of the geometry are shown. There is a minor difference in the length of the middle part between the spruce, oak and bilinga part and the azobé part. This is due to limitations in the size of the azobé logs, see Section 3.4.2. For the AZ_45_120 series the height is adjusted to 120

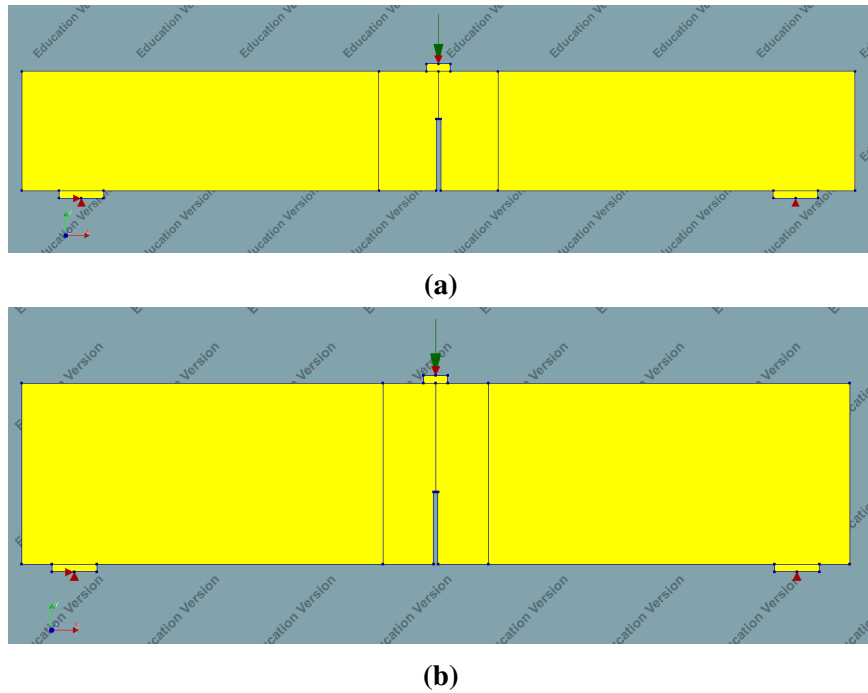


Figure 6.1: The finite element model of the SEN-TPB test for (a) the series with a height of 80 mm and (b) with a height of 120 mm.

mm. The dimensions of the support and load plates remain unchanged. To meet a span of 480 mm for the azobé specimens, the spruce end parts are both shifted 5 mm at each end to account for the shorter middle azobé part. For the spruce end parts the direction of the local/element axis coincides with the global axis, the direction of the x-axis is in the direction of the beam and the fibers of the spruce parts. The middle part in the experiment is shifted 90-degrees. This is also done for the numerical model, where the direction of the local axis is shifted 90-degrees compared to the global axis.

Table 6.1: Element geometries.

Element	Thickness (mm)	Height (mm)	Length (mm)	Element x-axis
Spruce end part	40	80	240	Global x-axis
Middle part (SP, OA, BI)	40	80	40 ¹⁾	Global y-axis
Middle part (AZ)	40	80	35 ²⁾	Global y-axis
Support plate	50	5	30	Global x-axis
Load plate	50	5	16	Global x-axis

¹⁾ At height 0 to 48 mm the length of the element is 38.5, this is due to the location of the initial notch.

²⁾ At height 0 to 48 mm the length of the element is 33.5, this is due to the location of the initial notch.

Table 6.2: Finite element types.

	Plane stress elements	Line interface elements	Point interface elements
Full element name	8-noded quadrilateral plane stress element (CQ16M)	3+3-noded two-dimensional interface element (CL12I)	1+1-noded two-dimensional interface elements (N4IF)
Dofs per element	16	12	4
Interpolation scheme	Quadratic	Quadratic	-
Integration scheme	2x2	4-point Newton-Cotes	-
Shape dimension	2-D	2-D	2-D
Topological dimension	2-D	1-D	1-D
Stress components	$\sigma_{xx}, \sigma_{yy}, \sigma_{xy}$	$\sigma_{xx}, \sigma_{yy}, \sigma_{xy}$	σ_{xx}, σ_{yy}
Shear deformation	Yes	Yes	No
Average element size (mm)	10 ¹⁾	1	1
Nr. of elements (h = 80)	7230 ²⁾	48	2
Nr. of elements (h = 120)	9964 ³⁾	88	2

¹⁾ The average element size of the mesh generated for the hardwood parts of the beam is on average 1 mm.

²⁾ The nr. of elements of the spruce parts and the middle hardwood part is 900 and 6296 elements respectively.

³⁾ The nr. of elements of the spruce parts and the middle hardwood part is 1621 and 8309 elements respectively.

Finite elements

In the numerical model the crack is initially simulated by discrete interface elements. In Section 6.3 the choice is evaluated and discussed. The interface elements are placed at mid-span and span from notch end ($y = 48\text{mm}$) to the load plate ($y = 80\text{mm}$, $y = 120\text{mm}$ for the AZ_45_120 series). Two types of finite elements are used in the model: plane stress elements for the wood material and discrete interface elements to simulate the crack. The mesh is comprised of 2-dimensional 8-noded quadrilateral elements. The interface elements are 2-dimensional 3+3-noded interface elements and 2-dimensional 1+1-noded interface elements. In Tab. 6.2 the details of both finite elements are shown.

For the spruce end parts the mesh size is 10 mm. For the middle hardwood parts and the adjacent interface elements a mesh size of 1 mm is chosen. The small mesh size is chosen to properly simulate the crack propagation. A larger step size led to divergence for the samples which fracture in a more brittle manner. Note that not all spruce parts have an element size of 10 mm. To meet compatibility requirements at the interface of the spruce end parts and the middle hardwood part, the spruce end parts are smaller close to the interface, this is seen in Fig. 6.2. The mesh size of the support plates is also 10 mm.

In addition to the interface at mid-span which simulates the crack, there are two point interface elements and one additional line interface at the boundary between the middle hardwood part and the load support plate. Both the line and point interface represent the boundary between the load support plate and the test sample. Without the interface the support plate is fixed to the test sample and the support plate will act as an artificial re-

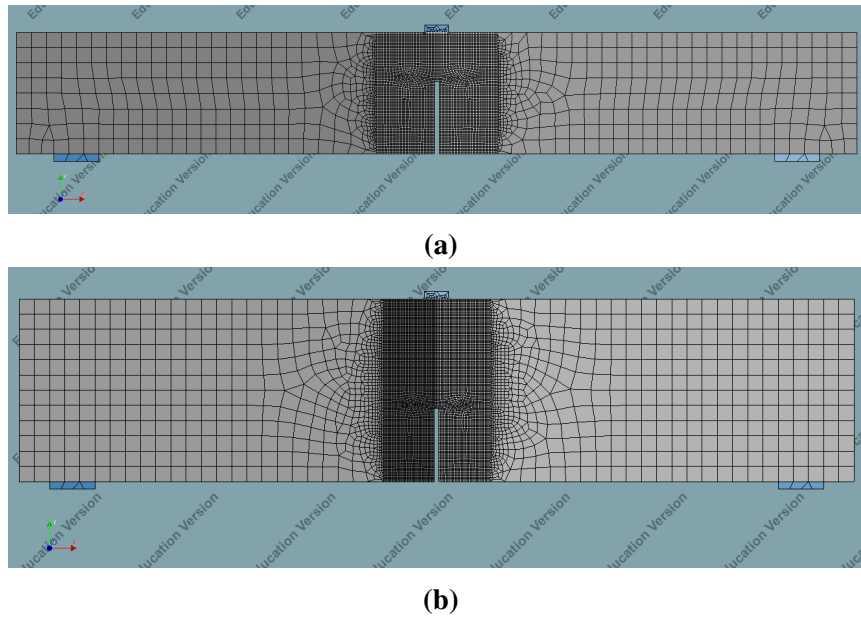


Figure 6.2: The finite element mesh of (a) the series with a height of 80 mm and (b) with a height of 120 mm.

inforcement to the test specimen. Thus the interface needs to be described between the support plate and the test sample. This is done by two point interface elements at the ends of the support plate and one line interface over the length of the support plate. In Fig. 6.3 the interface is shown. To prevent the artificial increase in stiffness, the stiffness of the line interface is equal to zero and the test sample can rotate separately from the support plate. The function of the two point interface elements is to transfer the load from the support plate to the test sample. The stiffness of the point interface elements is arbitrarily chosen at a high value. This way the test sample can fracture and separate completely and rotate around the support plate.

Material model

In Tab. 6.3 the linear elastic material properties are shown. For the steel support plates, the line and point interfaces at the boundary with the plates and the spruce end parts, only the linear elastic material properties are prescribed. For the middle hardwood part also the fracture properties are prescribed in Tab. 6.4. The value for the MoE perpendicular to the grain, the tensile strength and the fracture energy is determined in the experiment and retrieved from Tab. 5.8.

The other material properties in Tab. 6.3 are either based on the Eurocode (NEN-EN 338 (2016)) or on literature. The value for the MoE parallel to the grain (MoE_x) is from the Eurocode, where the assumed strength class for spruce, oak, bilinga and azobé is C30, D30, D50 and D70 respectively. The Poisson's ratio and the shear modulus is based on relations stated by Green et al. (1999). The Poisson's ratio is taken as the average of the μ_{LR} and the μ_{LT} value stated in Tab. 2.2. In the paper by Green et al. (1999) the Poisson's ratio for bilinga and azobé are not stated. It is assumed this value is equal to the value for oak, 0.40.

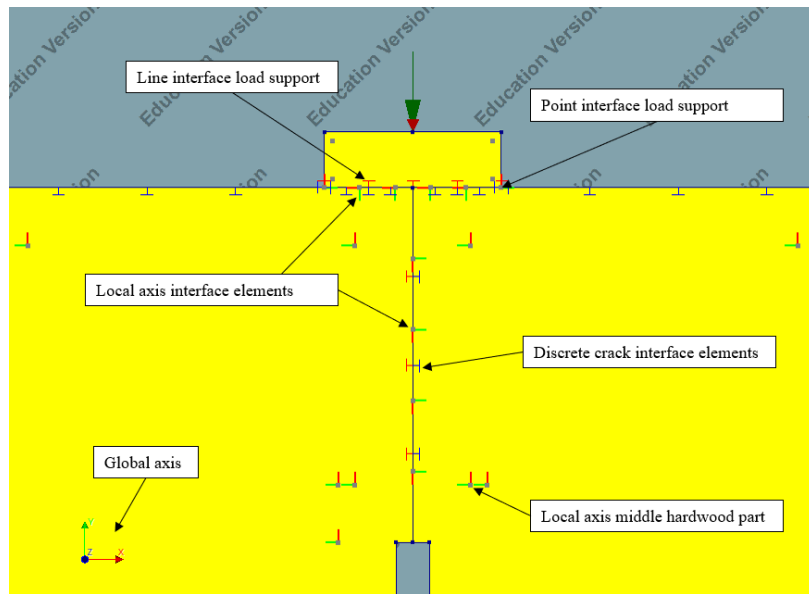


Figure 6.3: Detailed image of the area around the notch and interface elements. The image shows the location of the interface elements and the direction of the local axes.

The shear modulus is also based on relations stated in Green et al. (1999), where a ratio is given between the shear modulus and the MoE. For spruce this ratio is 0.12 and for oak 0.09. Thus for spruce the shear modulus is 0.12 times the MoE parallel to the grain and for oak, and the other hardwood species, 0.09 times the MoE parallel to the grain. Lastly, the initial assumed tension softening curve is a linear softening curve. Note that for the model of the AZ_45_120 series the same material model is used as the AZ_45_80 series.

Solution method

A structural nonlinear analysis is run with a prescribed displacement of 10 mm. The displacement is applied in different load steps to properly model the tension softening and the (quasi-)brittle behaviour post peak load. The displacement is applied in three load step blocks, shown in Tab. 6.5.

In the nonlinear analysis both physically and geometrically non-linearity is included. The maximum number of iterations is 100. For all analysis both displacement and force convergence norm is used. Both convergence tolerances are set at 0.01 and need to be met simultaneously. The iterative method used is a full Newton-Raphson incremental-iterative procedure, meaning the tangent stiffness matrix is updated in every iteration.

In the numerical model multiple mesh sizes and load steps are applied to study the convergence behaviour and the mesh-sensitivity. The convergence with changing mesh size had an influence on the series which showed very brittle and unstable cracking behaviour. With a mesh size larger than 1 mm, the analysis did not convergence due to the brittle material behaviour. For the less brittle series, such as the AZ_0_80 series, the mesh size had minor influence on the results and all analysis converged. Increasing the applied displacement step size to 0.1 mm (100 steps) and 0.5 mm (20 steps), led to less accurate results. Similar to the mesh size, the influence of this change was less significant for the

Table 6.3: Linear elastic material properties.

Element	Model	MoE _x (N/mm ²)	MoE _y (N/mm ²)	Poisson's ratio (-)	Shear modulus (N/mm ²)	Stiffness (N/mm ³)
Steel	Linear elastic isotropic	210000	210000	0.3	-	-
Load line interface	Interface element	-	-	-	-	0
Load point interface	Interface element	-	-	-	-	10 ⁵
Spruce	Linear elastic orthotropic	12000	400	0.44	1440	-
Oak	Linear elastic orthotropic	11000	1000	0.40	990	-
Bilinga	Linear elastic orthotropic	14000	1050	0.40	1260	-
Azobé (45°) ¹⁾	Linear elastic orthotropic	20000	2200	0.40	1800	-
Azobé (0°)	Linear elastic orthotropic	20000	1500	0.40	1800	-
Azobé (90°)	Linear elastic orthotropic	20000	2600	0.40	1800	-

¹⁾ Material model used for the AZ_45_80 and the AZ_45_120 series.

Table 6.4: Fracture properties.

Element	Cracking model	Tensile strength (N/mm ²)	Fracture energy (N/mm)	Tension softening curve
Spruce	Discrete cracking	3.5	0.250	Linear
Oak	Discrete cracking	9.7	0.542	Linear
Bilinga	Discrete cracking	4.2	0.490	Linear
Azobé (45°)	Discrete cracking	11.0	0.656	Linear
Azobé (0°)	Discrete cracking	5.0	1.110	Linear
Azobé (90°)	Discrete cracking	11.0	0.534	Linear
Azobé (h120)	Discrete cracking	10.0	1.119	Linear

¹⁾ At height 0 to 48 mm the length of the element is 38.5, this is due to the location of the initial notch.

Table 6.5: Load steps.

Load step block	Step size (mm)	Load steps	Total displacement (mm)
1	0.1	10	1.0
2	0.01	100	1.0
3	0.1	80	8.0
<i>Total</i>			10.0

less brittle series. The reason that the mesh size and load step size had less influence on the results of the less brittle materials, is that the crack along the interface elements development more gradual due to the higher fracture energy value. A detailed evaluation of the mesh-sensitivity and convergence behaviour of the model along with figures of the load-displacement curve, are shown in Appendix D.

6.2.2. Numerical results

For each series the same analysis is run with the finite element model stated in Section 6.2.1. In Fig. 6.4 the load-displacement curve of the numerical analysis is shown along with the load-displacement curve of the experiments. In the curve the moment during the fracture process is shown where: (A) the tensile strength is reached at the end of the notch, (B) the peak load is reached, (C) the traction-free crack is initiated at the notch end and (D) complete fracture of the specimen takes place. The load levels for the experimental results are not shown in the figure. From the DIC files it is hard to distinguish the exact points when the tensile strength is reached or when the traction-free crack is formed.

Most of the numerical load-displacement curves show a high resemblance with the experimental results. For the linear elastic stiffness and the peak load this is expected as the MoE and the tensile strength are derived by comparing the load-displacement curve of both analysis. The post-peak curve is mainly defined by the fracture energy and the shape of the tension softening curve. From Fig. 6.4 it can be seen that the load-displacement curve of the experimental and numerical results of the SP_45_80, OA_45_80, AZ_45_80 and AZ_90_80 series are very similar. For the other series (BI_45_80, AZ_0_80 and AZ_45_120) the load-displacement curve of both analysis is different. Especially in the shape of the post-peak curve there is a large difference.

In Fig. 6.5 the crack tip opening displacement (CTOD), i.e. the crack width, at the notch end is shown during the fracture process. Only the CTOD is shown for a vertical displacement up to 3 mm. A traction-free crack is formed in the node after load level (C) is reached. After this point the CTOD increases linearly with the vertical displacement. The CTOD figure demonstrates the brittleness of the series and the size of the cohesive zone. Recall that load level (A) is the moment the tensile strength is reached and load level (C) the moment the crack forms. A large difference in vertical displacement between load levels (A) and (C) is the result of a large value for the fracture energy and thus a slowly developing crack. On the opposite, if load levels (A) and (C) are relatively close, the crack

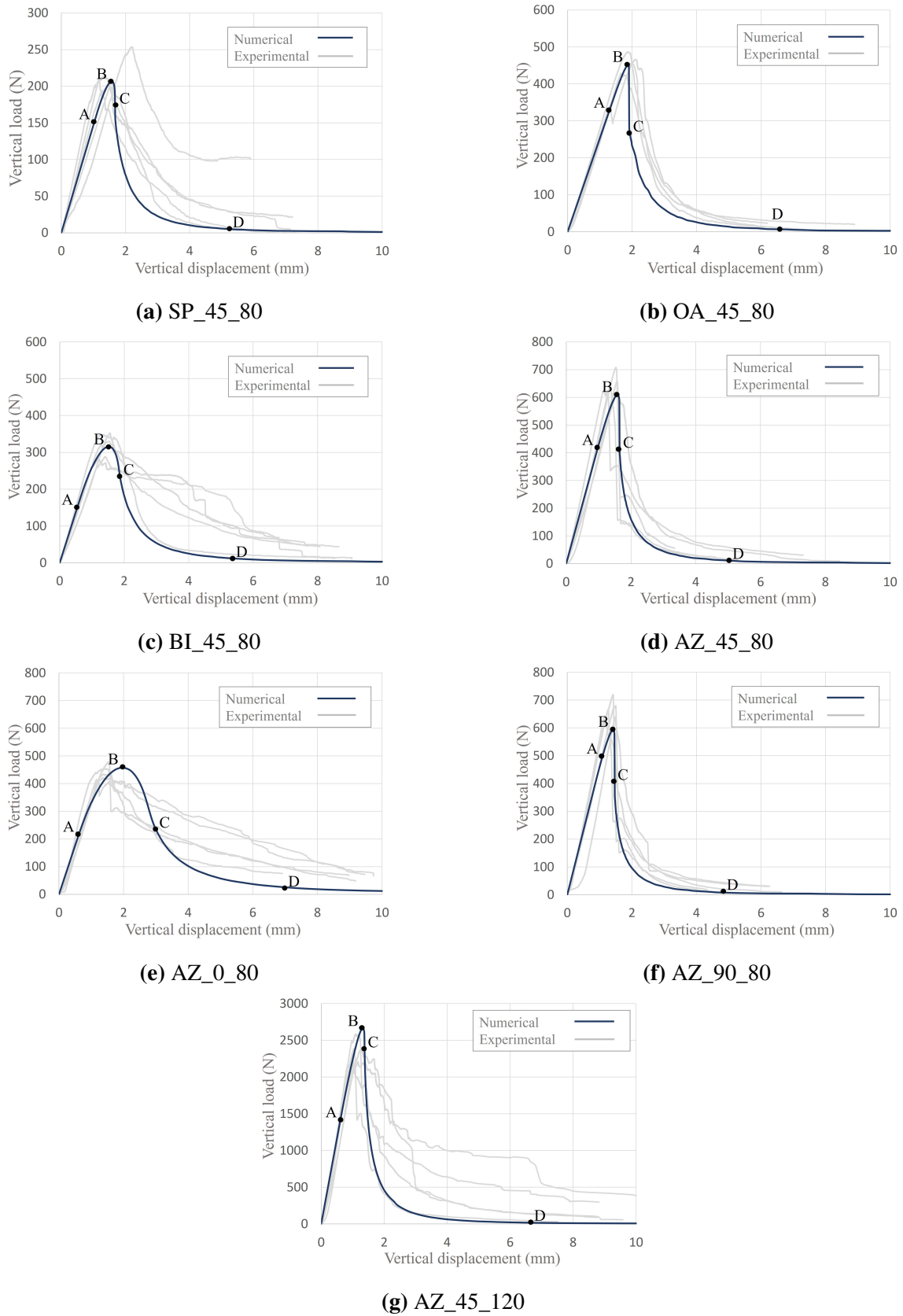


Figure 6.4: Load-displacement curve of the numerical models of each series.

forms in a more brittle manner. This is also demonstrated by a sudden increase in CTOD between load levels (B) and (C). This sudden increase demonstrates brittle failure after the peak load has been reached (load level (B)).

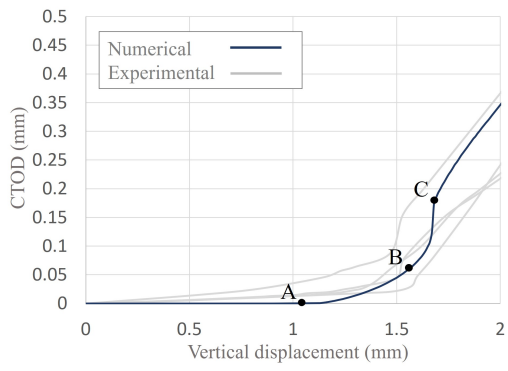
There are some notable differences in the CTOD plots between the experimental and the numerical results. Similar to the load-displacement curves in Fig. 6.4 there is a significant difference between the series with brittle/unstable fracture and the series with a slowly developing post-peak branch. From the CTOD curve it can clearly be seen that fracture develops much more gradually for the bilinga (Fig. 6.5c) and the azobé-0 series (Fig. 6.5e). This is indicated by the moment of tensile strength being reached and the moment a traction-free crack forms, load levels (A) and (C) respectively. For the BI_45_80 and AZ_0_80 series the vertical displacement between points (A) and (C) is more than for the other series. Moreover, the vertical displacement for these series at the onset of reaching the tensile strength, is lower than for the other series.

Most of the experimental results show a kink in the CTOD-displacement curve. This is the moment the traction in the material point has reached zero and a crack forms, hence the sudden increase in the CTOD. The CTOD has reached the critical value w_c (Fig. 2.12). This point coincides with load level (C) in the numerical model. Not all numerical models accurately predict this moment in the loading process. This is a critical point because at this load level crack propagation is initiated. Although the CTOD-displacement curves of the experimental and numerical results of the OA_45_80, BI_45_80, AZ_0_80 and AZ_45_120 series are comparable, the moment at which cracking is initiated is less accurately captured. For the other series (SP_45_80, AZ_45_80 and AZ_90_80) the moment cracking is initiated is approximately at the same vertical displacement for the experimental and numerical results.

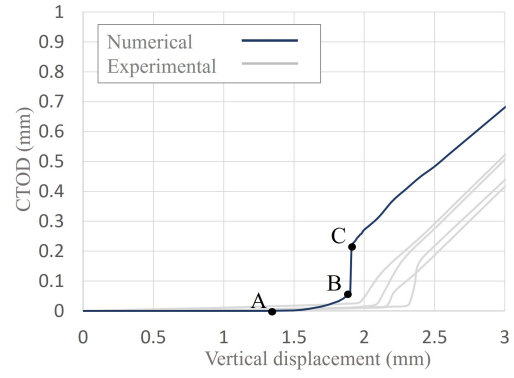
6.3. Numerical model calibration

6.3.1. Key findings

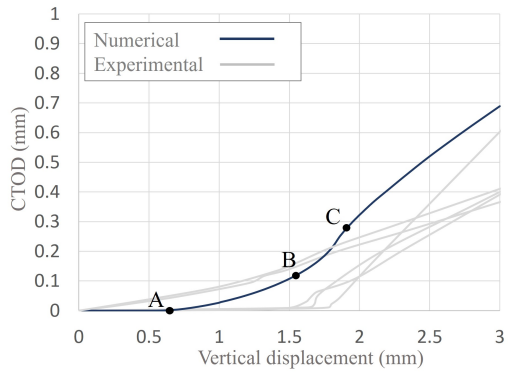
- The numerically obtained load-displacement curve of the SP_45_80, OA_45_80, AZ_45_80 and the AZ_90_80 series is similar to the load-displacement curve of the experiments.
- The numerically obtained load-displacement curve of the BI_45_80, AZ_0_80 and AZ_45_120 series deviates from the load-displacement curve of the experiments.
- Cracking develops at a relatively lower rate for the BI_45_80 and the AZ_0_80 series than for the other series.
- For the BI_45_80, AZ_0_80 and AZ_45_120 series there is a significant difference in vertical displacement between the moment the tensile strength is reached, load level (A), and the peak load, load level (B).



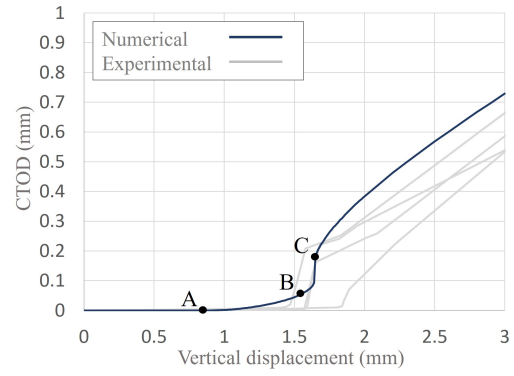
(a) SP_45_80



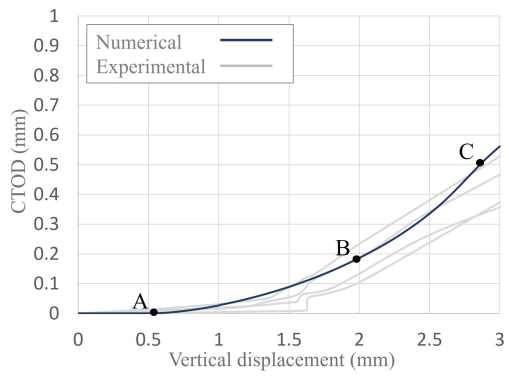
(b) OA_45_80



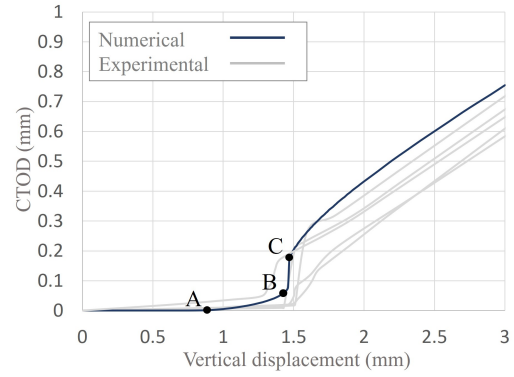
(c) BI_45_80



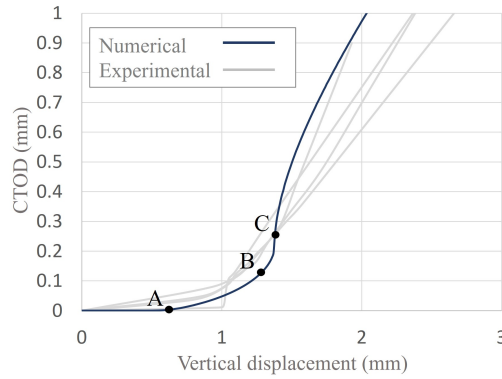
(d) AZ_45_80



(e) AZ_0_80



(f) AZ_90_80



(g) AZ_45_120

Figure 6.5: The crack tip opening displacement (CTOD) at the notch end during the loading process.

6.3.2. Discussion numerical results

Most of the key findings can again be explained by the orientation of the specimen. For all models a linear shape of the tension softening curve is implemented. The shape of the tension softening curve and the fracture energy are the main factors defining the shape of the post-peak load-displacement curve. An argument can thus be given that a linear tension softening curve is not the ideal shape for the series where the post-peak load-displacement curve of the experimental and numerical results do not coincide, the BI_45_80, AZ_0_80 and AZ_45_120 series. This is supported by the CTOD-displacement curves of these series. Although the CTOD during the fracture process is not very different between the experimental and the numerical results, the shape of the CTOD curve is very different.

For spruce, oak and azobé in 45 and 90 degrees, the load-displacement curve and the CTOD curve are mostly similar. Only the sudden drop in stiffness and the jump in CTOD for oak is higher in the numerical model than what is seen in the experiments. The linear tension softening curve is thus a good initial assumption of the real softening behaviour of these wood species/orientations. The accuracy of the linear tension softening curve for the various series can be explained by the presence of the non-linear phenomena micro-cracking and fiber-bridging (Fig. 4.10).

In Section 2.1.3 the applicability of various shape of the tension softening curve to wood is explained. According to Stanzi-Tschegg et al. (1995) the presence of non-linear phenomena in wood imply that a bi-linear tension softening curve is more applicable to wood than a linear softening curve. In Section 6.3.3 it is explained that the non-linear phenomena in the BI_45_80, AZ_0_80 and AZ_45_120 series is much more pronounced. Thus a bi-linear tension softening curve is better suited for these series than the other series. For the other series the linear tension softening curve is sufficient due to the lack of non-linear phenomena occurring during fracture.

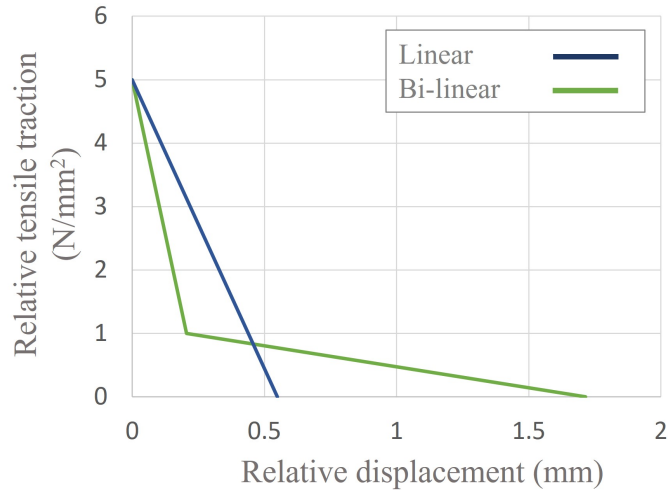


Figure 6.6: Constitutive law with the material properties of the AZ_0_80 series with a linear and a bi-linear tension softening curve.

6.3.3. Model calibration

Fig. 6.4 and 6.5 show that the initial numerical model with discrete cracking, the material properties found in the experiment and the assumption of a linear tension softening curve yields good numerical results for the SP_45_80, OA_45_80, AZ_45_80 and AZ_90_80 series. Fig. 6.4 and 6.5 show that for the other series (BI_45_80, AZ_0_80 and AZ_45_120) the initial numerical model does not provide accurate results compared to the experiments. This could be the result of three factors: (1) the wrong choice of tension softening model, (2) a bad estimation of the material properties or (3) the wrong choice of cracking model. In this section, the influence of these factors are discussed and a suggestions for adjustments to the numerical model are provided.

Use of the bi-linear tension softening law

In Section 6.3.2 it is mentioned that due to non-linear phenomena in wood, a bi-linear tension softening law is more applicable in the numerical model. Fig. 6.6 shows the difference between a linear and a bi-linear tension softening curve. For the two softening curves in Fig. 6.6 the tensile strength and the fracture energy is the same.

For the BI_45_80, AZ_0_80 and AZ_45_120 series these non-linear phenomena are more pronounced than for the other series, and therefore a bi-linear tension softening law is used instead of a linear softening law. In the new material model the bi-linear approximation from Bostrom (1992) is adopted. Where the stress at the break point is at $0.2f_t$ and the displacement $0.12w_c$. The tensile strength and fracture energy remain unchanged. In the figures, only load level (C) is indicated. Load levels (A) and (D) remain unchanged due to the adjustment in tension softening curve, and load level (B), the peak load, is clearly visible in the graph. The exact displacement for each load level is shown in Appendix C.

The load-displacement curves in Fig. 6.7 show a clear difference in the post-peak behaviour between the linear and the bi-linear tension softening curve. The change in slope

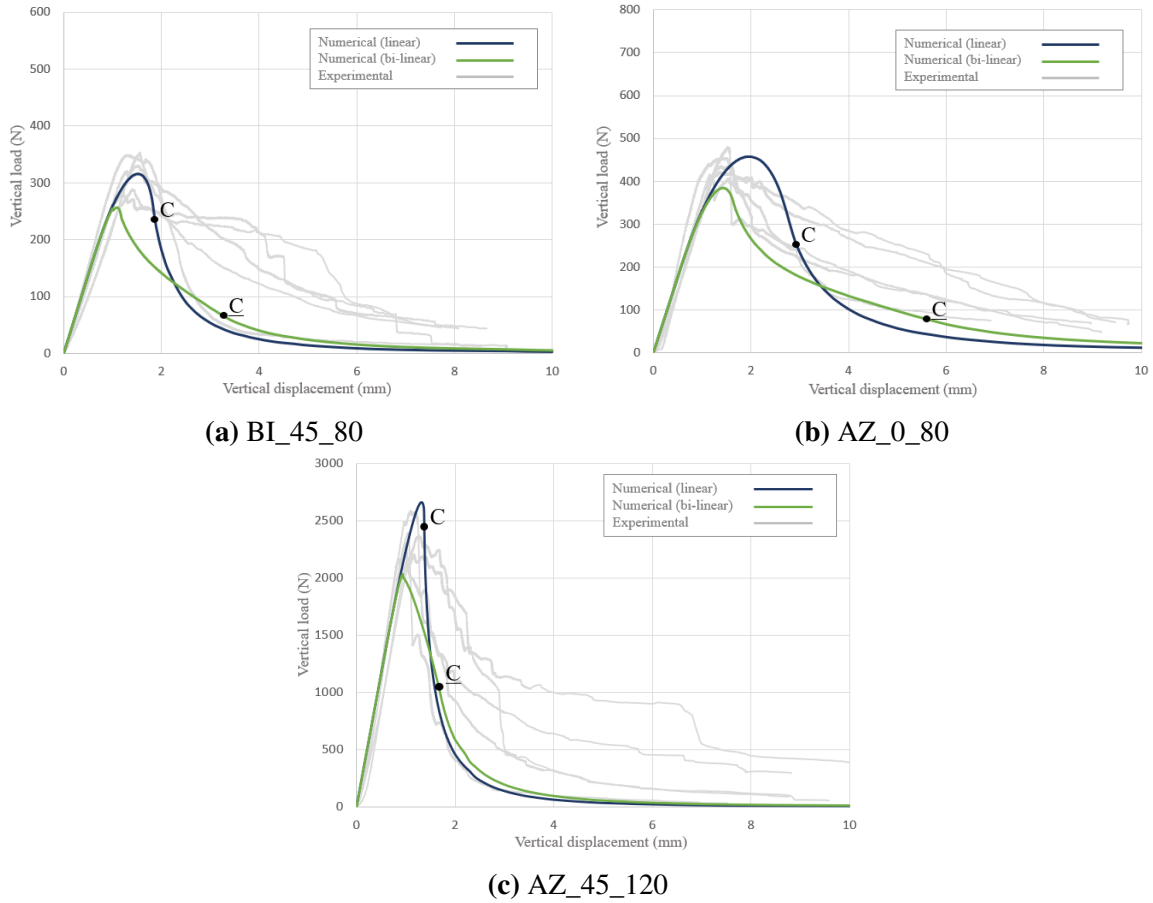
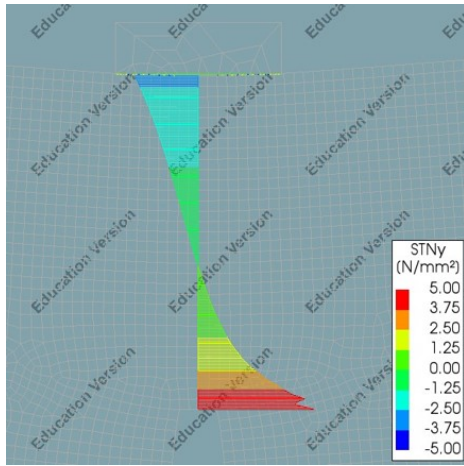


Figure 6.7: Load-displacement curve for the experimental results and the numerical models, with the linear tension softening curve and the bi-linear tension softening curve.

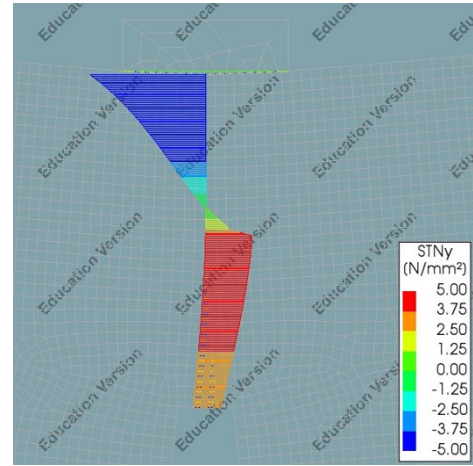
of the load-displacement curve is lower with a bi-linear tension softening curve. This is due to the part in the bi-linear curve that represents fiber bridging, see Fig. 4.10. The distribution of the fracture energy in the bi-linear curve results in a significantly higher value for the critical crack opening displacement w_c . To compare, the critical value w_c for bilinea in the linear softening model is 0.23 mm and for a bi-linear softening model 0.73 mm. As a consequence, the material point reaches complete fracture at a much later stage in the fracture process resulting in a more gradual decline in the post-peak stiffness. This is also indicated by the shift in load level (C). For all three series the moment cracking is initiated in the bi-linear model, indicated by (C), is at a higher vertical displacement than in the linear model.

Recall that the fracture energy is defined by the area under the stress-crack opening curve for a material point (Eq. 2.7) and by the area under the load-displacement curve (Eq. 2.9). The fracture energy remains unchanged, thus both area values must remain this same. This explains the drop in the peak load for the bi-linear model. Due to the longer tail in the bi-linear tension softening curve (Fig. 6.6), the first part representing micro-cracking is much steeper than for the linear case.

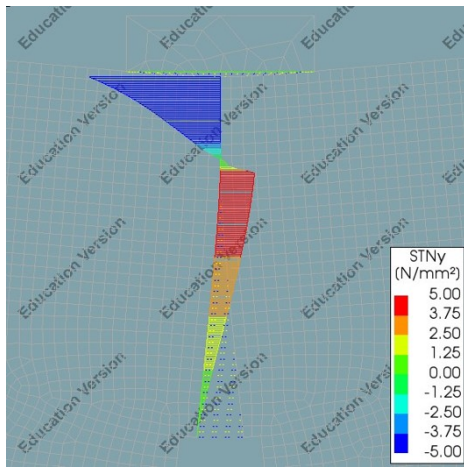
Although the peak load drops significantly when using a bi-linear tension softening



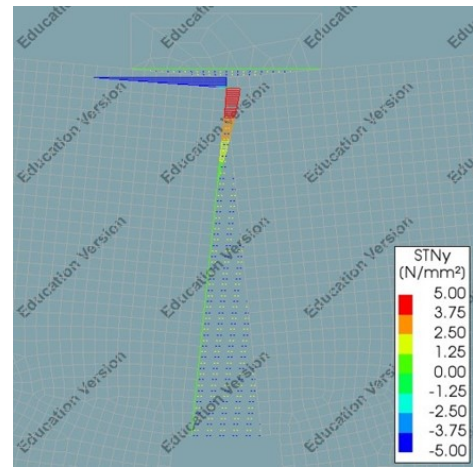
(a) Vertical displacement: 0.50 mm (A)



(b) Vertical displacement: 2.00 mm (B)



(c) Vertical displacement: 2.80 mm (C)

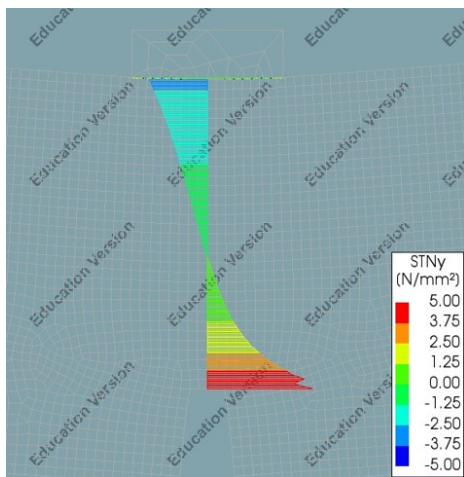


(d) Vertical displacement: 6.80 mm (D)

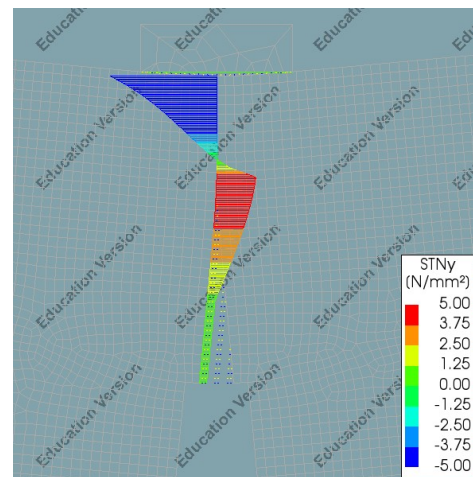
Figure 6.8: Line diagram of the horizontal traction (STNy) along the interface elements for multiple points throughout the loading process for the AZ_0_80 series with a linear tension softening curve.

model, the post-peak behaviour is better simulated than with a linear tension softening model due to the longer "tail" in the bi-linear softening model representing fiber-bridging. Note that the partition between micro-cracking and fiber bridging in the bi-linear model is not uniquely defined and the transition from one non-linear phenomena to the other is much more fluent in reality. The reason why the peak load is lower for a bi-linear tension softening curve is because the distribution of the total fracture energy is different. For a bi-linear tension softening curve the gradient of the traction-relative displacement curve is larger at the start of the fracture process, see Fig. 6.6. Meaning that the resistance to cracking is lower than for a linear curve. After the break-point in the bi-linear curve the gradient decreases, which means the resistance increases. This explains that at the later stage in the fracture process, the resistance is larger than for a linear curve. Thus with an equal fracture energy the energy dissipation is more gradual with a bi-linear curve than with a linear curve.

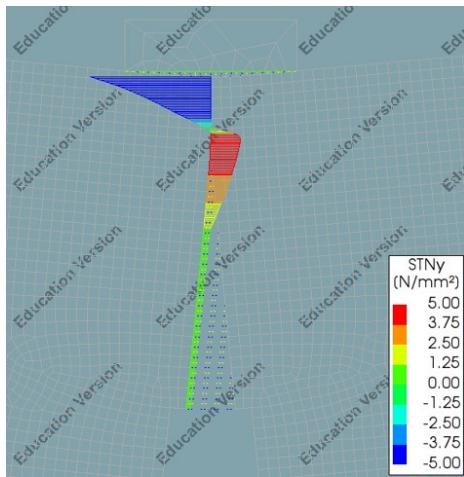
Fig. 6.8 shows the horizontal traction along the interface elements for the four load levels A through D as shown in Fig. 6.4e. The results are shown for the AZ_0_80 series with a linear tension softening curve. As a comparison, the horizontal traction is shown for the same series and same vertical displacements but with a bi-linear tension softening curve in Fig. 6.9. It can be seen that at the end of the linear-elastic stage, i.e. the tensile strength is reached at notch-end, the traction along the interface is the same. This is expected as only the constitutive law beyond the linear-elastic regime is changed. The big difference can be seen at a vertical displacement of 2.00 mm and 2.80 mm. With a bi-linear tension softening curve, the neutral axis is much higher at a vertical displacement of 2.00 mm, thus a smaller resistance to bending and a lower peak load.



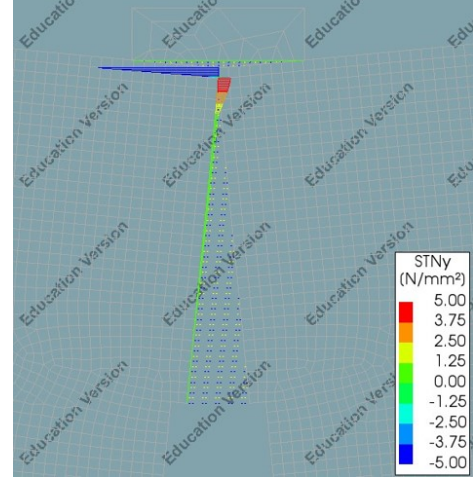
(a) Vertical displacement: 0.50 mm



(b) Vertical displacement: 2.00 mm



(c) Vertical displacement: 2.80 mm



(d) Vertical displacement: 6.80 mm

Figure 6.9: Line diagram of the horizontal traction (STNy) along the interface elements for multiple points throughout the loading process for the AZ_0_80 series with a bi-linear tension softening curve.

It is noteworthy that the load level (C) is at an unrealistically high value for the vertical displacement. Load level (C) is the moment the traction at the node at notch-end is zero,

meaning a traction-free crack is initiated. In the experiments the traction-free crack is initiated at notch-end at approximately 1.9, 1.8 and 1.0 mm for the BI_45_80, AZ_0_80 and AZ_45_120 series respectively. Fig. 6.7 and the displacement values for load level (C) in Appendix C, show that in the numerical model with a bi-linear curve this value is much higher, 3.2, 5.7 and 1.7 mm respectively. To conclude, although the load-displacement curve is better modelled with a bi-linear curve, the vertical displacement when a traction-free crack is formed is overestimated. A solution to this problem is to adjust the shape of the bi-linear curve. The bi-linear approximation by Bostrom (1992) thus needs to be adjusted so that the value for w_c is lower. Recall that w_c is the critical relative displacement, and thus the moment the traction is the material point is zero.

Adjusting the linear softening curve to a bi-linear softening curve for the other samples did not result in a more accurate model. Due to the high ratio between the tensile strength and the fracture energy (f_t/G_f), a change from linear to bi-linear is minor. Moreover, due to this change and the high tensile strength/fracture energy ratio, the initial slope of the bi-linear curve becomes too large which led to convergence issues for some samples, see Appendix D. Therefore, the tension softening curve for these samples remains linear. Only one exception is made for spruce, where the accuracy of the model increased when adjusting to a bi-linear curve.

Adjustment to the fracture energy

A second explanation for the inaccurate numerical model of the BI_45_80, AZ_0_80 and AZ_45_120 series is the incorrect use of the fracture energy value. As concluded in Section 4.4 and shown in Fig. 4.4, the cracked surface area of these series is much higher than the other series. The fracture energy is calculated with the exact cracked surface area measured by the profilometer. However, in the numerical model discrete interface elements are used to model the fracture surface. These discrete interface elements are placed at mid-span from the notch end to the top of the beam. Thus the cracked surface area of the numerical model is approximated by $b*(h-a_0)$. Thus for the series mentioned earlier, the difference between the approximated cracked area by the interface elements and the actual cracked surface area from the experiments lead to an inaccurate use of the input value for the fracture energy.

To account for the difference in cracked surface area, the input value for the fracture energy is adjusted. The initial input value for the fracture energy (Tab. 6.4) is adjusted according to the ratio between the approximated and the actual cracked surface area as shown in Tab. 5.2.

$$G_f^{\text{num}} = \frac{A_{\text{real}}}{A_{\text{approx}}} * G_f \quad (\text{N/mm}) \quad (6.1)$$

The adjustment to the real fracture energy value leads to a numerical fracture energy value G_f^{num} of 0.651, 1.372 and 1.502 N/mm for the BI_45_80, AZ_0_80 and AZ_45_120 series respectively. The other material properties remain unchanged, and the tension softening curve is bi-linear. This leads to the load-displacement curves shown in Fig. 6.10.

The shape of the tension softening curve remains unchanged, and thus the shape of the post-peak curve is the same. The only difference is that the total area under the load-displacement curve increases due to an increase in the input value for the fracture energy.

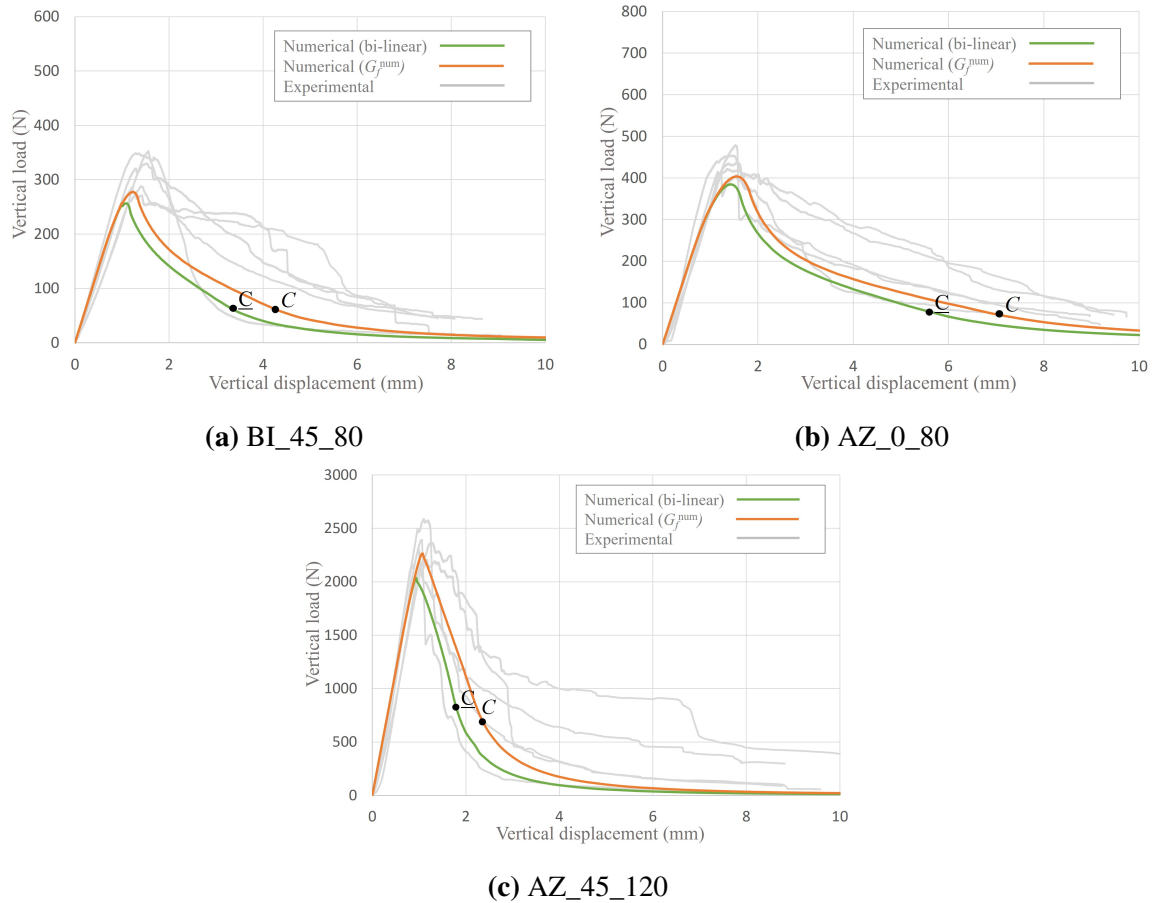


Figure 6.10: Load-displacement curve for the experimental results and the numerical models, with the linear tensions softening curve, the bi-linear tension softening curve and the model with the adjusted fracture energy.

As seen from Fig. 6.10 the results with the adjusted fracture energy is closer to the results from the experiments for all three series.

Change in the cracking model

A third solution to the inaccurate model is a change in the fracture model. In the initial numerical model discrete interface elements are used. In Section 2.3 a literature study is performed on the different fracture models which are used in practical applications. Each fracture model has its own advantages and drawbacks, and the choice of model is very problem-specific. As alluded to in the literature study there is no obvious integral approach to model fracture in wood. A choice is made for the discrete interface elements because the location of the crack is known with high certainty in this test setup. For the series which show almost brittle failure and have a relatively 2D dimensional crack plane this is the case, and the numerical model with discrete elements provide accurate results. For the series which do not fracture in a brittle manner and do not show a 2D crack plane, discrete interface elements does not properly model the crack. A choice here can be made for a

smearing cracking model or a continuum damage model (CDM). In a continuum fracture model, it is not required to model the assumed crack path a priori, the crack can form in any part of the material.

The three series are now modelled with a smeared cracking approach. The major difference is that the softening/fracture behaviour is now not described in the interface elements, but in the plane stress elements. Initially, the hardwood parts were modelled with a linear elastic orthotropic model. Now, the middle hardwood parts are described by an isotropic total strain based crack model. The discrete interface elements (at mid-span) are removed from the model. In the isotropic crack model the tensile behaviour is described by the material properties in Tab. 6.4, only now the tension softening curve is assumed to be bi-linear. Although crack propagation is not predefined in interface elements at mid-span, the increased value for the fracture energy according to Eq. 6.1 is used as the input value. The reason for this is that in the smeared cracking model the crack is still concentrated at mid-span. In Fig. 6.12 is seen how in the smeared cracking model the crack propagation does not deviate from mid-span. In the material model there is no reduction of the Poisson's ratio and the compressive behaviour is assumed to be elastic. The same bi-linear constitutive law is implemented as for the discrete model. In Fig. 6.12a the mesh around the notch for the smeared crack model is shown. Compared to the discrete model, the mesh size and element types are more important for crack propagation. No further research is done on the mesh sensitivity of the smeared crack model. In Fig. 6.11 the results of the smeared crack model are shown for the AZ_0_80 series. In both discrete and smeared models the same constitutive model is used with a bi-linear softening curve and an increase in the input value for the fracture energy to take into account the size of the fracture plane. Fig. 6.11 also shows the four load levels. The damage evolution and crack length for the smeared crack model is shown at these load levels in Fig. 6.12.

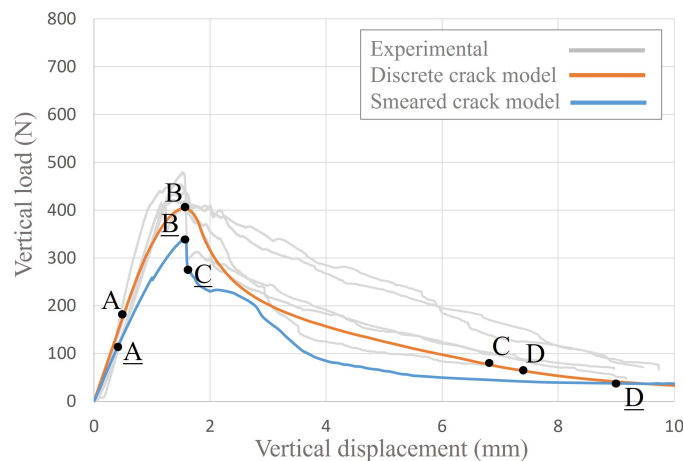


Figure 6.11: Load-displacement curve for the AZ_0_80 series with a discrete crack model and a smeared crack model.

There are some notable differences between the smeared cracking results and the discrete cracking results:

- The area under the load-displacement curve is smaller than for the discrete crack

model. This is due to the difference in modelling the middle hardwood part. In the discrete interface approach the hardwood material is modelled as linear elastic, whereas in the smeared cracking approach it is modelled non-linear.

- The load-displacement curve is less smooth than the discrete crack model curve. This difference can be explained by the formation of cracks at different parts of the structure. This also explains the lower peak load. Failure is distributed over the whole hardwood part instead of just the single discrete interface elements. In a discrete model only a single crack is formed at the discrete elements which results in a smooth development of the crack and thus a smooth load-displacement curve. The formation of multiple asymmetric cracks in the smeared model leads to sudden redistribution of stresses and a less smooth load-displacement curve.
- Cracking is initiated in the corner of the notch instead of exactly at mid-span. This is expected in a smeared cracking model as in the corner of the notch there is a stress concentration. This can also be explained by the location of load level A. Due to the stress concentration at the corner, the tensile strength is reached at an earlier stage than with a discrete model. The integration point closest to the corner of the notch enters the softening regime at load level A. This also explains why the stiffness prior to the peak load being reached is lower than for the discrete crack model. Due to minor asymmetry of the mesh around the notch, the crack will either develop on one corner of the notch or the other. The location of crack initiation remains unchanged when remeshing.
- Another difference is the required time for the numerical model to run. This difference should not be overlooked. The total elapsed time for the analysis to run for the AZ_0_80 series with a discrete fracture model is 356 seconds, and for the same series with a smeared fracture approach 922 seconds. This is an important argument in favor of the discrete cracking model. In design purposes the total computation time can be significantly important when large structures are modelled.

The differences stated above are visualised in the contour plots of the cracking pattern during loading. In Fig. 6.12 the cracking pattern is shown at the four load levels for the smeared cracking approach. To illustrate the cracking development in the smeared crack model, the largest principal strains are computed during the fracture process for the AZ_0_80 series. In the contour plots the applied scaling factor is 1.

From Fig. 6.11 and 6.12 can be concluded that the use of the isotropic smeared cracking model is not the solution to the inaccurate numerical model for the considered series. What this model lacks is the orthotropic fracture behaviour seen for the BI_45_80, AZ_0_80 and AZ_45_120 in the experiments. The top view of the fractured specimens, Fig. 4.5, shows that the crack develops very irregular and un-linear in the out-of-plane direction. In a two-dimensional model this out-of-plane fracture cannot be modelled. A final solution to these series is the use of a three-dimensional numerical model, where an orthotropic smeared cracking model is used instead of an isotropic smeared cracking model. In a three-dimensional model it is possible to fully describe the anisotropic properties of wood. As concluded before, the (fracture) characteristics of azobé in the T-direction are different

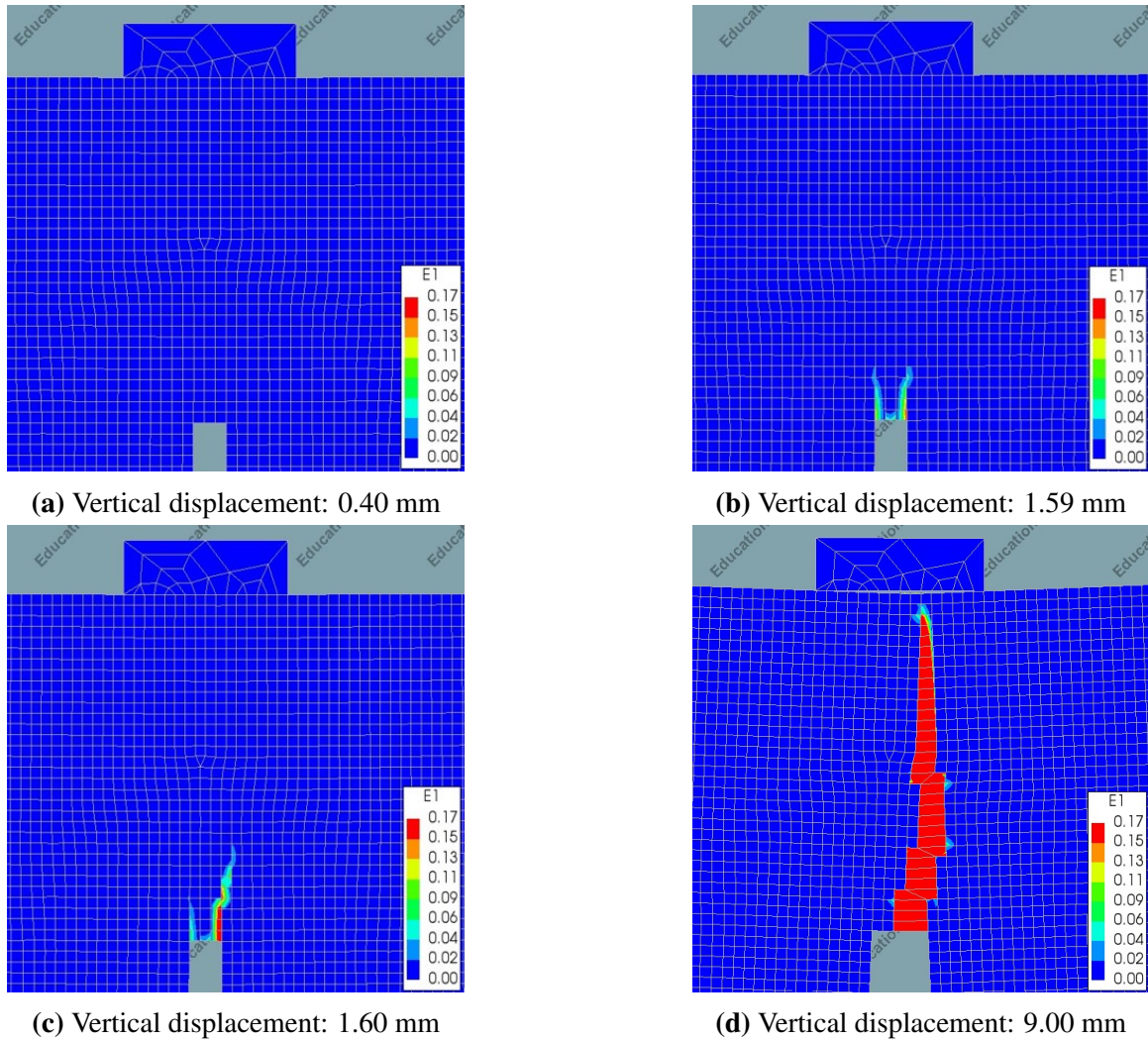


Figure 6.12: Contour plot of the highest principal strain (E1) for multiple points throughout the loading process for the AZ_0_80 series with a bi-linear tension softening curve and a smeared crack model.

from the R-direction. Thus to fully describe the anisotropic behaviour, the linear elastic properties and fracture properties must be prescribed in the three orthogonal directions. In DIANA it is not possible to implement an orthotropic smeared cracking model on solid elements. With a three-dimensional orthotropic smeared cracking model it would also be possible to model the fracture behaviour of sample with the orientation of the growth rings between the 0 and 90 degrees. This can be done by adjusting the direction of the local axis of the sample. But, it is expected that in a 3D numerical model, the crack plane will still be at mid-span and there the irregular 3D crack plane will not be modelled. A lattice model could provide realistic results but this requires too much computational time and storage and will not be useful in practical applications

The results of the numerical model of the other series (series: SP_45_80, OA_45_80, AZ_45_80 and AZ_90_80) showed a reasonable resemblance with the results from the experiment. Although these initial models are accurate enough, an additional calibration was performed with the adjusted fracture energy value according to Eq. 6.1 and a bi-linear tension softening curve. For the spruce (SP_45_80) series the softening curve is changed to bi-linear. For the other series only the adjusted fracture energy value is implemented. A change to a bi-linear curve for these series did not provide more accurate results. The calibration resulted in a unique constitutive law for each series, where depending on the amount of non-linear behaviour and a comparison with the experimental results, either a linear or bi-linear softening law is chosen. In Fig. 6.13 the constitutive laws are shown for each series.

6.4. Influence of the material properties on the numerical results

The fracture process in this research is quantified by four parameters: the modulus of elasticity, the tensile strength, the fracture energy and the shape of the tension softening curve. If these material properties are known, an accurate estimation of the fracture process can be made based on conclusions from this research. What for practical implications is important is how much these properties influence the fracture process and more importantly the peak load. In this section the correlation between the material properties and the peak load is studied. Each of the four aforementioned material properties are adjusted in the numerical model of the AZ_0_80 series. The material properties for AZ_0_80 as stated in Tab. 6.3 and 6.4 are multiplied by a factor 0.8, 1.2 and 1.5. For the shape of the tension softening curve a linear, bi-linear, Hordijk and JSCE softening curve is implemented. The Hordijk tension softening curve is similar to an exponential softening curve (see Fig. 2.9) and the JSCE softening curve is similar to a bi-linear softening curve only the break-point slightly differs.

Fig. 6.14 demonstrates how the peak load and post-peak behaviour changes when adjusting the input values for the material properties in the numerical model. The peak load is dependent on all material properties, of which the tensile strength is the most dominant. An increase in the tensile strength of 50% results in an increase in the peak load of 20%. Fig. 6.14d shows that the peak load is also significantly increased when a linear tension soften-

6.4. Influence of the material properties on the numerical results

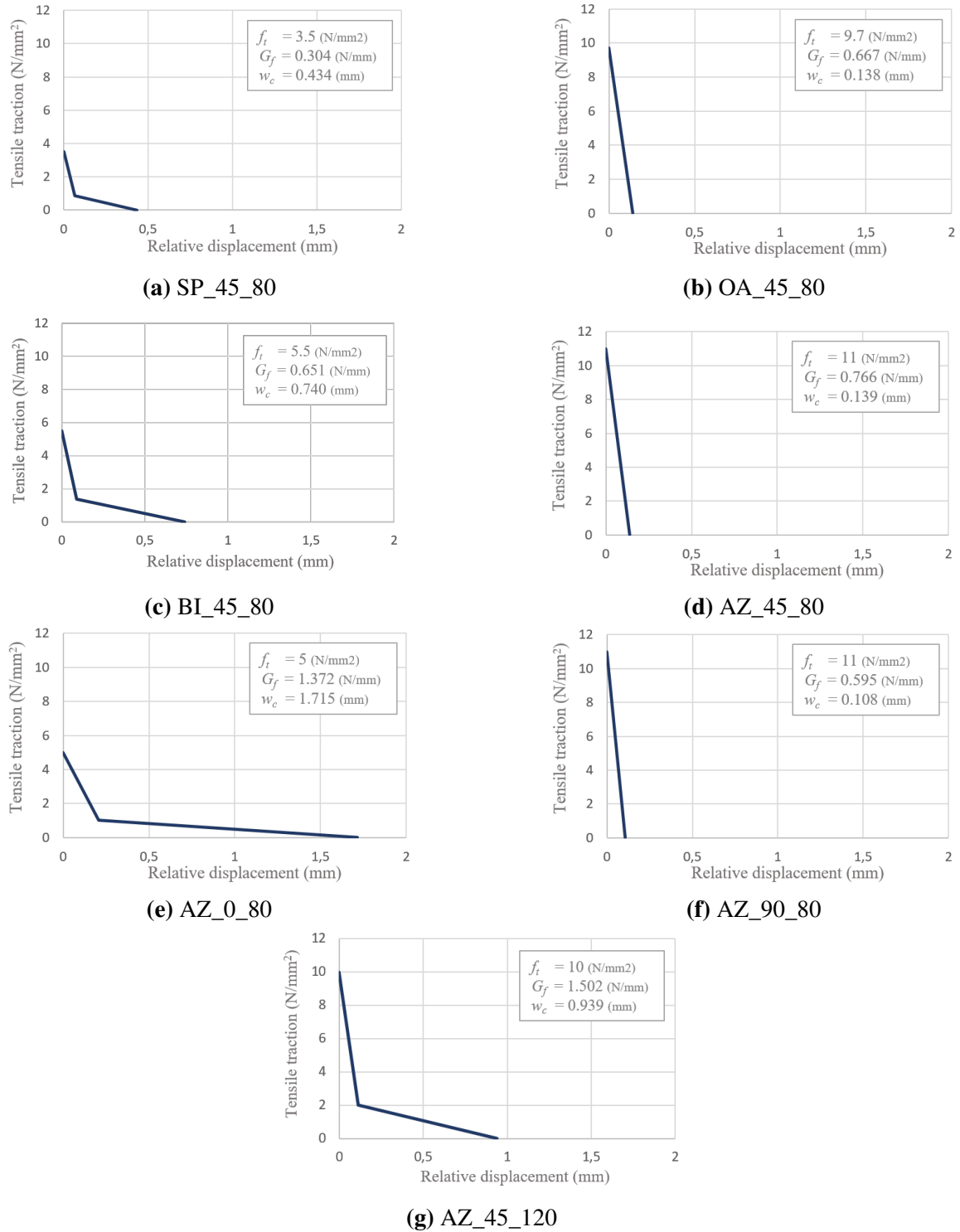


Figure 6.13: Constitutive law of the material model with the tensile strength found in the back-analysis and the adjusted fracture energy considering the cracked surface area.

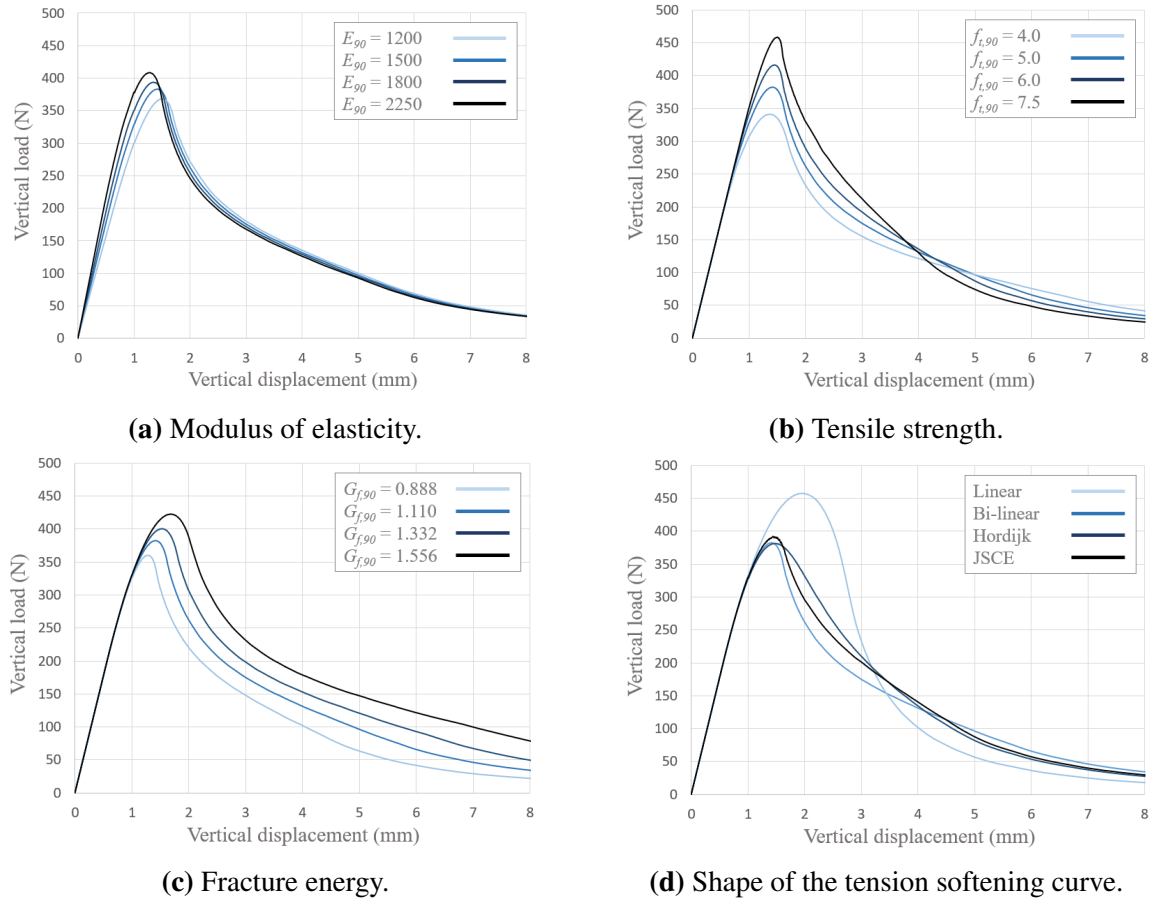


Figure 6.14: Load-displacement curve of the AZ_0_80 series showing the influence of the material properties on the general mechanical behaviour.

ing curve is implemented. The difference between the other shapes has minor influence on the mechanical behaviour. JSCE softening is a variant of the bi-linear curve presented in Section 2.1.3, but the break-point is at $(0.75G_f/f_t; 0.25f_t)$. The Hordijk tension softening curve is a non-linear curve similar to a exponential curve (DIANA FEA BV, 2017).

To verify the independence between the other material properties and the peak load, a similar parameter study is performed for the shear modulus, the MoE parallel to the grain for the middle azobé part and the MoE parallel to the grain for the spruce end parts. Increasing the input value for these three parameters by a factor 1.5 results in approximately 1% change in peak load. The influence of these parameters on the peak load can thus be assumed to be negligible.

Fig. 6.14d shows that the peak load is dependent on the shape of the softening curve. Recall that in Section 5.7.2 the tensile strength is estimated from a back-analysis where the peak load is evaluated. In this evaluation is the shape of the tension softening curve is linear. However, for the BI_45_80, AZ_0_80 and AZ_45_120 a bi-linear softening curve is more accurate. Thus the peak load decreases for these series when implementing a bi-linear curve, as can be seen in Fig. 6.7. With the adjusted value for the fracture energy, only the tensile strength of the bilinga series needs to be readjusted (Fig. 6.10). The new value for

the tensile strength is changed from 4.2 to 5.5 N/mm². For the other series an adjustment to the tensile strength will not lead to a significantly more accurate model.

6.5. Conclusion

The main goal of the numerical modelling is to provide an accurate model to simulate the mode-I fracture of tropical hardwood. An initial numerical model is computed with the material properties found in Chapter 5. Initially, discrete interface elements and a linear tension softening curve is implemented in the numerical model. This yielded different results. For the series which showed a relatively more brittle fracture behaviour and a two-dimensional flat crack plane, the use of discrete elements and linear tension softening showed results comparable to the experimental results. This is based on a comparison of the load-displacement curve and the CTOD curve. For the series which showed a relatively more ductile fracture development and had a more irregular fracture plane, the combination of discrete elements and a linear softening model did not provide accurate results. These series are the BI_45_80, AZ_0_80 and AZ_45_120 series.

The numerical model of these series are adjusted first by using a bi-linear tension softening curve instead of a linear curve. Literature states that a bi-linear tension softening curve is more suited for wood due to the formation of non-linear phenomena (Boström, 1992; Dourado et al., 2015). The larger the influence of non-linear phenomena the more accurate the fracture behaviour can be modelled with a bi-linear tension softening curve. In addition to the change in shape of the softening curve, the input value for the fracture energy is adjusted to account for the irregular three-dimensional crack plane. In a 2D model, it is assumed that the cracking plane does not change in thickness; this is contradictory with experimental evidence. To take this into account, the adjusted value for the fracture energy (Eq. 6.1) is considered.

A third modification to the numerical model is done by using a smeared cracking approach instead of a discrete cracking approach. Although a smeared cracking approach would be a better representation of reality as cracking can occur in any part of the specimen and propagate in any direction, the results show the opposite. The load-displacement curve of the smeared model does not coincide with the experiment results. Furthermore, similar to the discrete interface approach, cracking still occurs in a relatively straight manner regardless of the fracture energy or the shape of the tension softening curve. This irregular cracking is the result of the micro-structure of wood, and this can not be modelled with the simple numerical models here. A lattice model could best model this behaviour as here the micro-structure of wood can be modelled. However this is a very complicated and time-consuming model and is highly undesirable for practical applications. For practical applications a more suiting model would be an orthotropic smeared cracking model in a three-dimensional space, where unique fracture properties are described in each direction. The orientation of the growth rings can then be modelled by changing the direction of the local axis. A three-dimensional model however requires a lot of computational time and space which in practice is essential. Thus the discrete interface element approach is preferred and yields acceptable results in modelling the fracture process if the crack path is known a priori and only the resistance of the structure is required.

PRACTICAL IMPLICATIONS

The key findings of this research show that the fracture process of hardwood can vary greatly depending on the wood species and the orientation in which it is placed. In practical applications and the design of timber structural elements, this level of detail is often not considered and the exact orientation in which a structural member is placed is neglected. Furthermore, in design only the maximum design load on a member is important to avert any fracture in the structure. This chapter focuses on the practical implications of this research. In this chapter a theoretical approach is taken to find an analytical solution for the critical load, i.e. the load when cracking is initiated.

7.1. Theoretical energy release analysis

A theoretical approach is taken to the problem to predict the peak load with an analytical model. Analytical approaches are often desirable in practice when a numerical or experimental approach is not possible or too comprehensive. In the theoretical approach the total potential energy of the system is determined with linear-elastic theory and implemented in Eq. 2.9. The equation of the energy release is then evaluated at a critical value, the value for which crack propagation is initiated. According to the fracture criterion by Griffith (1921), crack propagation is critical when the energy release G is equal to the fracture energy $G_{f,I}$.

7.1.1. Linear-elastic analytical model

First, to set up an equation for the total potential energy of the system, the relation between the external load F and the vertical displacement u at mid-span has to be determined using linear-elastic theory. A similar approach is taken by Blaß and Sandhaas (2017) for a CT-specimen fracture test. The fundamental difference with their approach is in setting up the linear-elastic relation between the vertical displacement and the external load. Setting up the linear-elastic relation for this test setup is not so straight forward. The reason for this is the discontinuity in the section modulus due to the notch. Thereby the problem arises that the location of the neutral axis is not constant over the span of the beam. Fig. 4.2 shows how the location of the neutral axis changes around the notch. Due to the change in neutral axis the effective section modulus of the beam changes. Therefore, in order to set up the linear-elastic relation between displacement and load, the effective section modulus must

be known and thus the location of the neutral axis. The location of the neutral axis around the notch can be approximated by the left figure in Fig. 7.1.

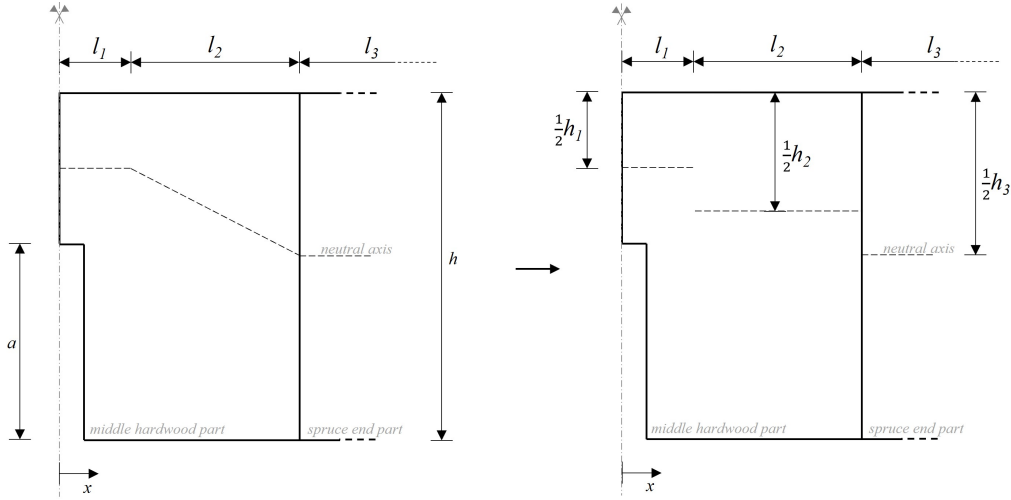


Figure 7.1: Effective height distribution over the length of the beam.

In order to apply linear-elastic beam theory, the beam has to be discretized in fields with each a constant bending stiffness EI . The effective section modulus is determined by evaluating the height of the compression zone in the beam. The reason for this, is that in contrast to the tension zone, the horizontal stress in the compression zone is linear over the height. Furthermore, the effective height of the transition zone (field 2) is linearly dependent on the distance from the notch, see Fig. 7.1. For simplicity sake, a constant effective height is assumed here. According to the numerical model the height of the fields as shown in Fig. 7.1 is stated in Eq. 7.1. All values are shown in mm. Note that this equation only holds for the hardwood species with a height of 80 mm.

$$\begin{aligned}
 h_1 &= h - a + 4 & 0 < x \leq 10 \\
 h_2 &= \frac{1}{2}(h + a) - 8 & 10 < x \leq 40 \\
 h_3 &= h & 40 < x \leq 240
 \end{aligned} \tag{7.1}$$

Where h is the total height of the beam, a is the length of the notch and $x = 0$ is located at mid-span. Eq. 7.1 only holds for the hardwood species with a height of 80 mm, because the changing neutral axis is dependent on the slenderness and depth of the beam. For the AZ_45_120 series, the influence of the notch on the stress distribution is less than for the smaller series. The numerical model of the AZ_45_120 series shows that the neutral axis does not change due to the notch, over the whole length of the middle hardwood part the neutral axis is located at a height of 80 mm. Thus in the analytical model for larger beam sizes a constant h can be assumed over the full length of the middle hardwood part. Future research is required to study the exact influence of the notch on the stress distribution in the beam.

Next, using linear-elastic beam theory the displacement and rotation of each field is computed. The mid-span displacement is computed by making use of a symmetry model

where the rotation at one end is equal to zero, and the force is divided by two. The total displacement is then computed by summing up the displacement at each end of the field and taking into account the contribution by the rotation of the fields. The vertical displacement at mid-span can be approximated by Eq. 7.2. In this equation it is assumed that the length of the fields as shown in Fig. 7.1 is $l/24$, $l/8$ and $5l/6$ for fields 1, 2 and 3 respectively. Furthermore, it is assumed here that the modulus of elasticity of the spruce end-parts is equal to 12000 N/mm^2 . Both the ratio's of the field length and the MoE for the spruce end-parts result in the constants between the brackets in Eq. 7.2.

$$u = \frac{Fl^3}{16E_{90}b} * \left(\frac{0.479}{(h-a+4)^3} + \frac{1.206}{(h-\frac{1}{2}a-6)^3} + \frac{0.000193E_{90}}{h^3} \right) \quad (\text{mm}) \quad (7.2)$$

Where, F is the force on the structure (N), l is the total length (mm) of the beam (assuming a symmetric beam), E_{90} is the Young's modulus (N/mm^2) of the middle part of the beam (N/mm^2), a is the length of the notch/crack (mm) and b the width of the beam (mm). In Fig. 7.2 the load-curves are shown for the hardwood series with a height of 80 mm. To compute the analytical load-displacement curve, first the vertical displacement is calculated at the average experimental peak load (Tab. 7.2). Then from the experimental results the crack length a is obtained for a certain value F along the post-peak load-displacement curve. This is done for multiple values of F . Then with a value for the load F and the corresponding crack length a , the vertical displacement is computed. This vertical displacement is added to the vertical displacement at the peak load to compute the descending branch of the load-displacement curve. The results are shown in Fig. 7.2.

The influence of the material properties in Eq. 7.2 is compared with the parameter study in Section 6.4. This is only done for the MoE perpendicular to the grain, as this is the only material property in the equation. The length of the crack a is assumed to be 48 mm, as this is the initial notch length, and the height of the beam h is 80 mm. The width b and span l are 40 and 480 mm respectively. Note that for the numerical model only a linear analysis is run.

Table 7.1: Comparison of the reaction force for a vertical displacement of 1 mm between the numerical and analytical model.

Modulus of elasticity perp. to the grain (N/mm^2)	Reaction force (N)	
	Numerical model	Analytical model
1200	313	341
1500	354	424
1800	389	506
2250	433	627

Tab. 7.1 shows that for larger MoE values, the analytical model loses its accuracy and overestimates the stiffness of the beam. Thus for larger MoE values the location of the

neutral axis changes and Eq. 7.1 loses its accuracy. Further research is required why this is the case and how the model could be improved.

7.1.2. Energy-based failure criterion

Now, to evaluate the critical load with the analytical model, a failure criterion is required. This can either be in the form of stress-based failure criterion with the tensile strength $f_{t,90}$, or by a energy-based approach with the fracture energy $G_{f,I}$. This research is mainly focused on an energy-based failure criterion, thus the failure criterion by Griffith (1921) is used here with the fracture energy as the critical parameter.

With the linear-elastic load-displacement relation the potential energy of the system is computed. Substituting the derivative of the potential energy in Eq. 2.9 and writing the equation gives the equation for the load as a function of the energy release, the modulus of elasticity and the geometry of the beam. To compute the critical load, i.e. the load when cracking is initiated, the value for the energy release G_I is substituted by the fracture energy $G_{f,I}$ for a given wood specie and orientation. In Appendix E the elaborated analysis and calculations are shown. In Eq. 7.3 the equation for the critical load is shown, where γ is a parameter containing the length of the crack and the location of the neutral axis.

$$F_c = \frac{2b\sqrt{\gamma l E_{90} G_{f,I}}}{\gamma l^2} \quad (\text{N}) \quad (7.3)$$

Where,

$$\gamma = \frac{1.437}{(h - a + 4)^4} + \frac{1.809}{(h - \frac{1}{2}a - 6)^4} \quad (\text{mm}) \quad (7.4)$$

Substituting the material properties of Tab. 5.8 results in the value for the critical external load F_c , yields to following results:

Table 7.2: Experimental and theoretical critical load for the series where Eq. 7.2 applies.

Series	Average experimental peak load (N)	Average experimental crack load (N)	Theoretical critical load (N)
OA_45_80	459	362	468
BI_45_80	321	242	456
AZ_45_80	651	525	778
AZ_0_80	448	398	836
AZ_90_80	670	556	733

There are some important limitations to the theoretical approach. In the theoretical analysis the critical load is determined based on the criterion that the energy release is equal to a critical value, the fracture energy in the case of linear-elasticity. This is the moment crack propagation is initiated. The theoretical critical load F_c should thus be compared

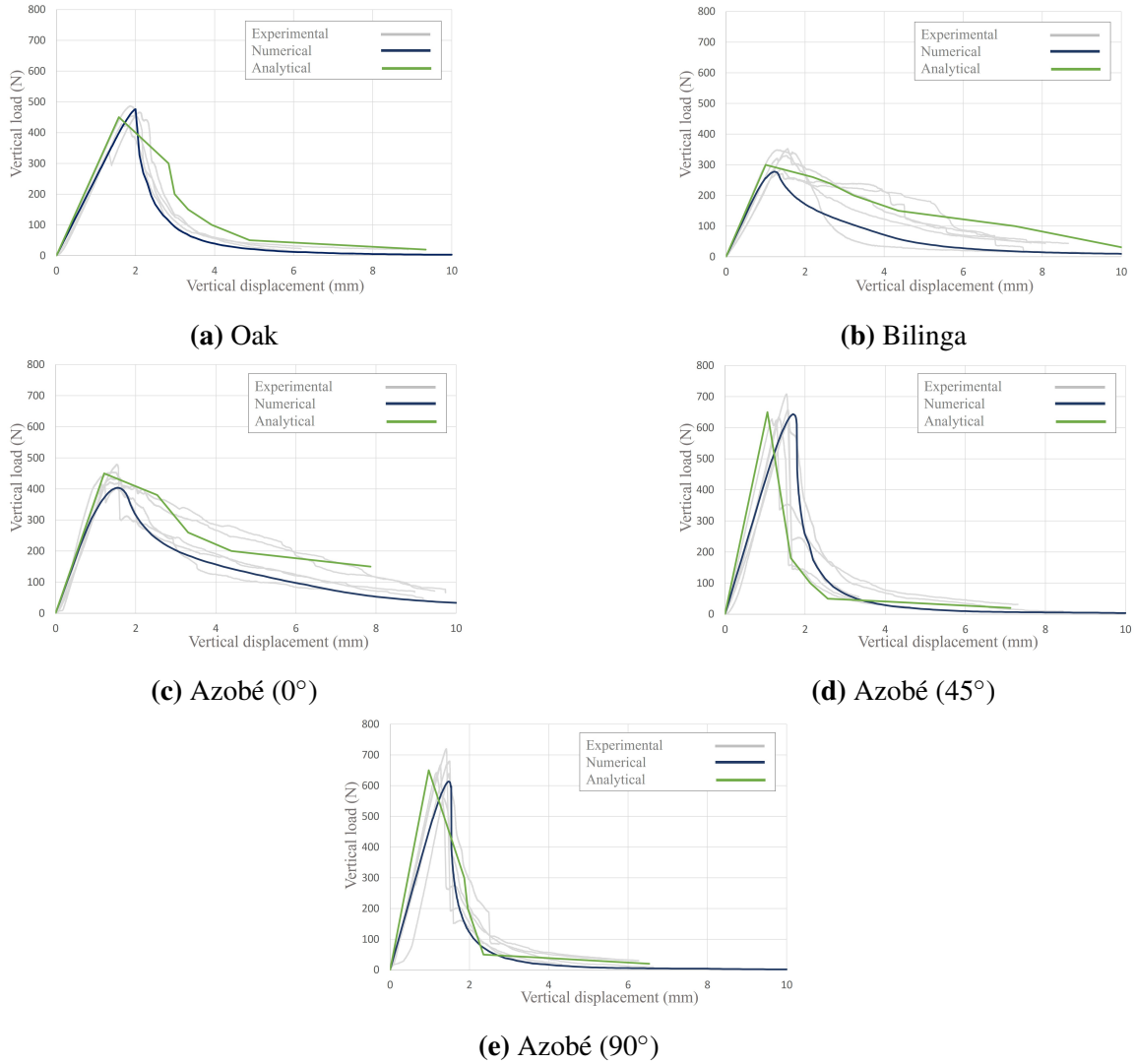


Figure 7.2: Load-displacement curve of the experimental results, the numerical model and the analytical model.

with the average experimental crack load. In Tab. 7.2 both the peak load and the load at the onset of cracking is shown, and it can be seen that there can be a significant difference. Thus the peak load can not be determined with the analysis. This requires an introduction of the tensile strength in the model, for the peak load is the result of the tensile strength and the fracture energy. This is also illustrated by the parameter study in Section 6.4. Fig. 6.14b shows that the tensile strength has a significant influence on the peak load and must therefore be included in the model. Another limitations is that the model loses its accuracy when the height of the specimen increases. This can be explained by the exclusion of the shear deformation. Lastly, the model assumes that all potential energy of the system is transferred to the formation of the crack, while in reality the applied work in the system is also transferred to strain energy, see Eq. 2.6. Thus the energy required to initiate cracking is overestimated in the current model.

7.2. Recommendations for design

In this research a relation is drawn between the microscopic structure of the wood specie and the mechanical behaviour. The key findings in Chapter 4 and 5 show how the mechanical behaviour and properties can be estimated from the microscopic structure of a wood specie. During the design of a wooden structure the level of detail of this research will not be reached. In the design of a structural element the moment of cracking is most important, not the cracking process. In Section 6.4 the influence of the material properties on this maximum load is studied. In this section a short recommendation is written to design a timber structural element. Emphasis is made here on how an arbitrarily chosen wood specie will behave and how the orientation of the growth rings can be taken into account.

What is concluded from the results of the experiments is that the material properties can vary significantly in different orientations. It was found that the fracture energy of azobé in the RL-orientation is 0.534 N/mm, while in the TL-orientation it is 1.110 N/mm. Also the stiffness and strength can vary depending on the orientation in which the structural element is placed. Careful attention must be paid to the points where fracture is critical in the perpendicular to the grain orientation, which are the re-entrant corners and notches in a structural element, see Fig. 1.2. Placing each structural element in the best possible orientation is a very difficult and time-consuming process. Moreover, most structural elements are either glulam (glue-laminated timber) or CLT (cross-laminated timber) elements, where each individual plank can be orientated in a different direction. It is therefore only recommended to pay close attention to the orientation of wooden planks at the location of the notch or hole. If at the location of the notch/hole the wooden plank is orientated in a less favorable position, additional preventive measurements for fracture must be applied.

Regarding the numerical model, close attention should be paid to the input values of the wood species. The estimations of the MoE and tensile strength perpendicular to the grain significantly differ from the values stated in the Eurocode. Changing the parameters of the Eurocode requires an elaborate study on the values which is a very time-consuming process and might take years. Furthermore, in the design models of buildings and bridges, usually only a linear elastic analysis is done. In Fig. 7.3 an example is shown of a linear-elastic orthotropic wood material model. No input parameters are shown in relation to fracture.

Although the fracture energy is not applicable in a linear-elastic material model, the difference in strength and stiffness of the different orientation can be taken into account in the model. If the critical cross-section in a structural element is placed in a certain orientation, e.g. with the growth rings orientated 90-degrees, the appropriate MoE and tensile strength value of this orientation are used in the material model. This requires a more elaborate and accurate study on the influence of the growth ring orientation on the mechanical properties.

In the construction industry there is a large variety of wood species which are used for timber structures. As concluded by this research each of these wood species behaves differently depending of the microscopic structure of the wood and the orientation in which it is placed. Focusing only on the mode-I tensile behaviour it can be seen that the quantity and orientation of the ray and parenchyma cells largely influence the resistance of the wood specie and the development of cracks in the material. Firstly, there is a large difference in

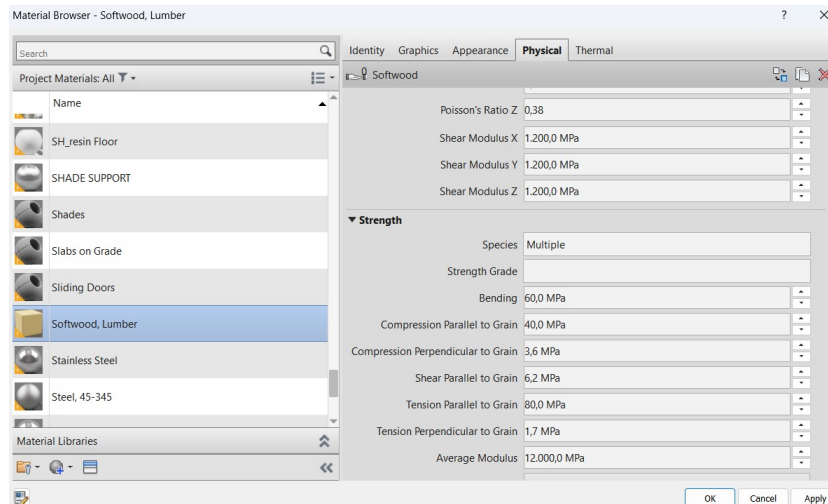


Figure 7.3: Example of a linear orthotropic softwood material model in Autodesk Revit 2023.

the mechanical properties between softwood and hardwood. Currently, most structures are built with softwood because it is widely available and cheaper than hardwood. However, as seen in this research and literature, the differences in strength can be large enough to consider the use of hardwood in certain situations.

CONCLUSION

8.1. Answer to the secondary research questions

- *Which material properties are relevant in modelling the fracture process?*

The fracture process in tension is modelled by a tension softening curve in the constitutive law. In the tension softening curve three parameters are relevant: (1) the tensile strength, (2) the fracture energy and (3) the shape of the softening curve. The tensile strength determines the onset of cracking, the fracture energy is the energy dissipated during crack propagation and the shape of the softening curve defines the distribution of energy dissipated during crack propagation.

- *Does the size of the tested sample have an influence on the test results?*

According to previous testing there is an increase in fracture energy with an increase in height, due to larger strain gradients (Larsen, 1990). This research shows a much larger increase in the fracture energy when the height of the sample is increased. This is due to invalid adjustments to the dimensions of the tested specimen. The dimensions of the beam are related to a parameter a as defined by Nordtest (1993). The defining parameter a is the height of the beam, and thus the length of the initial notch ($0.6a$) and span ($7a$) should be adjusted accordingly, which was not the case. Therefore, the results can not be compared and additional research is required.

- *Can the linear relation between the density and the fracture energy be expanded for hardwood?*

No, the linear relation by Larsen (1990) overestimates the fracture energy of wood above 700 kg/m^3 . A new linear relation is set up for the density and the fracture energy values found in this research. The new linear relation between the density and fracture energy is: $G_f = 0.0005\rho + 0.072$. The new linear relation yields a mean absolute error (MAE) of 0.079 with the test results, while the MAE for the linear relation by Larsen is 0.202. This relation is based on the fracture energy results for spruce, oak, bilinga and azobé with a height of 80 mm and a growth rings orientation of 45-degrees. Addition wood species need to be tested with the same test setup to verify the validity of this equation.

- *How do the results of this experiment relate to current numerical models of wood fracture?*

In practice, failure is often assessed by a linear-elastic stress analysis (a stress-based failure criterion) (Danielsson, 2013). In this research, failure or fracture is assessed with an energy-based approach, with the critical value the fracture energy. In a energy-based approach the input value for the fracture energy and choice for the softening curve is dependent on the wood species and orientation of the growth rings.

- *Can an analytical approach model the perpendicular to the grain fracture behaviour of wood accurately?*

In this research a theoretical approach is taken by constructing an analytical model of the SEN-TPB test, where an equation is set up for the load-displacement curve and the critical failure load. The analytical model provides accurate results for hardwood species with a height of 80 mm. The analytical model does not provide accurate results for spruce and for specimen with higher dimensions. The cause is that the location of the neutral axis is dependent on the size of the specimen and the considered wood species.

- *How do the results of this research influence the design considerations of timber structural elements?*

Results show that the maximum load is heavily influenced by the orientation of the growth rings. In practical applications, the input values for the material properties should be chosen accordingly, with the growth rings orientation in mind. If design loads do not meet the strength, additional preventive measures should be taken to prevent fracture. Currently, the Eurocode only distinguishes the parallel and perpendicular to the grain orientation. But, this research showed that the difference between the tangential and radial orientation (both perpendicular to the grain) must not be neglected for hardwood in an energy-based analysis. In the future more attention and research could be spend on how this difference varies depending on the wood specie. In general, hardwood research is very limited. In order for hardwood to increase its usage in practical applications, research on the material is required.

8.2. Answer to the main research question

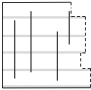
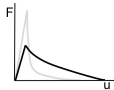
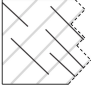
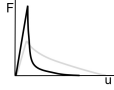
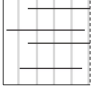
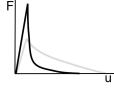
The goal of this research is to study which parameters influence the mode-I fracture properties of a tropical hardwood. In this thesis an experimental, numerical and analytical study is performed to answer the main research question:

- *Which parameters should be considered when describing the constitutive model of a (tropical) hardwood in mode-I tension?*

The quantitative and qualitative results of the experimental study demonstrate a significant dependency of the fracture behaviour on the tested wood specie and the orientation

in which the growth rings are orientated. Visual observations and the profilometer results revealed that there is an inconsistency in the roughness of the cracked surface area between the different series. From the microscopic analysis is concluded that this inconsistency in the roughness of the cracked surface area is the result of the amount of ray and parenchyma cells and in which direction they are orientated with respect to the fracture plane. In the perpendicular to the grain direction the rays provide an additional stiffness when loaded in tension. A second conclusion is that the parenchyma cells, which usually have a thinner cell wall than other cell types in wood, causes a weak link in the wood structure. The quantity and orientation of these wood cells has a significant influence on the fracture behaviour. This is clarified by Tab. 8.1 where the influence of the orientation on the general mechanical behaviour and material properties is shown. For each orientation, five samples were tested.

Table 8.1: Influence of the growth ring orientation on the fracture characteristics and properties of azobé.

Growth ring orientation	Microscopic structure ¹⁾	Load-displacement curve	Peak load (N)	Fracture energy (N/mm)	Modulus of elasticity (N/mm ²)	Tensile strength (N/mm ²)
0° orientation			448	1.110	1500	5.0
45° orientation			651	0.656	2200	11.0
90° orientation			670	0.534	2400	11.4

¹⁾ In the figures the rays are indicated by the dark grey lines, the parenchyma cells by the light grey lines and the fracture plane by the dashed lines.

The observations from the qualitative study are confirmed by the quantitative study. When the weaker parenchyma cells are orientated perpendicular to the crack plane (the 0° orientation), the non-linear phenomena micro-cracking and fiber-bridging are much more dominant. This causes more energy to be absorbed during the fracture process, hence a larger value for the fracture energy. Vice versa, if the parenchyma cells run parallel to the crack plane (the 90° orientation), the fracture process behaves in a more brittle manner which results in a lower value for the fracture energy and a larger decrease in stiffness in the post-peak regime.

In the second part of the thesis, the numerical model of wood is calibrated to fit the observations seen in the experiments. In the numerical model 2D discrete interface elements are used to model the fracture plane. By using a bi-linear tension softening curve more accurate results are obtained for the SP_45_80, BI_45_80, AZ_0_80 and AZ_45_120 series. The non-linear phenomena mentioned in the previous paragraph are accurately modelled by a bi-linear tension softening curve. The area under the softening curve is an adjusted input value for the fracture energy. This adjusted value is a multiplication of the real fracture energy value (Tab. 5.8) with a ratio which takes into account the roughness of the cracked surface area.

RECOMMENDATIONS

The results of this thesis provide new insights in the fracture process of tropical hardwood. But due to limitations in the research approach addition research is required. Recommendations for future studies are stated below:

Within the scope of this research

- The correlation between the fracture process and the orientation of the growth rings is studied for three different orientations of azobé. To fully understand this relation, more intermediate angles of the growth rings must be studied to understand the full correlation. Furthermore, the dependency of the growth ring orientation and the fracture process is only tested for azobé. No clear conclusions could be made on the dependency for other wood species. For future research a study only focused on the orientation of the sample could provide more clear conclusions regarding the influence of the orientation.
- Similar to the influence of the growth ring orientation, the size effect is only tested for two different sizes of the azobé samples. In future research, a more elaborate study on the size effect could provide a better insight into the topic. This study must include more variety in the height of the samples and more wood species which will be tested for size-effect. Furthermore, the dimensions of the specimen should be adjusted according to the parameter a as prescribed by Nordtest (1993). The parameter a corresponds to the height of the beam, and thus the span, dimensions of the middle hardwood part should be adjusted accordingly.
- In future research a more detailed analysis of the micro-structure of the wood species can provide more insight in the correlation with material properties.
- An important recommendation regarding the validity of the results, is to increase the number of samples in a series. Due to the wide spread in different series the sample size was only limited to five. An increase in sample size provides a more realistic average of the material properties and better arguments for comparison.
- During testing an adaptive displacement rate is used, meaning that the applied displacement rate is not constant throughout the fracture process. The displacement rate can influence the results due to a change in the strain and energy-release gradient.

The exact influence of the applied displacement rate on the results and the mechanical behaviour must be studied in future research.

- For a fair comparison between the discrete and the smeared cracking model, the interface elements must not be placed at mid-span but exactly at the corner of the notch. This is due to a stress concentration which arises at the corner.
- In this research the modulus of elasticity and the tensile strength were estimated with a back-analysis. For an accurate value of these properties, a separate analysis with a pure tension test is required. For future research an elaborate study and estimation of these properties in relation to the orientation and size effect could provide more insight into the mechanical behaviour of hardwood. The sensitivity study in Section 6.4 showed how the input values of the material properties change the mechanical behaviour. The back-analysis thus is not the most accurate approach to estimate the material properties.
- The numerical model was mainly focused on the use of discrete interface elements. The interface element model in this research is then calibrated and optimized to provide the most accurate results. Future research could be more focused on the use of other fracture model, such as the smeared cracking model and the continuum damage mechanics (CDM) model.
- Future research must be focused on optimizing the bi-linear curve tension softening curve. This research showed that, although the load-displacement curve is modelled accurately with a bi-linear curve, the moment of crack initiation is badly modelled by the currently used bi-linear model by Bostrom (1992).
- The analytical model could be further elaborated in future research. The model contains many assumptions regarding the stress redistribution around the notch, the energy balance in the system and the influence of other material properties. These factors/parameters need to be better understood to improve the analytical model. Furthermore, the tensile strength can be included based on its relation to other material properties.
- The approach taken in the analytical model is based on the change in potential energy of the system. Future research should also be focused on other approaches to an analytical solution. Ulfkjær and Krenk (1995) proposed an analytical model for crack propagation for concrete where the crack is modelled by the fictitious crack model in an elastic layer in the specimen. Cracking can also be modelled with a spring model, where the propagation of the crack is modelled with a non-linear spring, where the spring stiffness is described by the constitutive model of the wood specie.

Outside the scope of this research

- The intention of this research is to explore and study the mode-I fracture process of tropical hardwood. The dependency of the fracture process was measured with respect to three parameters: the wood species, the orientation of the growth rings

and the size of the sample. Fracture is a complicated and difficult part of a material to fully understand, especially in the case of an organic material as wood. There are thus more parameters involved in the characterisation of fracture beside the aforementioned three. Boerenveen (2019) tested the dependency of the fracture process on dry and wet samples. This research could be further elaborated by including the moisture content and other environmental parameters to the study.

- This research is limited to mode-I fracture. Additional research is required to see how the material behaves when shear is a dominant parameter. Is the same influence of orientation of growth rings seen in the fracture process and material properties in mode-II and mode-III fracture?
- Future research must be conducted on the relation between the observations and findings of this research with the structural design rules in the Eurocode. Current design rules are stress-based criteria. Could an energy-based approach, as done in this research, produce more accurate results?

REFERENCES

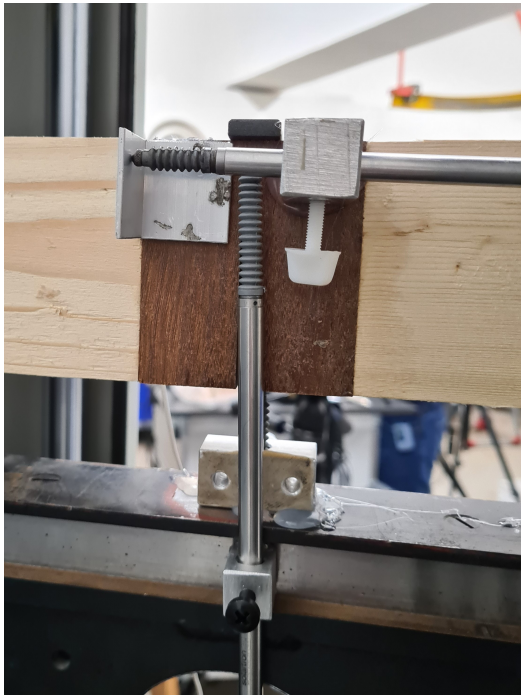
- Aicher, S. (2009). Process zone length and fracture energy of spruce wood in mode-I from size effect. *Wood and fiber science*, 42(2), 237–247.
- Bažant, Z., & Planas, J. (2019). *Fracture and size effect in concrete and other quasibrittle materials*. Routledge.
- Benabou, L., & Sun, Z. (2015). Numerical study of anisotropic failure in wood under large deformation. *Materials and Structures*, 48(6), 1977–1993.
- Berblom Dahl, K. (2009). Mechanical properties of clear wood from norway spruce. *Trondheim, Norway*.
- Blaauwendraad, J. (2006). Plate analysis, theory and application volume 1, theory. *Delft University of Technology, Delft*.
- Blaß, H., & Sandhaas, C. (2017). *Timber engineering: Principles for design*. KIT Scientific Publishing.
- Boerenveen, J. (2019). *Theoretical tenon beam shear strength* (Unpublished master's thesis). Delft University of Technology.
- Boström, L. (1992). Method for determination of the softening behaviour of wood and the applicability of a nonlinear fracture mechanics model. *Division of Building Materials, LTH, Lund University*.
- Carrington, H. (1923). Cv. the elastic constants of spruce. *The London, Edinburgh, and Dublin Philosophical Magazine and Journal of Science*, 45(269), 1055–1057.
- Danielsson, H. (2013). Perpendicular to grain fracture analysis of wooden structural elements-models and applications. *Division of Building Materials, LTH, Lund University*.
- DIANA FEA BV. (2017). User manual diana: 7.8.1 element types [Computer software manual].
- Dourado, N., et al. (2015). Wood fracture characterization under mode I loading using the three-point-bending test. experimental investigation of picea abies L. *International Journal of Fracture*, 194(1), 1–9.
- European Standard. (2003). *NEN-EN 408: Structural timber and glued laminated timber - determination of some physical and mechanical properties*.
- European Standard. (2008). *EN 1995-1-1: Eurocode 5: Design of timber structures - part 1-1: General - common rules and rules for buildings*.
- European Standard. (2012). *NEN-EN 1912: Structural timber - strength classes - assignment of visual grades and species*.
- European Standard. (2016). *NEN-EN 338: Structural timber - strength classes*.

- Fransen, G. (2016). *Behaviour of azobé (lophira alata) in compression perpendicular to grain* (Unpublished master's thesis). Eindhoven University of Technology.
- Gamstedt, K., Bader, T., & De Borst, K. (2012). Mixed numerical–experimental methods in wood micromechanics. *Wood Science and Technology*, 47.
- Gijzenberg, C. (2022). *Experimental and numerical modelling of mode I fracture in tropical hardwoods* (Unpublished master's thesis). Delft University of Technology.
- Green, D., Winandy, J., & Krestschmann, D. (1999). Mechanical properties of wood. *Wood handbook, US Department of Agriculture, Forest Service, Products Laboratory*, 4–1.
- Griffith, A. (1921). VI. The phenomena of rupture and flow in solids. *Philosophical transactions of the royal society of London. Series A, containing papers of a mathematical physical character*, 163–198.
- Gustafsson, P. (1988). A study of strength of notched beams. In *Proceedings of 21st meeting of cib-w18, parksville, canada, 1988* (Vol. 25).
- Hillerborg, A. (1978). *A model for fracture analysis*. Division of Building Materials, LTH, Lund University.
- Hillerborg, A. (1991). Application of the fictitious crack model to different types of materials. In *Current trends in concrete fracture research* (pp. 95–102). Springer.
- Kovryga, A., Stapel, P., & van de Kuilen, J. (2020). Mechanical properties and their interrelationships for medium-density european hardwoods, focusing on ash and beech. *Wood Material Science & Engineering*, 15(5), 289–302.
- Larsen, H. (1990). The fracture energy of wood in tension perpendicular to the grain: results from a joint testing project. In *CIB-W18 meeting 23* (pp. 294–531 (23-19-2)). Lisbon, Portugal.
- Leguillon, D., Martin, E., & Lafarie-Frenot, M.-C. (2015). Flexural vs. tensile strength in brittle materials. *Comptes Rendus Mécanique*, 343(4), 275–281.
- London, I. I. (1926). *Timbers from the gold coast*.
- Nordtest. (1993). *Fracture energy in tension perpendicular to the grain (nt build 422)* [Computer software manual].
- Pan, Z., Ma, R., Wang, D., & Chen, A. (2018). A review of lattice type model in fracture mechanics: theory, applications, and perspectives. *Engineering Fracture Mechanics*, 190, 382–409.
- Ravenshorst, G. (2015). *Species independent strength grading of structural timber*. Technische Universiteit Delft.
- Reiterer, A., Sinn, G., & Stanzl-Tschegg, S. (2002). Fracture characteristics of different wood species under mode I loading perpendicular to the grain. *Materials Science and Engineering: A*, 332, 29–36.
- Reiterer, A., & Tschegg, S. (2002). The influence of moisture content on the mode I fracture behaviour of sprucewood. *Journal of materials science*, 37, 4487–4491.
- Rots, J. G., & Blaauwendraad, J. (1989). Crack models for concrete, discrete or smeared? fixed, multi-directional or rotating? *HERON*, 34 (1), 1989.
- Sandhaas, C., Sarnaghi, A., & van de Kuilen, J. (2020). Numerical modelling of timber and timber joints: computational aspects. *Wood science and technology*, 54(1), 31–61.
- Schmidt, J., & Kaliske, M. (2009). Models for numerical failure analysis of wooden structures. *Engineering Structures*, 31(2), 571–579.

- Serrano, E. (n.d.). Retrieved from <https://portal.research.lu.se/en/persons/erik-serrano>
- Smith, I., Landis, E., & Gong, M. (2003). *Fracture and fatigue in wood*. John Wiley & Sons.
- Stanzl-Tschegg, S., Tan, D., & Tschegg, E. (1995). New splitting method for wood fracture characterization. *Wood science and Technology*, 29(1), 31–50.
- Ulfkjær, J., Krenk, S., & Brincker, R. (1995). Analytical model for fictitious crack propagation in concrete beams. *Journal of Engineering Mechanics*, 121(1), 7–15.
- Van Voorhis, S. (2016). Engineer and CNA dispute claim over dual 2014 bridge failures. *Engineering News-Record (ENR)*. Retrieved from <https://www.enr.com/articles/41092-engineer-and-cna-dispute-claim-over-dual-2014-bridge-failures>
- Vasić, S., Ceccotti, A., Smith, I., & Sandak, J. (2009). Deformation rates effects in softwoods: Crack dynamics with lattice fracture modelling. *Engineering fracture mechanics*, 76(9), 1231–1246.
- Vasic, S., Smith, I., & Landis, E. (2005). Finite element techniques and models for wood fracture mechanics. *Wood science and technology*, 39(1), 3–17.
- Wagenführ, R., & Scheiber, C. (2006). *Holzatlas*. Carl Hanser Verlag GmbH Co KG.
- Wittel, F. K., Dill-Langer, G., & Kröplin, B.-H. (2005). Modeling of damage evolution in soft-wood perpendicular to grain by means of a discrete element approach. *Computational Materials Science*, 32(3-4), 594–603.

RELIABILITY STUDY DIC

Prior to the SEN-TPB testing of the samples, the reliability and accuracy of the DIC is tested by comparing the results with a strain gauge. In this study the reliability of the DIC is evaluated by comparing the strain results of the DIC with results from a strain gauge and a LVDT. The comparison is done by determining the strain throughout the loading process 10 mm below the top of the beam, just right of the notch. In Fig. A.1 the location of the LVDT and the strain gauge is shown. The relevant LVDT is the horizontal LVDT in Fig. A.1a. Prior to the evaluation, the length of the LVDT is carefully measured to obtain strain values.



(a)



(b)

Figure A.1: Test setup of the reliability study of the DIC showing (a) the location of the horizontal LVDT and (b) the location of the strain gauge.

The comparison shows that the results of the LVDT are significantly different from the DIC and strain gauge. This is the results for a couple of reasons. Firstly, the LVDT

measures the displacement at the back of the sample, while the strain gauge and DIC are measured from the front. Secondly, the beam is subjected to a rigid body rotation around the point of loading due to cracking. As the LVDT is one-dimensional, and will thus not accurately measure the strains. Thirdly, in the determination of the strains, there is a minor error in measuring the length of the LVDT.

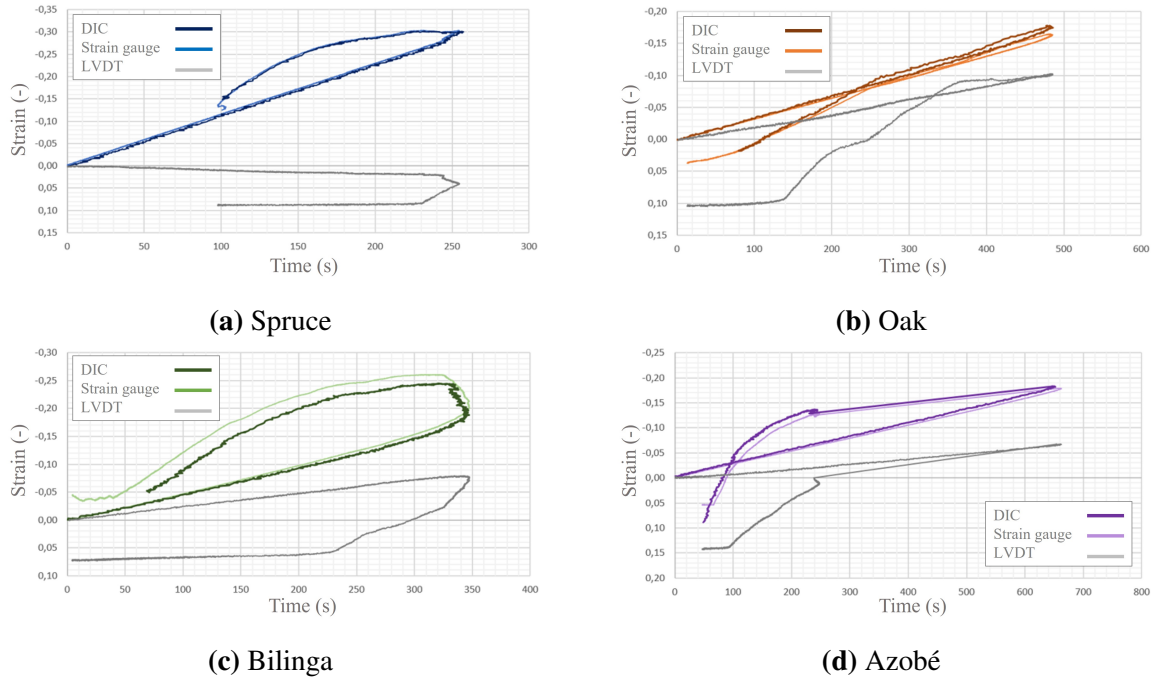


Figure A.2: Horizontal strain results during testing from the DIC, strain gauge and LVDT.

The results in Fig. A.2 show that the strain values obtained with the DIC are comparable to the strain gauge. For the DIC a testing volume is applied of $80 \times 60 \times 40 \times \text{mm}$, which yields an accuracy of 0.04 mm/m. The strain gauge, which can be considered the most accurate, has an accuracy of 0.003% or 0.0009 mm. Based on Fig. A.2 and the accuracy of the strain gauge, it can thus be concluded that the DIC provides accurate strain results.

DENSITY OF THE SAMPLES

Series	Sample nr.	l (mm)	b (mm)	h (mm)	V (mm ³)	W (g)	ρ (kg/m ³)
Spruce	2	41	30	23	28290	14.22	502.65
	3	40	32	22	28160	15.27	542.26
	4	40	31	23	28520	14.56	510.52
	5	40	39	23	35880	14.70	409.70
	<i>Average</i>						
Oak	1	40	36	23	33948	24.59	724.34
	2	40	33	23	30360	23.00	757.58
	3	40	37	24	35520	26.71	751.97
	4	40	32	24	31488	23.62	750.13
<i>Average</i>							746.00
Bilinga	1	40	35	24	33600	25.87	769.94
	2	40	41	24	39360	28.97	736.03
	3	40	36	24	34560	27.05	782.70
	4	40	36	23	33120	25.69	775.66
	5	40	38	24	36480	27.43	751.92
<i>Average</i>							763.25
Azobé (45)	1	40	36	19	27360	28.80	1052.63
	2	40	34	19	25840	27.60	1068.11
	3	40	38	18	27360	29.37	1073.46
	4	40	34	19	25840	28.07	1086.30
	5	40	40	18	28800	31.52	1094.44
<i>Average</i>							1074.99
Azobé (0)	6	40	31	19	23560	24.81	1053.06
	7	40	38	19	28880	29.35	1016.27
	8	40	34	18	24480	26.19	1069.85
	9	40	33	18	23760	25.10	1056.40
	10	40	36	18	25920	27.39	1056.71
<i>Average</i>							1050.46
Azobé (90)	11	40	37	18	26640	28.40	1066.07
	12	40	34	18	24480	26.22	1071.08
	13	40	30	18	21600	22.82	1056.48
	14	40	34	18	24480	26.30	1074.35
	15	40	28	19	21280	22.32	1048.87
<i>Average</i>							1063.37
Azobé (120)	16	40	43	18	30960	32.41	1046.83
	17	40	47	18	33840	35.24	1041.37
	18	40	46	16	29440	29.71	1009.17
	19	40	46	17	31280	31.59	1009.91
	20	40	46	17	31280	32.28	1031.97
<i>Average</i>							1027.85

LOAD LEVELS LOAD-DISPLACEMENT CURVE NUMERICAL MODEL

Series	Numerical model											
	Linear				Bi-linear				Bi-linear and G_f^{num}			
	A	B	C	D	A	B	C	D	A	B	C	D
SP_45_80	0.1	1.6	1.7	5.7	-	-	-	-	-	-	-	-
OA_45_80	1.3	1.9	1.9	6.9	-	-	-	-	-	-	-	-
BI_45_80	0.6	1.5	1.8	5.6	0.6	1.1	3.2	5.5	0.6	1.2	4.1	6.3
AZ_45_80	0.9	1.6	1.7	5.0	-	-	-	-	-	-	-	-
AZ_0_80	0.5	2.0	2.8	6.8	0.5	1.4	5.7	6.8	0.5	1.6	6.9	7.4
AZ_90_80	0.8	1.4	1.5	4.4	-	-	-	-	-	-	-	-
AZ_120_80	0.6	1.3	1.4	6.3	0.5	0.9	1.7	6.3	0.4	1.0	2.2	6.9

MESH SENSITIVITY AND CONVERGENCE

In this appendix the mesh sensitivity and the convergence behaviour of the numerical model is performed. The study is performed on two series, the AZ_45_80 and AZ_0_80 series. The mesh sensitivity of the other series show similar convergence patterns to either of the two. The convergence is influenced by two factors: the mesh size and the load step size. The mesh sensitivity for both are evaluated in this appendix.

Mesh size

The mesh sensitivity is tested for four mesh sizes: 0.5, 1.0, 2.0 and 5.0 mm. Only the mesh size for the middle hardwood part is adjusted, the mesh size of the spruce end parts and the supports remains unchanged at 10.0 mm. Fig. D.1 shows how the load-displacement curve changes when the mesh size of the middle azobé notched part is adjusted.

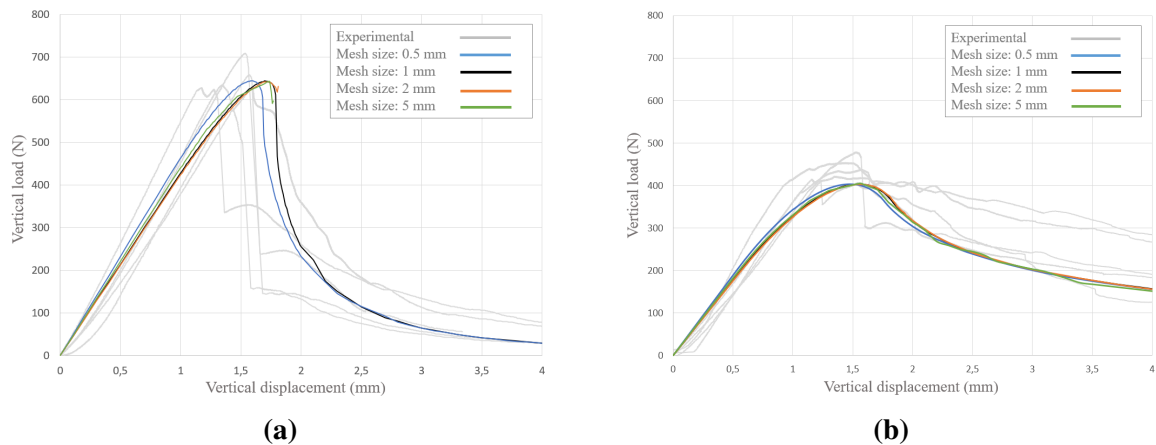


Figure D.1: Load-displacement curve for (a) the AZ_45_80 series and (b) the AZ_0_80 series, for a mesh size of 0.5, 1.0, 2.0 and 5.0 mm.

Results in Fig. D.1 demonstrate that the mesh sensitivity for both models is different. In Fig. D.1a there is a shift in the vertical displacement between mesh size 0.5 and 1.0 mm. A mesh size higher than 1.0 mm results in divergence for the AZ_45_80 series. Due to the brittle failure of the series, the model is unable to simulate the unstable cracking and sudden drop in stiffness of the specimen. Fig. D.1b shows that the mesh sensitivity is less for the AZ_0_80 series. An increase in the mesh size does not result in significant changes

in the load-displacement curve, and with a mesh size higher than 1.0 mm no divergence occurs. The implemented constitutive law for this series does not result in unstable cracking and sudden drops in stiffness. For both series, the modelled peak load is independent of the mesh size.

The number of iterations in each load step for the different mesh sizes is shown in Fig. D.2 for the AZ_45_80 series and in Fig. D.3 for the AZ_0_80 series. During the analyses the displacement is applied in different load step size groups according to Tab. 6.5. The transition in step size is indicated in the figures.

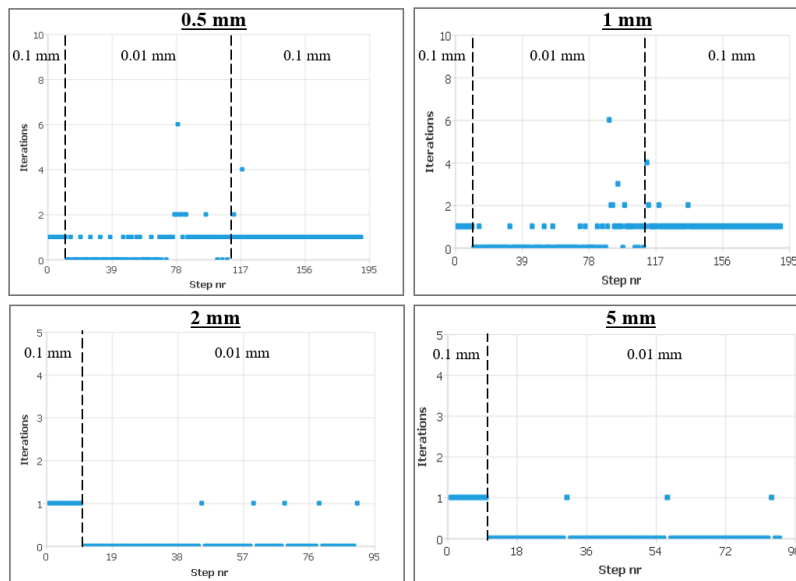


Figure D.2: The number of iterations in each load step for the AZ_45_80 series, with mesh size: 0.5, 1.0, 2.0 and 5.0 mm.

In Fig. D.2 can be seen that for a load step size of 0.01 mm, a larger mesh size leads to less iterations. Note that for mesh sizes 2.0 and 5.0 mm, the numerical model led to divergence and the computation is terminated at approximately a vertical displacement of 1.8 mm. The difference in number of iterations between the mesh sizes is less significant for the AZ_0_80 series, as shown in Fig. D.3. The maximum number of iterations in a load step in this series is two, whereas for the AZ_45_80 series the maximum is six iterations.

In Fig. D.4 the total elapsed time for each mesh size is shown for the two series. Between the two series there is no difference in the total time for each mesh size. Between the mesh sizes there is a significant difference in the total computational time to perform the analysis. This is expected as the smaller the element size, the more elements and the larger the global stiffness matrix. The computation time decreases exponentially with an increase in the mesh size.

Step size

The mesh sensitivity is also evaluated for different load steps. The numerical models in the main report are performed with load steps of 0.1 and 0.01 mm according to Tab. 6.5. The

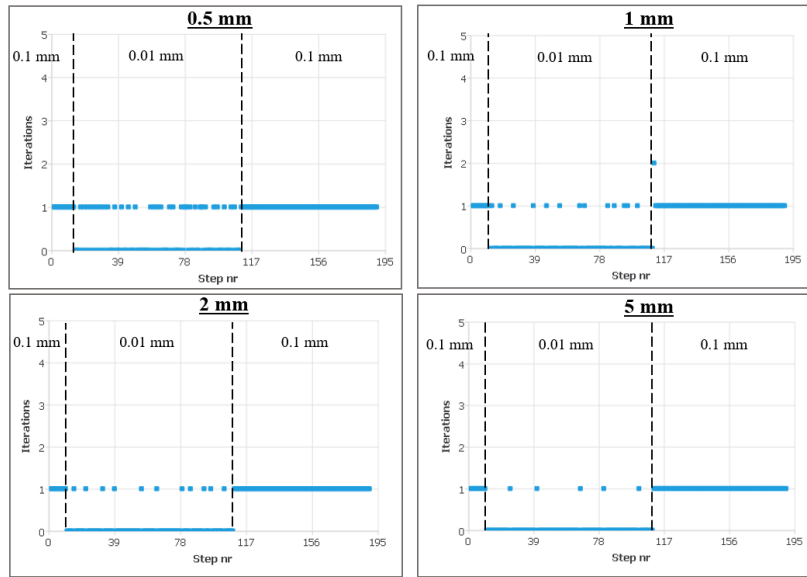
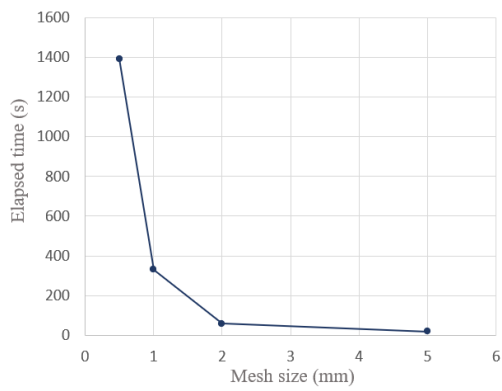


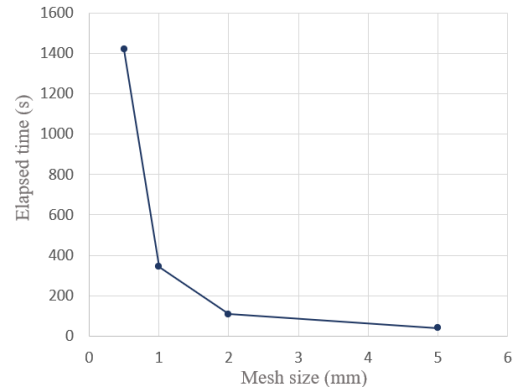
Figure D.3: The number of iterations in each load step for the AZ_0_80 series, with mesh size: 0.5, 1.0, 2.0 and 5.0 mm.

mesh sensitivity is evaluated for a constant load step size of 0.1 mm and 0.5 mm. In Fig. D.5 the load-displacement curve is shown for the AZ_45_80 and AZ_0_80 series.

Fig. D.5 demonstrates that for larger step sizes the accuracy of the numerical model decreases. Moreover, a larger step results in a less smooth load-displacement curve. This is more significant for the AZ_45_80 series than for the AZ_0_80 series.

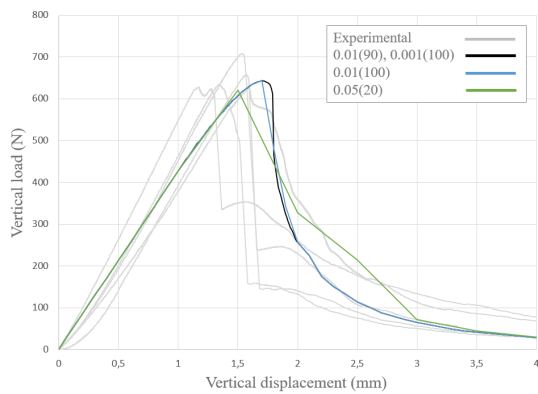


(a)

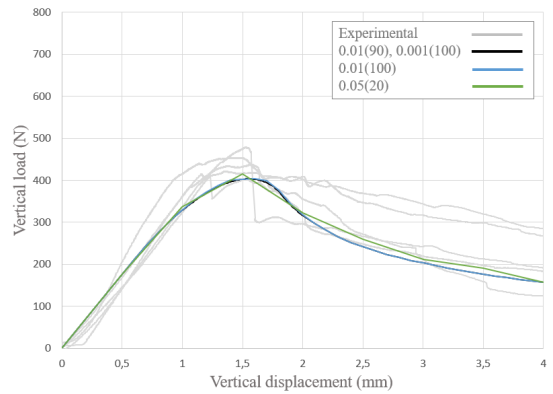


(b)

Figure D.4: The computation time for (a) the AZ_45_80 series and (b) the AZ_0_80 series.



(a)



(b)

Figure D.5: Load-displacement curve for (a) the AZ_45_80 series and (b) the AZ_0_80 series with different load step sizes.

CALCULATIONS THEORETICAL ENERGY RELEASE ANALYSIS

In the theoretical energy release analysis the critical load of the system F_c is calculated based on linear-elastic beam theory and the principles of fracture energy by Griffith (1921). In this appendix the calculations are shown to obtain the equation in Section 7.1, Eq. 7.2. Note that this equation only is applicable for hardwood species with a height of 80 mm.

First, the linear-elastic relation between the force and vertical displacement is set up. The beam is discretized by three fields and the use of symmetry. In Fig. E.1 the symmetry model is shown. Due to symmetry, the rotation at mid-span is zero. Thus the reaction force at the support at each end is half the total externally applied load.

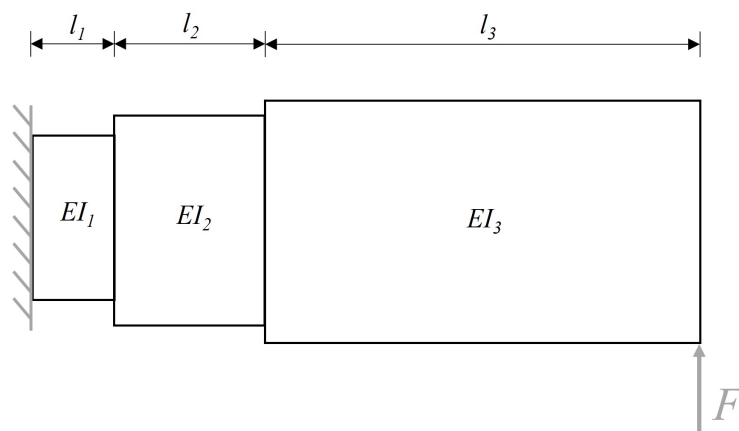


Figure E.1: Linear-elastic symmetry model to obtain the load-displacement relation.

The model consists out of three fields, where field 1 represents the notch, with a reduced section modulus and a MoE value according to Tab. 5.8. The second fields represents the transition zone from the notch notch to the spruce parts. The section modulus of this fields is related to the changing location of the neutral axis due to the discontinuity at mid-span. The height of the neutral axis in field 2 is obtained from the strain distribution from the DIC as shown in Fig. 4.3 and the stress distribution from the numerical model. From both models the location of the neutral axis in field 2 can be approximated by a linear relation. For simplicity's sake this linear relation is discretized. For future research a more

comprehensive approach must be taken to exactly determine the location of the neutral axis independent on the height of the beam.

Using Euler-Bernoulli beam theory, the displacement and rotation is computed at the end of each field. Summation of all the displacements at the end of each field and adding the contribution due to rotation, yields the vertical displacement at the end of field 3 for the applied load F :

$$u = \frac{Fl^3}{16Eb} * \left(\frac{0.479}{(h - a + 4)^3} + \frac{1.206}{(h - \frac{1}{2}a - 6)^3} + \frac{0.000193E}{h^3} \right) \quad (\text{mm}) \quad (\text{E.1})$$

This equation only holds for the tested hardwood species and a height of 80 mm. The constants in the equation represent the changing neutral axis over the length of the beam. Based on the numerical model, the location of the neutral axis is constant for the hardwood species with a height of 80 mm. For spruce and the azobé series with a height of 120 mm, the location of the neutral axis changes and the equation above does not hold.

In order to determine the critical cracking load, the potential energy of the system is determined. According to linear-elasticity, the potential energy of the system is given by Eq. E.2. It assumed that there are no stresses and strains before the load is applied. Note that a factor 2 is applied due to symmetry of the model.

$$W = -\frac{1}{2} \cdot 2F \cdot u \quad (\text{Nmm}) \quad (\text{E.2})$$

Next, Eq. E.1 is substituted in the equation for the potential energy, Eq. E.2. Next, the theory by Griffith (1921) is applied, which states that a reduction in potential energy corresponds to the formation of the fracture surface $b \cdot da$. The ratio between the reduction of potential energy and the increase in cracked surface area is given by a positive release of energy G , Eq. E.3.

$$G = -\frac{dW}{b \cdot da} \quad (\text{N/mm}) \quad (\text{E.3})$$

First the change of potential energy dW due to an incremental increase in the crack length da is determined. Next, the equation for dW is substituted in Eq. E.3. This results in the equation for the energy release. According to the failure criterion Griffith (1921), crack propagation is initiated when the energy release G is equal to a critical value $G_{c,I}$, which in linear-elasticity is equal to the fracture energy $G_{f,I}$ (see Section 2.2.1). Solving the equation for the external load F yields the critical value for the load, which is the load when cracking is initiated. Aside from the geometry of the specimen, the important parameters in the equation are the MoE of fields 1 and 2, which is the MoE perpendicular to the grain, and the fracture energy $G_{f,I}$